

Self-Organization of Two Anionic Azo Dyes in the Presence of Alkaline Earth Ions

Von der Fakultät für Naturwissenschaften
der Universität Paderborn
genehmigte

Dissertation

zur Erlangung des Grades eines
Doktors der Naturwissenschaften
-Dr. rer. nat.-

von Rolf Michels, geboren am 1. Juli 1984 in Höxter

Paderborn 2014

Die vorliegende Arbeit entstand zwischen Januar 2010 und Juli 2014 im Fachbereich physikalische Chemie der Fakultät für Naturwissenschaften der Universität Paderborn.

Erstgutachter: Prof. Dr. Klaus Huber

Zweitgutachterin: Prof. Dr. Claudia Schmidt

Tag der Einreichung: 30.07.2014

Tag der mündlichen Prüfung: 26.09.2014

Hiermit erkläre ich, die vorliegende Dissertationsschrift selbstständig verfasst zu haben. Die dazu genutzte Literatur, zu Hilfeleistungen herangezogene Institutionen sowie Beiträge anderer Personen zu dieser Arbeit werden im Rahmen der Dissertationsschrift vollständig angegeben bzw. kenntlich gemacht.

Paderborn, im Juli 2014

Rolf Michels

*Zu End' die Zeit als Candidat,
geschrieben das Elaborat!
Doch ganz und gar nicht Recht wär's nun,
den Ruhm sich selbst nur anzutun.
Denn der dies schrieb, war gut geleitet,
drum große Freud' es ihm bereitet,
jenen ein herzlich' Dankeschön
die ihn begleitet' kundzutun.*

Mein besonderer Dank mit Blick auf diese Doktorarbeit gilt Herrn Prof. Dr. Klaus Huber. Ich habe ihn als verständnisvollen und fürsorglichen Lehrmeister, steten Unterstützer und unermüdlichen Diskussionspartner kennengelernt. Durch seine ausgezeichnete Betreuung dieser Arbeit hat er in hervorragender Weise zu ihrem Gelingen beigetragen.

Bei Frau Prof. Dr. Claudia Schmidt bedanke ich mich herzlich für ihre bereitwillige Übernahme des Korreferats.

Herrn Thomas Sinemus, Herrn Dr. Jan Hoffmann, Herrn Prof. Dr. Bernhard Brutschy, Frau Dr. Yvonne Hertle, Herrn Prof. Dr. Thomas Hellweg, Herrn Dr. Günter Goerigk, Frau Dr. Ulla Vainio und Herrn Dr. Jérémie Gummel danke ich für unsere erfolgreichen Kooperationen im Rahmen dieser Dissertation. Hervorheben möchte ich hier Herrn Dr. Günter Goerigk, der mich durch zahlreiche anregende Diskussionen und sein großzügiges Bereithalten von Messzeit am HASYLAB in besondere Weise unterstützt hat.

Herrn Dr. Ralf Schweins und Herrn Dr. Sebastian Lages als ehemaligen Angehörigen des Arbeitskreises danke ich für ihre Unterstützung in der Anfangsphase meiner Doktorandenzeit sowie für freundschaftliche und ergiebige Zusammenarbeit.

Meinen langjährigen Kolleginnen und Kollegen des Arbeitskreises, namentlich Frau Marina Kley, Frau Anna Ezhova, Herrn Dr. Frank Markus Bayer, Herrn Markus Hansch, Herrn Dr. Sanjib Saha, Herrn Dr. Martin Schneider, Herrn Dr. Todor Hikov sowie Herrn Roman Nayuk danke ich herzlichst für das heitere Miteinander und die freundschaftliche Atmosphäre, derer wir uns zusammen erfreut haben. Mit Blick auf das ausgesprochen positive Arbeitsklima und ihre allseits starke Hilfsbereitschaft danke ich allen Mitarbeiterinnen und Mitarbeitern der Paderborner Physikochemie.

Ein besonders herzlicher Dank gilt den Paderborner Kommilitoninnen und Kommilitonen des „WS 2004“, Frau Dr. Olga Bienemann, Herrn Marko Gemmerich, Herrn Alexander Kröger, Herrn Dr. Christian Kunze, Herrn Dr. Simon Schmücker, Herrn Dr. Martin Urbanski und Frau Dr. Agnes Wycisk, für eine unvergessliche Universitätszeit voller prägender Ereignisse!

Für einen soliden familiären Rückhalt, der mir auch im Hinblick auf diese Arbeit sehr geholfen hat, bin ich meinen Eltern sowie meinen Schwestern und ihren Angehörigen äußerst dankbar.

In innigster Dankbarkeit bin ich meiner Frau verbunden. Ihre Sensibilität, ihr Verständnis und ihre Geduld haben in unschätzbare Weise zu einem erfolgreichen Abschluss dieser Arbeit beigetragen.

Kurzfassung

Die vorliegende Arbeit beschäftigt sich mit der durch Erdalkaliionen induzierten binären Aggregation zweier anionischer Azofarbstoffe in wässriger Lösung. Zur Untersuchung dieses Selbstaggregationsprozesses bedient sich die Arbeit hauptsächlich der zeitauflösenden statischen und dynamischen Lichtstreuung sowie der Röntgenkleinwinkelstreuung. Den Ausgangszustand für die Farbstoffaggregation bildet eine stöchiometrische Lösung der beiden Farbstoffe in Wasser. Bereits in einer solchen Lösung liegt ein kleiner Teil ($< 10\%$) der Farbstoffmoleküle in Form von Aggregaten mit einer Größe von etwa 50 nm vor, während der Großteil der Farbstoffmoleküle in oligomeren Strukturen organisiert ist oder als einzelne Farbstoffmonomere gelöst vorliegt. Wird eine solche Farbstofflösung mit einer wässrigen Lösung eines Erdalkalisalzes vermischt, so setzt ein Aggregationsprozess ein, der in Abhängigkeit von Art und Konzentration der Erdalkaliionen von wenigen Sekunden bis zu etwa einer Stunde lang andauern kann. Dieser Aggregationsprozess wird eingeleitet durch eine sehr kurze (< 1 s) Nukleierungsphase, die eine bestimmte Anzahl wachstumsfähiger Farbstoffaggregate (Nuklei) hervorbringt, welche sich nach Ablauf der Nukleierungsphase nicht mehr ändert. Gefolgt wird die Nukleierung durch eine Wachstumsphase, während der die Nuklei durch schrittweises Anlagern kleinerer Farbstoffbausteine zu faserförmigen Farbstoffaggregaten heranwachsen. Auf diese Weise erzeugte Farbstofffasern können aus deutlich über 10^5 Farbstoffmolekülen aufgebaut sein und Längen von einigen Mikrometern erreichen. Sie haben eine Dicke in der Größenordnung von 10 nm. Bei höheren Farbstoffkonzentrationen bilden die faserförmigen Farbstoffaggregate zudem verzweigte Netzwerke, welche bei sehr hohen Farbstoffkonzentrationen gelartige Eigenschaften annehmen. Die Erdalkaliionen sind auf solche Weise in die Farbstoffaggregate eingebaut, dass die Anzahl ihrer positiven Ladungen in etwa der Anzahl der negativen Ladungen der eingebauten Farbstoffmoleküle entspricht. Die örtliche Verteilung von Erdalkaliionen entlang der Faseraggregate ist gleichförmig. Die beiden Farbstoffe liegen in einem stöchiometrischen Verhältnis von 1:1 im Aggregat vor, was ebenso wie der zwischen benachbarten Erdalkaliionen häufig auftretende Abstand von etwa 1,5 nm auf eine hohe Nahordnung der einzelnen Bausteine im Aggregat hinweist. Die Kinetik des Aggregationsprozesses wird gut durch eine Reaktion 2. Ordnung beschrieben, bei der die Aggregationsgeschwindigkeit proportional einer Wachstumsgeschwindigkeitskonstante sowie der Anzahl wachstumsfähiger Aggregate und der Anzahl nicht umgesetzter Farbstoffbausteine ist. Im Gegensatz zur Gesamtfarbstoffkonzentration haben die Art und die Konzentration der Erdalkaliionen einen deutlichen Einfluss auf die Wachstumsgeschwindigkeitskonstante, was auf einen Zusammenhang der Aktivität wachstumsfähiger Faserenden und/oder freier Farbstoffbausteine mit den Erdalkaliionen hinweist.

Abstract

The present dissertation engages in the binary aggregation of two anionic azotic dyestuffs induced by alkaline earth ions in aqueous solution. The self-assembly process is investigated mainly by means of time-resolved static light scattering, dynamic light scattering and small-angle x-ray scattering. The starting point of the dyestuff aggregation consists in a stoichiometric solution of the two dyestuffs in water. In such a solution, a minor part (< 10 %) of the dyestuff molecules is existent in the form of aggregates with a size of about 50 nm, whereas the major part of the dyestuff molecules is organized as oligomeric structures or dissolved as single dyestuff monomers. If such a dyestuff solution is mixed with an aqueous solution of an alkaline earth salt, an aggregation process sets in. This aggregation process can last for a few seconds or even up to an hour, depending on the type and concentration of the alkaline earth ions. The process is initiated by a very short (< 1 s) nucleation phase yielding a number of dyestuff aggregates capable of growing (so-called nuclei). After nucleation is terminated, the number of nuclei remains constant. The nucleation phase is followed by a growth period during which the initial nuclei grow to fibre-like dyestuff aggregates via a gradual addition of smaller dyestuff building units. The dyestuff fibres formed in this way may contain considerably more than 10^5 dyestuff molecules and attain lengths of several microns. Their thickness is in the order of 10 nm. At higher dyestuff concentrations, the fibre-like aggregates build branched networks which may even adopt gel-like properties. Within the aggregates, the negative charges carried by the dyestuff molecules balance the positive charges carried by the alkaline earth cations. The spatial distribution of the latter along the fibres is homogeneous. The stoichiometry of the two dyestuffs within the aggregates is 1:1. This stoichiometry, together with a distance of about 1.5 nm frequently occurring between alkaline earth ions, points to a distinct short-range order of the building units within the aggregates. The kinetics of the aggregation process can be adequately described by a 2nd order reaction, where the rate of aggregation is proportional to a growth rate constant as well as to the numbers of growing aggregates and of unconsumed dyestuff building units, respectively. In contrast to the total dyestuff concentration, the type and concentration of alkaline earth ions have a strong impact on the growth rate constant. This suggests that the activity of fibre tails and/or of building units is closely related to the alkaline earth ions.

Table of Contents

1.	Introduction and Objective	1
1.1.	Introduction	1
1.2.	Objective	6
2.	Summarizing Discussion	7
2.1.	The Initial State	7
2.2.	Kinetics and Mechanism of the Dyestuff Aggregation	8
2.3.	Structure and Composition of Alkaline Earth Induced Dyestuff Aggregates	11
2.4.	Open Questions	13
3.	Bibliography, Table of Symbols, Coauthors' Contributions and Errata	16
3.1.	Bibliography	16
3.2.	Table of Symbols	18
3.3.	Coauthors' Contributions	20
3.4.	Errata	21
4.	Coaggregation of Two Anionic Azo Dyestuffs at a Well-Defined Stoichiometry	23
	Supporting Information	33
5.	Kinetic and Structural Features of a Dyestuff Coaggregation Studied by Time-Resolved Static Light Scattering	39
	Supporting Information	51
6.	Coaggregation of Two Anionic Azo Dyestuffs: A Combined Static Light Scattering and Small Angle X-Ray Scattering Study	59
	Supporting Information	73

1. Introduction and Objective

1.1. Introduction

Various types of low-molecular compounds with natural or synthetic origin bear the ability to form complex supramolecular structures with interesting properties. Aggregates formed in such self-organization processes can be considered as “physical polymers” consisting of low-molecular units, which correspond to the chemical monomers in a classical polymer. However, aggregates of low molecular compounds differ substantially from classical polymers in their interactions between neighbouring building units. In classical polymers, the monomers are interconnected by covalent bonds, whereas the building units in aggregates are held together by weaker attractions like van-der-Waals forces, π - π -stacking, hydrogen bonds or dipole interactions. Nature uses the reversibility of just these weaker interactions in order to create systems that are capable of sensitively responding to their environment. To give but an example, the reversible aggregation of cytoskeleton proteins is involved in many essential processes like the formation and degradation of intracellular transportation routes.¹ Also a few classes of synthetic compounds, as for instance organic gelators, are designed to reversibly form supramolecular structures in dependence on their environment.²⁻⁸ Despite of the addressed differences in the binding strength between neighbouring building units, the comparison of aggregates and polymers reveals striking analogies concerning the underlying growth mechanisms as well as the morphology of the supramolecular structures. These analogies result from the oriented character of the above-mentioned interactions and suggest that experimental methods and models which are well established in macromolecular chemistry may be successfully adapted to the investigation of self-organizing systems. The great potential of such an approach has for instance been shown by the interpretation of in-situ scattering experiments on cytoskeleton proteins with the help of structural models from polymer physics.⁹⁻¹¹

A prominent class of organic gelators that form supramolecular structures in aqueous solution are ionic dyestuffs, which have been produced in an industrial scale since more than 100 years. Dyestuffs have to fulfil two general yet conflicting requirements: (i) They have to be sufficiently water-soluble in order to make accessible aqueous dyeing liquor ready to expose it to substrates that are to be dyed (e.g. textile fibres) and (ii) they have to adhere on the

substrate, which in turn is impeded if water solubility is too good. Hence, the coexistence of ionic and/or polar groups on the one hand and neutral and/or non-polar patches on the other hand is obligatory. Many types of dyestuff molecules are equipped with expanded π -electron systems, which on the one hand grant them their macroscopic colour properties but on the other hand render certain patches within the molecules flat and inflexible. As a result of these structural elements, ionic dyestuffs bear remarkable analogies to proteins. These analogies consist in the capacity of both classes of substances to establish directed and reversible interactions to other molecules of the same type and manifest in the tendency to form aggregates. The formation of protein aggregates is usually influenced by the actual conformation of the proteins, as they may for instance generate inflexible, flat β -sheet structures or expose polar groups on their surface. In the case of the comparatively small dyestuff molecules, such conformational effects on the aggregation process can be neglected. However, aggregates of both proteins and dyestuffs often exhibit elongated, rod- or worm-like shape with a certain degree of branching. This similarity in the morphologies of dyestuff and protein aggregates emphasizes the analogy between both classes.

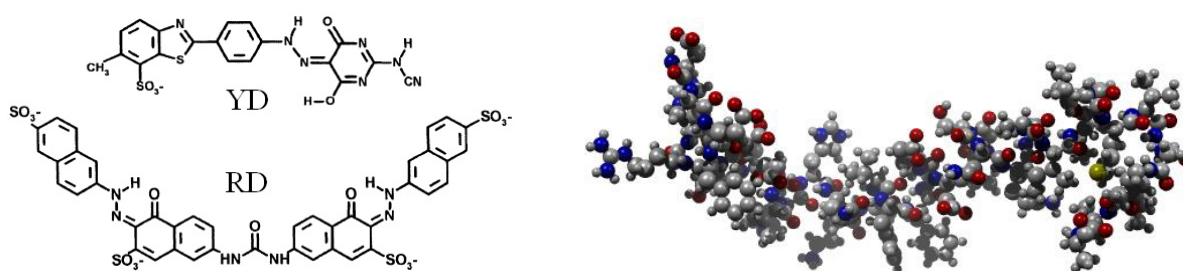


Figure 1.1. Chemical structures of two anionic azo dyestuffs (left-hand side, the coaggregation of YD and RD is the topic of the present dissertation) and an amyloid beta 1-42 protein (right-hand side¹²; the colours denote the following atoms: white = hydrogen, grey = carbon, blue = nitrogen, red = oxygen, yellow = sulphur). The dyestuff like the protein tend to form worm-like aggregates.

Various preceding works in the field of ionic dyestuff aggregation identified the following fundamental aspects. Usually, the tendency to form aggregates is enhanced by addition of an inert salt or a decrease of temperature, whereas an addition of hydrogen bond donors or acceptors like phenol or urea impedes aggregation.¹³ In various cases the aggregates grow over hours or even days, which is also observed for other types of gelators.¹⁴ Further studies have shown that anionic azo dyes in aqueous solution are capable of forming mesophases that consist of rod-like aggregates.^{15,16} Yet scattering methods have rarely been used for the

characterization of dyestuff aggregates. However, the great potential of light scattering for this purpose has already been demonstrated in a few articles.¹⁷⁻²¹

Two of these publications report on mixtures of a red and a yellow anionic azo dyestuff (in the following denoted as RD and YD, see Figure 1.1), for which a binary self-assembly to fibre-like structures induced by the addition of magnesium ions has been identified.^{17,18} The focus of the present dissertation lies on this particular aggregation process. Therefore, references 16 and 17 can be considered as studies directly preceding the present dissertation. In these preceding studies, it could be demonstrated that the rate of aggregation in aqueous solutions containing RD and YD is accelerated by an increase of the Mg^{2+} concentration. Sinemus could identify another remarkable feature of this self-assembly process by showing that the molar ratio of RD and YD within full-grown dyestuff aggregates is 1:1.²² However, many interesting questions have not yet been answered. These questions concern for example a quantitative kinetic analysis, which might provide insight into mechanistic details of the aggregation process, and structural features like network formation or the development of the cross-sections of the presumably fibre-like dyestuff aggregates. Also, the aggregation of RD and YD in the presence of other metal species, like for instance the homologues of Mg^{2+} , and their interaction with the dyestuff molecules have not yet been considered.

The application of time-resolved in-situ scattering techniques²³ and of the worm-like chain model²⁴ show great promise for a further investigation of this aggregation process, which may not only contribute to optimize industrial dyestuff production but may also open up new ways for the generation of responsive materials. For example, a controlled alignment of metal ions within fibre-like dyestuff aggregates might eventually yield wire-like structures on the nanoscale. Moreover, the aggregation of RD and YD could serve as a comparative model for amyloid beta fibrillation (cf. Figure 1.1) since both processes yield supramolecular structures of similar morphologies.^{18,25} The identification of such analogies resulting from a comparison of selected dyestuff and protein aggregation processes may contribute to a better and more fundamental understanding of self-organization.

The present dissertation is based on the application of in-situ scattering techniques using the best available instrumentation. With the help of a recently developed eight-detector combined static and dynamic light scattering instrument, static scattering curves and intensity correlation functions can be measured simultaneously as functions of the time and of the scattering angle. As a special feature of this instrument, its detectors are arranged on two levels, with each level respectively comprising four detectors. By this means, the distances

between neighbouring detection angles is decreased to 8° . Its relatively narrow arrangement of scattering angles renders the instrument in particular suitable for the observation of extended self-assembly processes during which aggregates grow up to several hundred nanometers.

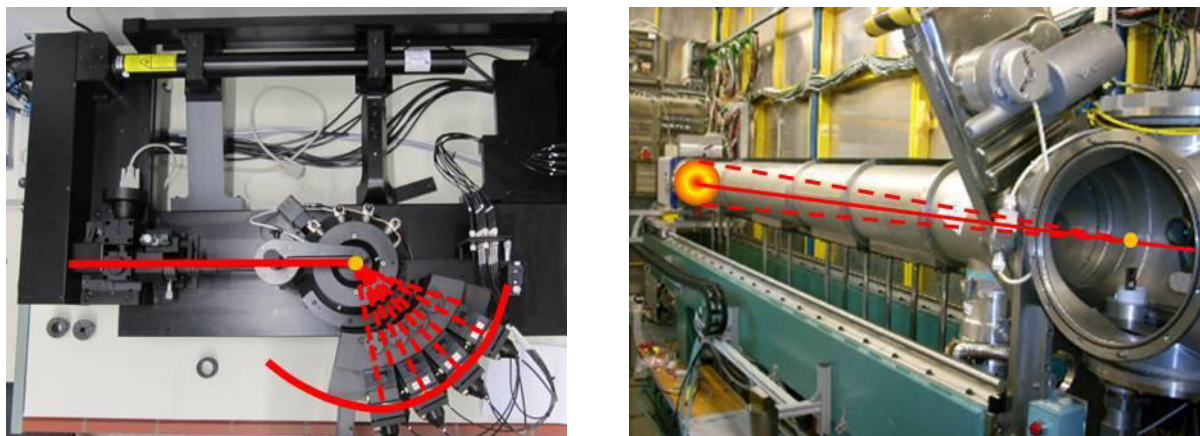


Figure 1.2. Left-hand side: The multi-angle combined static and dynamic light scattering instrument used in the present work. The primary beam impinges on the sample (yellow point) and a part of it is scattered. Eight detectors measure the scattered light (dashed lines) in a plane parallel to the primary beam. The whole array of detectors can be radially moved around the goniometer in order to vary the scattering angles. Right-hand side: The former HASYLAB B1 as an example for a small-angle x-ray scattering instrument. Within the present work, B1 was used for anomalous small-angle x-ray scattering measurements, but it could in principle also be used for time-resolved small angle x-ray scattering. The photons scattered by the sample (yellow point) pass a distance of several meters in a vacuum tube before being detected at scattering angles $< 10^\circ$ by an area detector. For isotropic samples, a radially symmetric scattering pattern is obtained.

On the one hand, the angular dependent static scattering curve yields the molar mass of the scattering particles (e.g. the dyestuff aggregates) and their size in terms of the radius of gyration. Moreover, the static scattering curve contains valuable information on the morphology of the particles as soon as their radius of gyration gets close to 100 nm. From the angular dependency of the intensity correlation functions, on the other hand, the size distribution of the scattering particles and their average hydrodynamic radius can be extracted. The ratio of the hydrodynamic radius from dynamic light scattering and the radius of gyration from static light scattering yields a structure-sensitive coefficient, which again may provide valuable information on the shape of the scattering particles. Multi-angle combined static and dynamic light scattering is thus capable of providing a great deal of information concerning the mass, the size and the morphology of growing aggregates. If conducted in a time-resolved

way, it is an optimal tool to investigate self-assembly processes. Within the context of the present thesis, the first detailed analysis of an aggregation process based on the application of time-resolved simultaneous static and dynamic light scattering is presented. However, the time resolution of the method is restricted to about ten seconds, and the major part of information can be gathered for particles with sizes in between 50 and 500 nm only.

Therefore, multi-angle combined static and dynamic light scattering is hardly suitable to investigate the first stages of self-assembly processes, i.e. nucleation. These stages might last no longer than a second and include the formation of species with sizes of 1 to 10 nm. A tool that is complementary to light scattering and suitable for the in-situ investigation of nucleation is time-resolved small-angle x-ray scattering. 3rd generation synchrotrons like the European Synchrotron Radiation Facility provide x-ray photon fluxes large enough to achieve a time resolution in the regime of 0.01 to 1 seconds, depending on the x-ray scattering contrast and on the concentration of the sample. Due to the much smaller wavelength in comparison to visible light, x-ray photons can be used to probe structural details on length scales down to 1 nm. Eventually, the scattering capacity of x-rays increases with the square of the electron density of the sample, which makes x-ray photons in particular sensitive to heavy metal ions.

1.2. Objective

The objective of the present dissertation is a detailed investigation of the aggregation of RD and YD in aqueous solution. Priority is given to a time-dependent quantification of structural parameters of the aggregates and to the interpretation of the aggregation process by means of suitable kinetic models. Besides, the composition of the formed aggregates shall be further investigated, and information on their branching behaviour and their tendency to form networks shall be obtained. The results are presented in terms of three consecutive articles which are based on each other. Each article represents a separate chapter of the dissertation.

Chapter 4 first investigates aqueous solutions of RD and YD in the absence of alkaline earth ions. This serves as a reference state for alkaline earth induced aggregation. Subsequently, time-resolved multi-angle combined static and dynamic light scattering is applied for the first time to Mg^{2+} -induced aggregation of RD and YD. With the help of this new technique, knowledge of the morphology of the formed aggregates suggested in the previous articles^{16,17} is confirmed and extended.

Chapter 5 focusses on the kinetics of the aggregation of RD and YD in the presence of magnesium ions. Besides, worm-like chain parameters of the aggregates are quantified and first hints on branching and on the temporal evolution of the polydispersity of growing dyestuff aggregates are provided.

Chapter 6 demonstrates that besides Mg^{2+} , also its higher homologues Ca^{2+} , Sr^{2+} and Ba^{2+} induce aggregation of RD and YD, which facilitates to investigate the process by small angle x-ray scattering. The kinetics of aggregation processes induced with the four different types of alkaline earth ions is compared. Successively, lateral growth, branching and network formation during the aggregation process are further highlighted. Finally, the metal-to-dye ratio within full-grown dyestuff aggregates is investigated by means of anomalous small angle x-ray scattering.

2. Summarizing Discussion

The conclusions from chapters 5, 6 and 7 are recapitulated in order to yield an overall picture of the dyestuff aggregation. References written in squared brackets address figures and tables from chapters 5, 6 and 7 demonstrating experimental results which support the conclusions addressed, respectively. However, the reader may easily comprehend the text without paying further attention to these references.

2.1. The Initial State

Before starting the investigation of an aggregation process, a well-defined starting point from which aggregation can be efficiently initiated in a reproductive way had to be established. For the dyestuff aggregation under consideration, such a starting point consists in two separated aqueous solutions. One of these solutions contains an alkaline earth salt and the other one contains an equimolar mixture of RD and YD. All aggregation processes investigated in the framework of the present dissertation were initiated by mixing two of the described aqueous solutions. This initial mixing has mainly been performed with the help of stopped-flow devices. Their use resulted in aggregation processes that proceeded similarly to those achieved by hand mixing of the two components [cf. Chapter 6, Figure S1] and moreover granted a comparatively quick and highly reproductive initiation of the dyestuff aggregation.

We have first established that equimolar solutions of RD and YD represent the condition of the RD and YD molecules right before they undergo alkaline earth induced aggregation. Such solutions contain dyestuff aggregates with a bimodal size distribution [cf. Chapter 4, Figure SI-2]. The slower diffusion mode corresponds to hydrodynamic radii of roughly 50 nm and comprises less than 10 % of the dyestuff molecules, whereas the faster mode corresponds to hydrodynamic radii of less than 10 nm and comprises more than 90 % of the dyestuff molecules [cf. Chapter 4, Figures 6 and 7-B]. The number of dyestuff molecules per aggregate lies in the order of 10^3 for the slow diffusion mode and in the order of 10 for the fast diffusion mode [cf. Chapter 4, Figure 7-A]. The fast diffusion mode thus can be attributed to dyestuff monomers and oligomers. As inferred from SAXS, the latter exhibit rod-like shape [cf. Chapter 6, Figure 3-A and Table 2]. It is likely that these oligomers contain RD and YD in an

equimolar ratio [cf. Chapter 4, Figures 4 and 5] and that they act as “building units” which consecutively add to the growing dyestuff aggregates during alkaline earth induced aggregation. This view provides meaningful explanations for the “step growth” or “monomer addition” mechanism of the growth of alkaline earth induced dyestuff aggregates and for their 1:1 stoichiometry in terms of RD and YD. Both are important findings and will therefore be readdressed in detail in sections 2.2. and 2.3.

The large particles responsible for the slower diffusion mode vanish immediately after magnesium ions are added [cf. Chapter 4, Figure 11], suggesting that they are involved in the nucleation of alkaline earth induced aggregation. Their mass concentration increases with increasing total dyestuff concentration [cf. Chapter 4, Figure 6-B]. Since this is also typical for classical micelles, the large particles have been denoted as “micelle-like” within the present dissertation. However, the structure of these particles as well as a clear-cut critical micelle concentration (cmc) could not be identified unambiguously.

2.2. Kinetics and Mechanism of the Dyestuff Aggregation

Addition of alkaline earth ions in mixed equimolar RD and YD solutions induces an aggregation process which, depending on the type and concentration of alkaline earth ions, may be terminated after a few seconds or proceed for tens of minutes [cf. Chapter 6, Figure 2-A]. Time-dependent molar mass data of the growing dyestuff aggregates can be modelled adequately with the irreversible nucleation-elongation (INE) model [cf. Chapter 5, Determination of Kinetic Parameters] and with the Lomakin model²⁶ [cf. Chapter 5, Supporting Information]. The most characteristic feature of the INE model consists in the continuous formation of nuclei from monomers. However, the INE model matches the experimental data only if it is applied in its simplified form, i.e. by assuming a constant number of nuclei already existent at the beginning of the aggregation process. These nuclei then grow to aggregates by gradually adding monomers/building units. The weak point of the INE model in this most simple form is its incapability to explain the origin of the nuclei. Application of the more general form of the INE model including continuous nucleation until monomers are entirely consumed turned out unsuitable to describe the experimental data. The Lomakin model²⁶, on the other hand, assumes nucleation from micellar species. Such a nucleation is limited in time since it terminates as soon as the monomer concentration falls short of the critical micelle concentration. Unlike the INE model, this provides a physically

meaningful explanation for the origin of the nuclei as well as for the limited duration of the nucleation phase. The growth reaction in the Lomakin model²⁶ is assumed as a gradual addition of monomers/building units to the nuclei, in complete analogy to the INE model.

The applications of both models consistently reveal that the alkaline earth induced dyestuff aggregation is initiated by a very short period of nucleation [cf. Chapter 5, Table 2 and Chapter 6, Table 1]. Whether nuclei are generated from larger, micelle-like particles similar to those which have been found in stoichiometrically mixed RD and YD solutions before the addition of alkaline earth ions, could not be unambiguously clarified since experimental data from the nucleation period were not available [cf. Chapter 5, Figures 3-5 and Table 2; Chapter 6, Figures 4 and 5].

Nucleation is followed by a temporally extended growth period during which the now constant amount of existing aggregates grow further by the gradual addition of small building units. The view of such a “monomer addition mechanism” for the alkaline earth induced aggregation of RD and YD is mainly supported by two findings. First, in the light of a growth of worm-like aggregates, an exponent approaching 0.3 in a correlation of the radius of gyration and the molar mass [cf. Chapter 4, Figure 10] can be only explained by assuming a monomer addition mechanism.²⁷ Again, such a mechanism is especially compatible with a rod-like or worm-like shape of the growing aggregates. Proof for these structures will be discussed in detail in section 2.3. Second, the rate constant describing the growth process (“rate constant of elongation”) is found to be independent of the dyestuff concentration [cf. 3, Figure 4 and Table 2; Chapter 6, Table 1], which likewise confirms the underlying monomer addition mechanism.

On the other hand, there are two quantities on which the rate constant of elongation significantly depends. These are the atomic number of the added alkaline earth species and their concentration. A higher atomic number and/or a higher concentration of alkaline earth ions results in an increase of this rate constant [cf. Chapter 5, Figure 4 and Table 2; Chapter 6, Figure 2-B and Table 1]. In the light of the gradual growth mechanism suggested by both the INE and the Lomakin model²⁶, these findings signify an interrelation of the activity of the growing sites of the aggregates and/or of the added building units with the alkaline earth ions. Likewise, the type and concentration of alkaline earth ions have an impact on the number of nuclei formed. A higher concentration and/or a higher atomic number of the alkaline earth ions lowers the number of growing particles generated during nucleation [cf. Chapter 5, Figure 4 and Table 2; Chapter 6, Table 1 and Figure 2]. There are various alternatives to

impact the final number concentration of nuclei. For instance, the nucleation threshold, the critical nucleus size and/or the rate constant of nucleation could directly be influenced by the type and/or the concentration of alkaline earth ions. All these possible influences are yet beyond the scope of the present work because the nucleation phase could not directly be accessed. Since a possible impact of the type of alkaline earth ion on the scattering contrast was not considered in the data evaluation, also a scattering contrast increasing with the atomic number of alkaline earth ions would cause an apparent decrease in nucleus concentration.

Besides the Lomakin model²⁶, which implicitly introduces a nucleation threshold by letting the nuclei being generated from micelles that exist as long as the monomer concentration is above the critical micelle concentration, other well-established models like the Classical Nucleation Theory²⁸⁻³² (CNT) provide similar features. In CNT, the threshold above which nucleation takes place is given in terms of the critical size of an agglomeration of monomers that has to be exceeded in order to yield a nucleus, i.e. a stable particle capable of growing further. This critical nucleus size originates from the balance between excess free energy of a solute molecule in supersaturated solution with respect to the pure bulk phase and the surface energy needed for the creation of nucleus-solvent interfaces. The latter explains why supersaturation, i.e. the existence of a concentration of dissolved solute molecules above their actual solubility, is possible at all. The probability of forming an agglomeration of solute molecules larger than the critical nucleus size thus determines the rate of nucleation in CNT. Since this critical size increases drastically as the supersaturation is decreased, the rate of nucleation already drops to zero significantly above the solubility and long before particle growth stops. After an initial burst of nucleation, the major part of the remaining supersaturation is consumed due to the addition of solute molecules to the already existing nuclei, i.e. due to growth processes, whereas only a minor part is consumed by henceforth rare nucleation events.

Unfortunately, the lack of experimental data from the nucleation phase does not allow for a more significant interpretation of this period with respect to the dyestuff aggregation under present consideration. Indeed the experimental data presented in this thesis provide indirect information on the nucleation in terms of the number of nuclei formed. However, a direct insight into the period of nucleation highlighting detailed mechanistic features could not be gained due to the circumstance that this period is probably shorter than a second. Therefore, it is for instance not yet possible to determine whether nucleation in the case of the aggregation of RD and YD rather resembles the Lomakin model²⁶ or the CNT.

2.3. Structure and Composition of Alkaline Earth Induced Dyestuff Aggregates

Besides clarifying the state of the RD and YD molecules right before alkaline earth induced aggregation sets in and besides investigating the kinetic and mechanistic aspects of this dyestuff aggregation, the structure and composition of the formed dyestuff aggregates represent a third relevant topic. Regarding this topic, two noteworthy features had already been established prior to the present work and therefore served as a valuable background for this dissertation. Huber et al^{17,18} had provided evidence for a worm-like shape of binary RD and YD aggregates growing at dyestuff concentrations < 0.1 g/l in the presence of magnesium ions and Sinemus²² had proven the 1:1 stoichiometry of these aggregates. Based on these preliminary findings, the present dissertation reveals the structural features of the aggregation process at this stoichiometric ratio in more detail and sheds light on the number of alkaline earth ions per dyestuff molecule within the aggregates.

In the present dissertation, the worm-like shape of aggregates growing at low dyestuff concentrations has been further verified by a couple of new achievements from scattering experiments. These are the trend of the structure-sensitive ratio R_g/R_h [cf. Chapter 5, Figure 9], the interpretation of the correlation between the radii of gyration of growing aggregates and their contour lengths [cf. Chapter 5, Figure 7] and the modelling of scattering curves recorded from growing aggregates [cf. Chapter 5, Figure 9]. The latter two issues have been performed using the worm-like chain model. Its successful application revealed further evidence for the worm-like shape of the dyestuff aggregates and moreover provided information on the evolution of polydispersity and/or network formation. A decreasing relative polydispersity of growing worm-like aggregates [cf. Chapter 5, Figure 8] is in agreement with the view of a fast nucleation period being followed by an extended addition of small building units as addressed in section 2.2. In this regard, the adequate modelling of the growth process using a rate constant independent of the aggregate mass (cf. the Lomakin model²⁶ and the INE model as described in Chapter 5) points to a constant number of growing sites per aggregate and therefore is best compatible with a preferably one-dimensional growth. This again supports a worm-like structure of the aggregates.

The polydispersity of single aggregates can be established reliably as long as no significant network formation sets in, which seems to apply for low total dyestuff concentrations. In contrast to the light scattering experiments, comparatively high dyestuff concentrations were

used for SAXS and especially for ASAXS experiments [cf. Chapter 6, Figures 5 and 8]. Here, hints on a network formation by partial lateral alignment of worm-like dyestuff aggregates [cf. Chapter 6, Figures 6 and 7] could be identified. In such branched structures, which were also observed on electron micrographs [cf. Chapter 5, Figure 2], the branching density again seems to increase further with increasing total dyestuff concentration [cf. Chapter 6, Figure S7]. Also, the dimension of the diameter of the dyestuff aggregates could be established to be close to 10 nm.

As could be concluded from ASAXS experiments, alkaline earth ions are homogeneously distributed along the dyestuff aggregates down to a scale of < 10 nm. At the same time, a recurring distance of approximately 1.5 nm between alkaline earth ions could be unambiguously identified [cf. Chapter 6, Figure 8]. In addition to the 1:1 molar stoichiometry of RD and YD established by UV/vis absorption measurements [cf. Chapter 4, Figure 2], the molar ratio of alkaline earth ions and dyestuff molecules within the aggregates could be estimated using a combination of ASAXS and XANES measurements [cf. Chapter 6, Figures 8, S5 and S6]. The results [cf. Chapter 6, Table 3] provide evidence for a complete neutralization of anionic charges on dyestuff molecules by cationic charges from strontium ions within the dyestuff aggregates. All these features reveal a high degree of order of the dyestuff aggregates at the nanoscale that may be crucial to their structural and mechanical properties.

2.4. Open Questions

This section focusses on questions that are not or only partially answered in the present thesis. These questions mainly concern (i) the nucleation phase of the dyestuff aggregation, (ii) the morphology of the building units and the mode of their addition to the dyestuff aggregates during alkaline earth induced growth processes and (iii) the transferability of results among samples with different dyestuff content and/or different type of alkaline earth ions.

The present dissertation has indeed provided reliable insight into the stages right before and a few seconds after the addition of alkaline earth ions to stoichiometric mixtures of RD and YD in aqueous solution. However, the nucleation phase, which lies in between these two stages, was not directly accessible. Therefore, the initial interaction of the bimodal dyestuff species with the added alkaline earth ions and the exact role of the latter during nucleation could not be highlighted. A direct investigation of the nucleation phase thus represents a particular challenge for future research. It requires an exceptionally well defined initiation process possibly including the use of a stopped-flow device in combination with a time resolution of the measuring technique in the order of a millisecond. For a future application of time-resolved SAXS, any possibilities to increase the scattering contrast and to slow down the nucleation phase should be reconsidered.

The nucleation phase is followed by a growth period during which the existing aggregates grow further by a gradual addition of smaller building units. The current view suggests that these building units already exhibit a composition close to the one of the final aggregates, but their structure and especially their origin could not be thoroughly investigated within the limits of the present thesis. They might resemble the small cylindrical particles identified in stoichiometric solutions of RD and YD prior to the addition of alkaline earth ions [cf. Chapter 4, Figures 6 and 7, Chapter 6, Figure 3]. Alternatively, the building units may feature similarities to so-called protofilaments and/or protofibrils, which are known to involve as intermediate states in biological fibre growth processes (cf. for instance the aggregation of amyloid beta^{33,34} or fibrin³⁵ proteins). In the latter case, the “monomer addition” based fibre elongation as well as fibre branching would proceed via partial lateral alignment of protofibrils. The strongest argument for a fibril-like character of the building units is thus its capability of explaining such a “partial lateral alignment”, as it was found for high dyestuff concentrations [cf. Chapter 6, Figure 7]. The two possible ways of fibre growth including branching are illustrated in Figure 2.1. Eventually, a dependency of the size and the

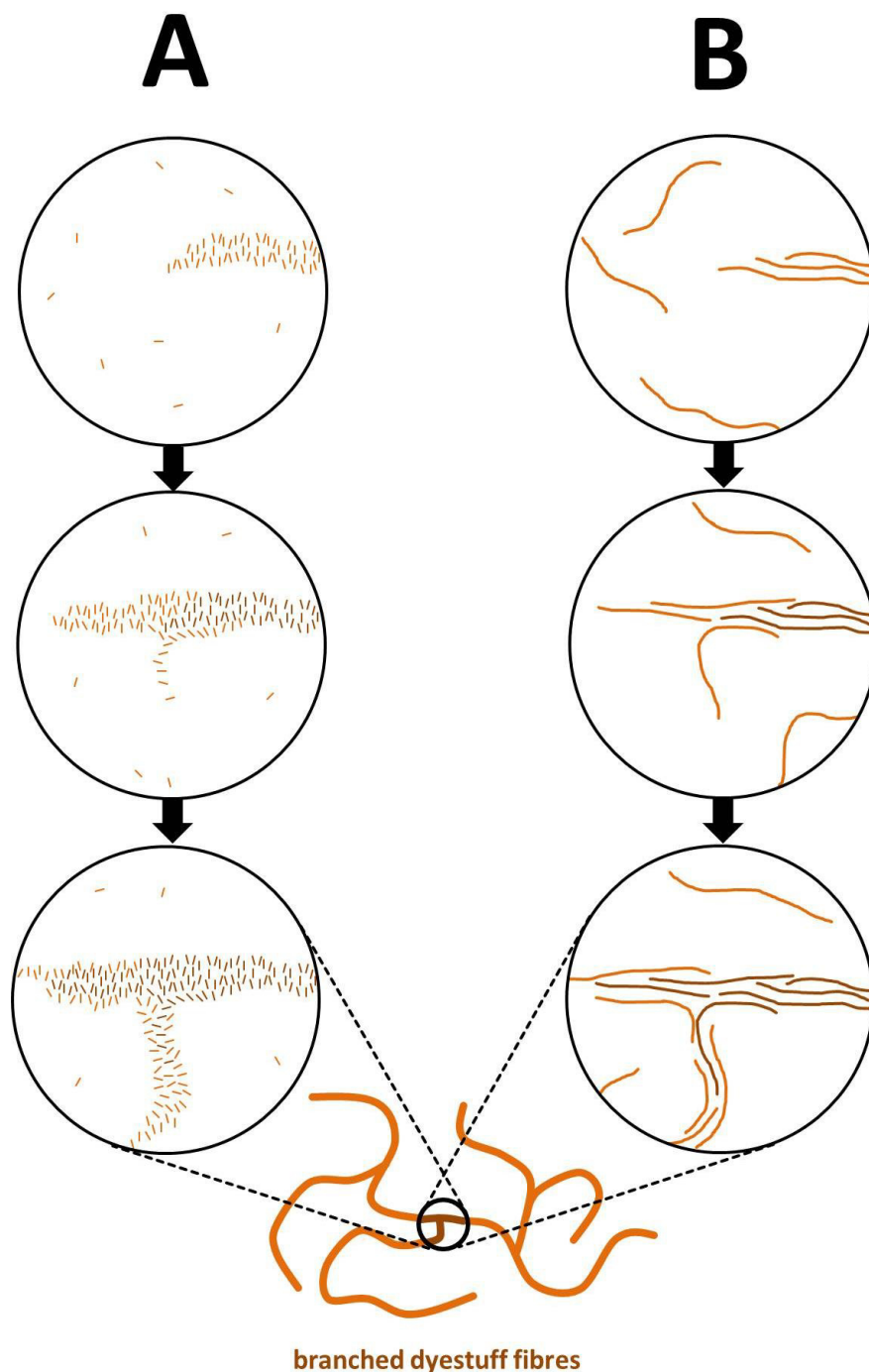


Figure 2.1. Two possible ways of branched dyestuff fibre formation are shown. (A) The growth of dyestuff fibres via a continuous addition of small, stiff building units every now and then introduces structural defects in the growing fibre. Such a defect may lead to a new fibre branch. (B) Worm-like dyestuff protofibrils establish the “monomers” and aggregate via lateral alignment, which still corresponds to a “monomer addition” mechanism. Sometimes this lateral alignment occurs only partially, which allows the formation of a new fibre branch.

morphology of the building units on the type and/or concentration of alkaline earth ions and/or on the total dyestuff concentration cannot be excluded.

Another issue that might be considered in possible future research is the transferability of results gained for a distinct sample to other samples with different type of alkaline earth ions and/or different dyestuff content. The impact of the dyestuff concentration on the aggregation process has been described only in a qualitative way. For example, it is yet unclear whether mature dyestuff fibres which undergo “partial lateral alignment” [cf. Chapter 6, Figure 7] at the fairly high dyestuff concentrations used for SAXS experiments originate from a growth process similar to the ones described for the lower dyestuff concentrations [cf. Chapters 2 and 3]. Also, the stoichiometry of RD and YD has only been investigated for dyestuff aggregates which had grown in the presence of magnesium ions [cf. Chapter 4, Figure 2] and was not explicitly verified for the dyestuff aggregation with calcium, strontium and barium ions. Furthermore, the number ratio of metal ions and dyestuff molecules within the aggregates has only been investigated for strontium induced aggregation processes at comparatively high dyestuff contents [cf. Chapter 6, Figure 8 and Table 3]. Whether these findings also apply to aggregation processes observed under different conditions is not evident. Yet, the strongest support for close similarity among dyestuff aggregation processes proceeding under different conditions is provided by the fact that all processes investigated by means of time-resolved light scattering could be comprehensively described with the same kinetic model [cf. Chapter 6 Figure 2 and Table 1].

3. Bibliography, Table of Symbols, Coauthors' Contributions and Errata

3.1. Bibliography

- 1 Alberts, B.; Johnson, A.; Lewis, J.; Raff, M.; Roberts, K.; Walter, P. *Molecular Biology of the Cell*, 4th edition, **2002**, Garland Science, New York, page 907 ff.
- 2 Percec, V.; Johannsson, G.; Heck, J.; Ungar, G.; Batty, S. J. *J. Chem. Soc. Perkin Trans.* **1993**, *1*, 1411.
- 3 Beginn, U.; Keinath, S.; Möller, M.; *Macrom. Chem. Phys.* **1998**, *199*, 2379.
- 4 Beginn, U.; Zipp, G.; Möller, M.; *J. Polym. Sci. A: Polym. Chem.* **2000**, *38*, 631.
- 5 Lehn, J. M.; Mascal, M.; Decian, A.; Fischer, J.; *J. Chem. Soc. Chem. Commun.* **1990**, *6*, 479.
- 6 Sijbesma, R. P.; Beijer, F. H.; Brunsveld, L.; Folmer, B. J. B.; Hirschberg, J. H. K. K.; Lange, R. F. M.; Lowe, J. K. L.; Meijer, E. W.; *Science* **1997**, *278*, 1601.
- 7 Fuchs, K.; Bauer, T.; Thomann, R.; Wang, C.; Friedrich, Ch.; Mühlhaupt, R.; *Macromolecules* **1999**, *32*, 8404.
- 8 Würthner, F.; Thalacker, Ch.; Sautter, A.; Schärtel, W.; Ibach, W.; Hollrichter, O.; *Chem. Eur. J.* **2000**, *6*, 3871.
- 9 Sayers, Z.; Koch, M. H. J.; Bordas, J.; Lindberg, U.; *Eur. Biophys. J.* **1985**, *13*, 99.
- 10 Spann, U.; Renner, W.; Mandelkow, E.-M.; Bordas, J.; Mandelkow, E.; *Biochemistry* **1987**, *26*, 1123.
- 11 Mandelkow, E.-M.; Mandelkow, E.; *Cell Motil. Cytoskeleton* **1992**, *22*, 235.
- 12 Created with UCSF Chimera using data from the following article: Tomaselli, S.; Esposito, V.; Vangone, P.; van Nuland, N. A.; Bonvin, A. M.; Guerrini, R.; Tancredi, T.; Temussi, P. A.; Picone, D.; *Chembiochem* **2006**, *7*, 257.
- 13 Burdett, B. C. in: *Aggregation Process in Solution*, **1983**, Elsevier Sci. Pub. Co.
- 14 Lopez, D.; Guenet, J.-M.; *Macromolecules* **2001**, *34*, 1076.
- 15 Attwood, T. K.; Lydon, J. E.; Jones, F.; *Liquid Crystals* **1986**, *1*, 499.
- 16 Tiddy, G. J. D.; Mateer, D. L.; Ormerod, A. P.; Harrison, W. J.; Edwards, D. J.; *Langmuir* **1995**, *11*, 390.
- 17 Inglés, S. E.; Katzenstein, A.; Schlenker, W., Huber, K.; *Langmuir* **2000**, *16*, 3010.

-
- 18 Katzenstein, A.; Huber, K.; *Langmuir* **2002**, *18*, 7049.
- 19 Datyner, A.; Flowers, A. G.; Pailthorpe, M. T.; *J. Colloid Interf. Sci.* **1980**, *74*, 71.
- 20 Datyner, A.; Pailthorpe, M. T.; *J. Colloid Interf. Sci.* **1980**, *76*, 557.
- 21 Datyner, A.; Pailthorpe, M. T.; *Dyes Pigm.* **1987**, *8*, 253.
- 22 Sinemus, T. Aggregationsverhalten ausgewählter Gelbildner. Master Thesis, Universität Paderborn, **2006**.
- 23 Becker, A.; Schmidt, M.; *Macromol. Chem. Macromol. Symp.* **1991**, *50*, 249.
- 24 Kratky, O.; Porod, G.; *Recl. Trav. Chim. Pays-Bas* **1949**, *68*, 1106.
- 25 Witte, T. ; Haller, L. A. ; Luttmann, E.; Krüger, J.; Fels, G.; Huber, K.; *J. Struct. Biol.* **2007**, *159*, 71.
- 26 Lomakin, A.; Teplow, D. B.; Kirschner, D. A.; Benedek, G. B. *Proc. Natl. Acad. Sci. USA* **1997**, *94*, 7942.
- 27 Liu, J.; Rieger, J.; Huber, K. *Langmuir* **2008**, *24*, 8262.
- 28 Smoluchowski, R. *Z. Phys. Chem.* **1917**, *29*, 129.
- 29 LaMer, V. K.; Dinegar, R. H. *J. Am. Chem. Soc.* **1950**, *72*, 4847.
- 30 Kashchiev, D. *J. Chem. Phys.* **1982**, *76*, 5098.
- 31 Robb, D. T.; Pivman, V. *Langmuir* **2008**, *24*, 26.
- 32 Vekilov, P. G. *Crys. Growth & Design* **2010**, *10*, 5007.
- 33 Walsh, D. M.; Lomakin, A.; Benedek, G. B.; Condrón, M.; Teplow, D. B. *J. Biol. Chem.* **1997**, *272*, 22364.
- 34 Walsh, D. M.; Hartley, D. M.; Kusumoto, Y.; Fezoui, Y.; Condrón, M.; Lomakin, A.; Benedek, G. B.; Selkoe, D. J.; Teplow, D. B. *J. Biol. Chem.* **1999**, *274*, 25945.
- 35 Hunziker, E. B.; Straub, P. W.; Haerberli, A. *J. Ultrastruct. Res.* **1988**, *98*, 60.

3.2. Table of Symbols

Symbol	Signification
$[A]$	number concentration of unconsumed building units
$[A]_{\text{tot}}$	total number concentration of building units (unconsumed + consumed)
$[A]^*$	number concentration of unconsumed building units above which micellation occurs (also “critical micelle concentration”)
$[B_i]$	number concentration of an aggregate consisting of i building units
$[B]^{[k]}$	k^{th} moment of an ensemble of aggregates
b	scattering length
c	mass concentration of a solute
$\langle D \rangle_0$	limit of the z-averaged translational diffusion coefficient at zero q
$\langle D \rangle_z(q)$	z-averaged translational diffusion coefficient
δ	Kronecker delta
E	photon energy
f' and f''	real part and imaginary part of an anomalous scattering factor
ϕ	volume fraction
$g_1(\tau)$	field correlation function obtained from dynamic light scattering
$\Gamma(q)$	mean inverse relaxation time, 1 st cumulant in dynamic light scattering
η	dynamic viscosity
K	contrast factor in a light scattering experiment
k_b	Boltzmann constant
k_e	rate constant of elongation or growth
k_n	rate constant of nucleation
L	contour length of a worm-like chain or length of a cylindrical particle
L_w	weight-averaged contour length of an ensemble of worm-like chains
l_p	persistence length of a worm-like chain
λ	photon wavelength
$[M]$	number concentration of micelles
M_A	Molar mass of a building unit
M_L	molar mass per unit length
M_n	number- averaged molar mass

Symbol	Signification
M_w	weight-averaged molar mass
μ_2/Γ^2	normalized variance of the intensity-weighted distribution of diffusion coefficients, 2 nd cumulant in dynamic light scattering
n	refractive index of a solvent
N_A	Avogadro constant
dn/dc	refractive index increment in a light scattering experiment
PD	polydispersity (≥ 1)
$P(q)$	form factor
p_M	number-averaged degree of polymerization of micelles
p_n	number-averaged degree of polymerization of nuclei
p_0	number-averaged degree of polymerization of seeds
Q	Porod invariant
q	scattering vector (also: momentum transfer) in a scattering experiment
θ	scattering angle in a scattering experiment
R	radius of a cylinder or of the cross-section of a worm-like chain
R_g	square root of the z-averaged square radius of gyration
$\langle R_g^2 \rangle_z$	z-averaged square radius of gyration
R_h	mean effective hydrodynamic radius
$R(q)$	Rayleigh Ratio obtained from static light scattering
r_{el}	scattering length of an electron
$\Delta\rho$	excess scattering density
S	raw signal in static light scattering
S_{res}	pure resonant scattering function
$d\Sigma/d\Omega$	differential scattering cross section obtained from small-angle scattering experiments
T	temperature
t	time
τ	relaxation time (also: correlation time) in dynamic light scattering
V	volume
Z	atomic number
z	polydispersity parameter of a Schulz-Zimm distribution

3.3. Coauthors' Contributions

This subsection specifies to what extent coauthors contributed to the articles in chapters 4, 5 and 6. For all parts of the work not addressed here, the first author carries sole responsibility.

3.3.1. Chapter 4

Thomas Sinemus performed the UV/vis study (including the sample preparation, the recording of UV/vis absorption spectra and the primary data evaluation) as a part of his master thesis at Universität Paderborn.

Dr. Jan Hoffmann performed the LILBID-MS measurements at Goethe Universität Frankfurt and contributed to the interpretation of the results from these experiments.

Prof. Dr. Bernhard Brutschy likewise contributed to the interpretation of the results from LILBID-MS measurements and provided drafts for the two paragraphs referring to LILBID-MS in the article.

Prof. Dr. Klaus Huber contributed to the interpretation of all experimental results addressed within the article. He also provided a draft for the introduction of the article and contributed to the composition of all other parts of the article in advisory capacity.

3.3.2. Chapter 5

Dr. Yvonne Hertle and **Prof. Dr. Thomas Hellweg** together with the first author recorded the TEM images shown in the article at Universität Bielefeld.

Prof. Dr. Klaus Huber contributed to the interpretation of all experimental results addressed within the article. He also provided a draft for the introduction of the article and contributed to the composition of all other parts of the article in advisory capacity.

3.3.3. Chapter 6

Dr. Guenther Goerigk and **Dr. Ulla Vainio** together with the first author performed the ASAXS measurements at DESY. They substantially supported the first author in the acquisition of ASAXS data and their further treatment.

Dr. Jérémie Gummel together with the first author performed the SAXS measurements at ESRF. He also supported the first author in the primary treatment of the SAXS raw data.

Prof. Dr. Klaus Huber contributed to the interpretation of all experimental results addressed within the article. He also contributed to the composition of the article in advisory capacity.

3.4. Errata

Chapter 4, equation 2 should write as follows:
$$\frac{Kc}{R(q)} = \frac{1}{M_w} + \frac{\langle R_g^2 \rangle_z}{3M_w} q^2 + kq^4$$

4. Coaggregation of Two Anionic Azo Dye-stuffs at a Well-Defined Stoichiometry

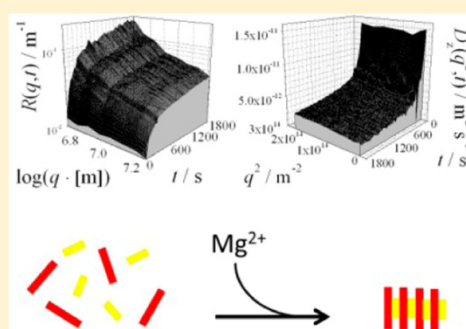
Reproduced with permission from *J. Phys. Chem. B*, **2013**, *117*, 8611-8619.
Copyright 2013 American Chemical Society.

Co-Aggregation of Two Anionic Azo Dyestuffs at a Well-Defined Stoichiometry

Rolf Michels,[†] Thomas Sinemus,[‡] Jan Hoffmann,[§] Bernhard Brutschy,[§] and Klaus Huber^{*,†}[†]Universität Paderborn, Department für Physikalische Chemie, Warburger Straße 100, D-33098 Paderborn, Germany[‡]Berufliche Schulen Korbach und Bad Arolsen, Kasseler Straße 17, D-34497 Korbach, Germany[§]Goethe Universität Frankfurt, Institut für Physikalische und Theoretische Chemie, Max-von-Laue-Str. 7, D-60438 Frankfurt am Main, Germany

Supporting Information

ABSTRACT: The present work investigates the formation of well-defined heteroaggregates from a binary mixture of a red and a yellow azo-dyestuff in the presence of Mg^{2+} ions. Combined static and dynamic light scattering together with laser induced liquid bead ion desorption mass spectrometry (LLBID-MS) has been applied to characterize the states of the pure red dye and the pure yellow dye as well as of their mixture in aqueous solution without Mg^{2+} . These experiments indicated that a structural reorganization on a molecular scale takes place as soon as the two dyes are combined. Solutions of the combined red and yellow dye contain micelle-like mixed entities with a size of a few tenths of nanometers. Upon the addition of Mg^{2+} , these micelles vanish in favor of elongated heteroaggregates, which grow by a stepwise addition of smaller building units. As unraveled by UV/vis spectroscopy, the heteroaggregates that are formed from the red and yellow azo dye in the presence of Mg^{2+} obey a stoichiometric ratio of the two components of 1:1. A new multiangle scattering instrument allowed us for the first time to follow this aggregation process at the stoichiometric ratio by time-resolved combined static and dynamic light scattering, thereby providing further aspects of the worm-like nature of the growing heteroaggregates.



INTRODUCTION

Dyestuffs belong to the first chemicals produced in an industrial scale and for just this reason also caused a 100-year-old riddle in technical chemistry.¹ A reduced solubility of dyestuffs is essential for their adsorption on fabrics but at the same time induces an inherent tendency of the dyestuffs to form aggregates. Such an aggregation is responsible for the formation of voluminous gel-like material in the production liquid or dyeing bath.² Therefore, gel formation inevitably interferes with its proper isolation during workup of the product or competes with the desired adsorption onto a substrate from the dyeing liquor. It is this aggregation which is at the center of the present study. Three aspects propelled our motivation to look at dyestuff aggregation: (i) The desire for a better control or even inhibition of this process generates a need for a detailed information on the mechanism of dyestuff aggregation. (ii) Dyestuff aggregation in aqueous solution shows striking analogies to protein aggregation and may serve as a simple synthetic model system for the reversible polymerization in physiological systems like, for instance, the growth of actin strands in the cytoskeleton³ or like protein fiber formation in protein folding diseases, such as Alzheimer's disease.⁴ (iii) Dyestuff aggregation is a process highly responsive toward changes of ambient conditions like salt concentration or temperature, which thus makes it a highly relevant process for the development of new responsive materials.

In the present study, we focus on a binary dyestuff system comprising two anionic azo-dyestuffs, a red dye (RD) and a yellow dye (YD). Chemical formulas of the two dyestuffs are given in Figure 1. The binary mixture had been originally

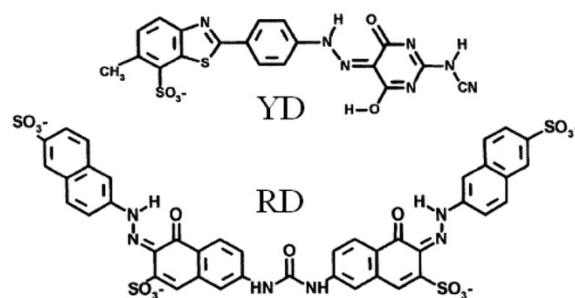


Figure 1. Molecular structures of the yellow dye (YD) and the red dye (RD). Including sodium counterions, the molar mass is 505 g mol^{-1} for YD and 1061 g mol^{-1} for RD. A dimer consisting of one RD and one YD molecule will be considered as a "building unit".

Received: April 22, 2013

Revised: June 10, 2013

Published: June 13, 2013

designed to produce an orange color shade. As has been revealed by two preceding studies,^{5,6} solutions of this dyestuff mixture respond extremely sensitively to the addition of magnesium ions. Dyestuff aggregates are formed within minutes in an aqueous solution in the presence of a few mM MgCl_2 , once a mixture of both components is present in solutions with a concentration of 30–60 mg/l (100 μM) of dyestuff, whereas solutions of either component are comparatively stable in aqueous solution under otherwise identical conditions. This aggregation process could be successfully analyzed with time-resolved static light scattering (TR-SLS) over a period of time of at least 10 min.⁵ Scattering curves recorded during the first 10 min unambiguously indicated a worm-like shape of the growing aggregates, enabling a detailed interpretation of the scattering curves with the model of a continuously bent rod introduced by Kratky and Porod.⁷ A correlation of the resulting z-averaged squared radius of gyration of the aggregates with the corresponding weight-averaged contour length led to trends which could be qualitatively reproduced with an averaged persistence length of 180 nm at a fixed polydispersity corresponding to the most probable distribution of the Schulz–Zimm type.^{6,8}

It is at hand that the accessibility of time-resolved light scattering is about to open new promising routes to interpret time dependent data with kinetic aggregation models and thus creates a need for mechanistic details of the aggregation process. Such details help to identify suitable mathematical growth models for the successive kinetic interpretation of the data.^{9–12} Hence, it is extremely helpful to resolve the stoichiometry of the aggregation process from the binary dyestuff mixture in the system under consideration. It is also helpful to get information on the situation at the start of the aggregation process, which corresponds to the solution state of the binary dyestuff mixture in pure H_2O at the moment when addition of the Mg^{2+} cations triggers the process. Another crucial aspect of the process not yet settled is the origin of the unexpected correlation between the z-averaged aggregate size and the weight-averaged aggregate mass, where both sets of data stem from TR-SLS.^{5,6} The respective trend turned out to be less steep than expected for worm-like aggregates. The use of inadequate concentration values for the growing aggregates or branching of the growing fibers or a simultaneous lateral growth of the fiber cross section were considered as possible origins for these unexpected trends.^{5,6} Fortunately, availability of two recently developed new experimental technologies turned out to shed light on these unsettled issues.

A combined static (SLS) and dynamic light scattering (DLS) device, which enables signal recording at eight different observation angles, makes the evolution of SLS and DLS curves simultaneously accessible in a time-resolved manner. This technique gives access to the evolution of molar mass data and of geometric and hydrodynamic size values as well as to the angular dependent distribution of translational modes with time. We are aware of only a few former studies where this technique has been applied to the analysis of morphological changes: Egelhaaf and Schurtenberger^{13a} reported the time-resolved application of multiangle combined dynamic and static light scattering on the micelle-to-vesicle transition of lecithin. Elimelech et al.^{13b} have investigated the aggregation of fullerene in water with a focus being laid on the evolution of the hydrodynamic radius of the fullerene nanoparticles with time.

Laser-induced liquid bead ion desorption mass spectrometry (LILBID-MS) is another promising tool to provide insight into the aggregate state in solution. The method is based on a soft

ionization and desorption of probe particles from a liquid bead formed directly by the solution of the probe particles and thus may give access to the particles in their native environment.¹⁴

Accordingly, the present work will first investigate by means of UV/vis spectroscopy the stoichiometric relations between the two dyestuff components in the aggregation process, induced by the addition of Mg^{2+} cations. Successively, a detailed characterization of aqueous solutions of pure dyestuff components and binary dyestuff mixtures at variable concentration in the absence of specifically interacting Mg^{2+} cations by combined SLS and DLS and by LILBID-MS will help to establish a view on the solution state at the start of the aggregation process. Finally, time-resolved DLS and SLS will be performed at the herein established stoichiometric ratio of the dyestuff mixture. To this end, a new multiangle combined DLS and SLS instrument will come to operation. Thereby, the present Article will provide the first account on a time-resolved multiangle combined DLS and SLS experiment that has been carried out to investigate a self-assembly process, unraveling the evolution of averaged values for the radius of gyration and the hydrodynamically effective radius together with the growth of aggregate mass values.

■ EXPERIMENTAL SECTION

Materials. Figure 1 shows the chemical structures of the two dyes used. Dyestuffs were available as sodium salts and were purified by dialysis as described in the preceding article.⁵ Magnesium sulfate (assay >99.5%) was purchased from Sigma-Aldrich.

UV/vis Spectroscopy. Two series each with 21 aqueous dyestuff solutions were prepared. The total concentration of RD and YD was kept constant at 0.132 g/L within the first series and at 0.066 g/L within the second series. For each series, the mass fraction of RD was varied in increments of 5%, i.e., $m_{\text{RD}}/(m_{\text{RD}} + m_{\text{YD}}) = 0.00, 0.05, 0.10, \dots, 1.00$. A 5 mL portion of each dyestuff solution of the first series was mixed with 5 mL of 12.8 mM aqueous magnesium sulfate solution, respectively. Similarly, another 5 mL of each dyestuff solution of the second series was mixed with 5 mL of 25.6 mM magnesium sulfate solution. In this way, 21 solutions containing 0.033 g/L dyestuff and 6.4 mM Mg^{2+} as well as another 21 solutions containing 0.066 g/L dyestuff and 12.8 mM Mg^{2+} were created. All of the 42 solutions were then stored for 1 week at room temperature under the exclusion of light. Afterward, each solution was separated by centrifugation from dyestuff aggregates that had formed due to the presence of Mg^{2+} , and an absorption spectrum of each of the 42 cleaned solutions was recorded. For the absorption measurements, a Perkin-Elmer Lambda 19 spectrometer was used. The spectra were recorded at a wavelength regime of 350–650 nm. Furthermore, the extinction coefficients of pure RD and pure YD in the presence of 6.4 and 12.8 mM MgSO_4 have been determined (cf. the Supporting Information). In order to determine the concentrations of RD and YD in the 42 solutions that had been cleaned from dyestuff aggregates by centrifugation, each of the 42 corresponding spectra was fitted by a superposition of the spectra of pure RD and pure YD.

LILBID-MS.¹⁴ In LILBID, an on-demand droplet generator produces liquid droplets (beads) of $\sim 60 \mu\text{m}$ diameter at about 10 Hz, which are injected via differential pumping stages into a vacuum. There each droplet is irradiated with a high intensity mid-IR laser pulse tuned to the absorption of water (3 μm). In this process, each droplet explodes and ejects ions into the vacuum which are mass analyzed in a TOF mass spectrometer. This results in a duty cycle of 1 and allows the handling of

extremely small volumes of solution, usually in the microliter range. In most cases, negative ions are detected which are produced from preformed ions in solution due to an incomplete ion neutralization in the liquid to vacuum transition. The method is very soft at low laser intensity, allowing for the detection of weakly bound complexes, which may be disintegrated at higher intensity. In general, the higher the charge of the ions in solution is, the higher the detection efficiency in mass spectrometry becomes.¹⁵

Aqueous stock solutions of RD (1.32 g/L) and YD (1.32 g/L) as well as a 3.2 mM MgSO₄ solution have been prepared for LILBID-MS experiments. These stock solutions were further diluted and mixed in order to achieve the concentrations desired for the measurements. The procedure by which LILBID-MS measurements were carried out is described in ref 16.

Preparation of Light Scattering Experiments. Two aqueous solutions, one containing 4.47 g/L (4.2 mM) RD and the other one containing 2.13 g/L (4.2 mM) YD, served as stock solutions for light scattering experiments. For the characterization of the pure RD and the pure YD, parts of the pure RD and the pure YD stock solutions were diluted by factors of 2, 6, 18, and 54, respectively, which resulted in dilution series of 2.24, 0.75, 0.25, and 0.08 g/L for pure RD and 1.06, 0.36, 0.12, and 0.04 g/L for pure YD. By combining equal amounts of the pure RD stock solution and of the pure YD stock solution, a mixed stock solution of 3.3 g/L RD and YD with a molar ratio of 1:1 RD:YD was created. This stock solution of mixed RD and YD was used to create a dilution series of 0.132, 0.122, 0.099, 0.066, and 0.033 g/L of mixed RD and YD. All solutions used for light scattering experiments have been cleaned from dust by means of syringe filters (Macherey-Nagel CHROMAFIL PET, 1.2 μm pore size).

In order to investigate the self-assembly of the RD and YD mixture in the presence of Mg²⁺ by means of time-resolved combined SLS and DLS, 3 mL of an aqueous 3.25 mM solution of magnesium sulfate and 3 mL of the solution with 0.132 g/L of mixed RD and YD were injected simultaneously into a scattering cuvette through syringe filters. The start of the process was defined as the time when 1.5 mL of each syringe had entered the cuvette. During the time-resolved experiment, the scattering intensity was recorded over an angular regime of 20–76°.

Time-Resolved Combined Dynamic Light Scattering (DLS) and Static Light Scattering (SLS). Cylindrical quartz cuvettes from Helma with a diameter of 20 mm were used as scattering cells. Prior to any measurement, cuvettes were cleaned from dust by continuously injecting freshly distilled acetone from below for 5 min. The light scattering experiments were performed with a new ALV CGS-3 Compact Goniometer System. The instrument exhibits an array of eight detectors, where the angle between two neighboring detectors is 8°. Each of the eight detectors contains an avalanche photodiode along with a photon correlator. In this way, the static scattering intensity and the intensity correlation can be recorded simultaneously over an angular range of 56°, which allows for the extrapolation of both the SLS and DLS results to zero scattering angle. Compared to an earlier version of the instrument,^{13b} a decrease of the angular spacing to 8° extends the applicability of such an extrapolation to much larger particles. The array of detectors as a whole can be freely rotated around the goniometer between a minimum scattering angle of 20° for the left most detector and a maximum scattering angle of 136° for the right most detector. A He–Ne laser from Soliton with a wavelength of λ = 632.8 nm was used as

a light source, resulting in an accessible *q*-regime of 5.9 × 10⁻³ nm⁻¹ < *q* < 2.5 × 10⁻² nm⁻¹, where

$$q = \frac{4\pi n}{\lambda} \sin\left(\frac{\theta}{2}\right) \quad (1)$$

is the scattering vector and *n* is the refractive index of the solvent. As primary results from light scattering experiments, the excess Rayleigh ratio *R*(*q*) of the solute and the intensity correlation function *g*₂(τ) were calculated. *g*₂(τ) was transformed into the field correlation function *g*₁(τ) by means of the Siegert relation.¹⁷

Treatment of Scattering Data. The Rayleigh ratio *R*(*q*) obtained from static light scattering was evaluated by means of an extended Zimm approximation^{18,19} given by

$$\frac{Kc}{R(q)} = \frac{1}{M_w} + \frac{\langle R_g^2 \rangle_z}{3} q^2 + kq^4 \quad (2)$$

In eq 2, *c*, *M*_w, and ⟨*R*_g²⟩_z are the mass concentration, the apparent weight-averaged molar mass, and the *z*-averaged square radius of gyration of the solute, respectively. The coefficient *k* of the *q*⁴ term served as a further fitting parameter without explicit physical meaning. The contrast factor

$$K = \frac{4\pi^2 n^2}{N_A \lambda^4} \left(\frac{dn}{dc} \right)^2 \quad (3)$$

is dependent on the refractive index increment of the solute, *dn/dc*, where *N*_A is Avogadro's number. *dn/dc* has to be known in order to calculate absolute *M*_w values from experimental SLS data. We assumed (dn/dc)_{YD} = 0.320 mL/g and (dn/dc)_{RD} = 0.401 mL/g, as determined by Inglés et al.⁵ For molar mixtures of 1:1 RD:YD, we estimated the refractive index increment as a weight-average of the values of the two pure components, yielding (dn/dc)_{RY} = 0.375 mL/g.

The field correlation function *g*₁(τ) obtained from DLS was treated in two alternative ways. According to the cumulant analysis,²⁰ a plot of ln(*g*₁(τ)) versus relaxation time τ can for small τ be described by a function of the form

$$\ln(g_1(\tau, q)) = C - \Gamma(q)\tau + \frac{\mu_2}{2\Gamma^2} \tau^2 \quad (4)$$

where *C* is a constant and Γ(*q*) is the mean inverse relaxation time of diffusive modes with the *z*-averaged translational diffusion coefficient ⟨*D*⟩_z(*q*) = Γ(*q*)/*q*². The quantity μ₂/Γ² corresponds to the normalized variance of the intensity-weighted distribution of diffusion coefficients. It served as a fitting parameter only and was not further considered. Linear extrapolation of ⟨*D*⟩_z(*q*) toward *q*² → 0 yields the *z*-averaged diffusion coefficient at zero scattering angle, ⟨*D*⟩₀. The translational diffusion coefficient can be transformed into a mean effective hydrodynamic radius *R*_h of the particles via the Stokes–Einstein equation

$$R_h = \frac{k_B T}{6\pi\eta \langle D \rangle_0} \quad (5)$$

where *k*_B is the Boltzmann constant, *T* is the temperature, and η is the dynamic viscosity of the solvent. Within the present work, the cumulant analysis was used to extract hydrodynamic radii from DLS data in a fast and statistically robust way.

The ratio of the two size parameters *R*_g and *R*_h obtained from SLS and DLS

$$\rho = \frac{R_g}{R_h} \quad (6)$$

is a shape-sensitive parameter and becomes smaller with increasing compactness of the particles. Within the present work, the use of a multiangle combined DLS and SLS instrument allowed us for the first time to record ρ in a time-resolved way during a self-assembly process.

An alternative way of treating DLS data provides information about the distribution of particle sizes by modeling the field correlation function with a series of exponentials:

$$g_1(\tau, q) = \sum_{i=1}^N a_i(q) \exp(\Gamma_i(q)\tau) \quad (7)$$

In eq 7, each coefficient $a_i(q)$ represents the intensity-weighted contribution of the respective $\Gamma_i(q)$ to the distribution of diffusive modes, which can be illustrated by a plot of $a_i(q)$ versus $\Gamma_i(q)$. For large numbers of exponentials (usually $N \geq 50$), eq 7 can be established by means of the CONTIN analysis,²¹ which may, on the one hand, give detailed information on the shape of the size distribution of a sample, but on the other hand, evaluation of the coefficients $a_i(q)$ and $\Gamma_i(q)$ may suffer from artifacts. Especially for the case of two well-separated modes, DLS data can be adequately modeled with double- or triple-exponentials ($N = 2$ or 3). This allocates a maximum of two exponentials per mode and in this way allows for a statistically robust estimate of the z -averaged particle size and of the corresponding partial scattering intensity of the respective mode. The partial scattering intensity $R_i(q)$ of mode Γ_i is proportional to the coefficient a_i :

$$R_i(q) = \frac{a_i(q)}{\sum_{i=1}^N a_i(q)} R(q) \quad (8)$$

Once the subdivision into different modes is significant, each $R_i(q)$ can be evaluated individually by means of eq 2, yielding the scattering at zero angle

$$R_i(q=0) = Kc_i M_{w,i} \quad (9)$$

and the radius of gyration $R_{g,i} = [\langle R_g^2 \rangle_{z,i}]^{1/2}$ of the respective diffusive mode Γ_i .

RESULTS AND DISCUSSION

The absorption spectra of mixed dyestuff solutions which have been cleaned from Mg^{2+} induced dyestuff aggregates were used to determine the concentrations of RD and YD that remained in the respective solution after centrifugation. For this purpose, each spectrum was fitted by a superposition of the spectra of pure RD and pure YD. For the interpretation of the results of this procedure, which are summarized in Figure 2, it is important to ensure that the Mg^{2+} contents used to initiate aggregation within the original mixed dye solutions correspond to a manifold molar excess with respect to each of the dye components. Thus, it can be assumed that aggregation terminated due to a complete consumption of RD and/or YD and not due to a lack of Mg^{2+} . Figure 2 indicates that, up to a mass fraction of 65% RD, RD is consumed almost quantitatively during the aggregation process, since there is no RD left in solution after centrifugation. Besides, the concentration of unconsumed YD decreases linearly with increasing mass fraction of RD. At mass fractions >70% RD, the diagrams continue in an inverted way; i.e., the concentration of unconsumed RD increases linearly with the mass fraction of RD,

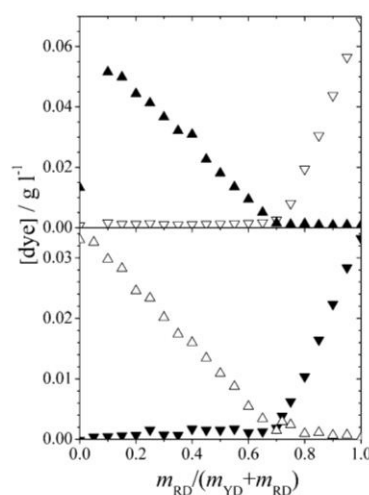


Figure 2. Concentrations of RD and YD in supernatant solutions as a function of the total mass fraction of RD, $m_{RD}/(m_{YD} + m_{RD})$, including dissolved and precipitated dyestuff. The symbols indicate: (▽) and (▲) concentrations of non-aggregated YD and RD where the total dyestuff concentration is 0.066 g L^{-1} and the initial content of Mg^{2+} had been 12.8 mM ; (△) and (▼) concentrations of non-aggregated YD and RD where the total dyestuff concentration is 0.033 g L^{-1} and the initial content of Mg^{2+} had been 6.4 mM .

whereas the fact that virtually no YD is left in the solution after centrifugation indicates that YD is consumed quantitatively during the aggregation process. The point where both RD and YD are consumed quantitatively is characterized by the intersection of the two linearly decreasing branches and denotes the stoichiometric ratio of RD:YD within the formed aggregates. This stoichiometric point is situated between 65 and 70% mass fraction of RD, which corresponds to a molar ratio of RD:YD = 1:1.

The results from light scattering measurements with the solutions of pure RD and pure YD are given in Table 1. The values of M_w and R_g clearly indicate that all dye solutions contain aggregates even in the absence of alkaline earth cations. These are considerably smaller in pure RD solutions than in pure YD solutions. Values of $\rho \geq 2.5$ found for the pure YD solutions are compatible with elongated, cylindrical, rodlike or stiff wormlike structures.⁷ This is also supported by Figure 3, which illustrates that the scattering behavior of YD aggregates can be described adequately by the form factor of polydisperse worm-like chains. Contrarily, lower values of $\rho \approx 1.2$ were detected for the pure RD solutions, suggesting a less anisotropic, more compact or fractal-like structure. Even though the actual form of the particles cannot be determined clearly, the decrease in ρ indicates significant structural differences between the aggregates in pure RD solutions and those in pure YD solutions.

Interestingly, the large YD aggregates disappeared in stoichiometric mixtures of RD and YD (cf. rows 6 and 7 of Table 1). Figure 4 illustrates that the scattering intensity of such a mixture is significantly lower than the sum of scattering intensities of the corresponding pure RD and the pure YD solution. This implies a structural reorganization when solutions of YD and RD are combined.

A technique that shall help to compare the structural features of the components in pure and in mixed dyestuff solutions is LILBID-MS.¹⁴ The spectrum of a solution of pure YD (Figure

Table 1. Results of the Measurements Carried out with Pure RD and Pure YD Solutions^a

sample	c_{mol} (mM)	M_w (10^4 g mol ⁻¹)	R_g (nm)	R_h (nm)	ρ
0.248 g/L RD	0.234	3.2(3)	52(5)	49(7)	1.1(2)
0.083 g/L RD	0.078	2.6(3)	42(7)	30(5)	1.4(4)
1.064 g/L YD	2.107	11.7(10)	155(12)	61(5)	2.5(3)
0.355 g/L YD	0.702	10.6(4)	163(7)	62(7)	2.6(4)
0.118 g/L YD	0.234	10.3(4)	148(8)	60(5)	2.5(3)
0.039 g/L YD	0.078	10.7(9)	169(14)	55(6)	3.1(5)
0.122 g/L 1:1 RD:YD	0.078	2.7(2)	52(6)	43(4)	1.2(2)

^aFor the two highest concentrations of RD (0.75 and 2.24 g/L), no results are shown, since data evaluation was not possible due to a strong absorption of the primary beam. The values of M_w , $R_g = [\langle R_g^2 \rangle]^{1/2}$, and R_h were determined by means of eqs 2 and 4. Values in brackets indicate the uncertainty of the last decimal.

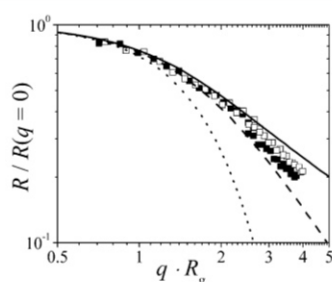


Figure 3. Plot of the form factors $R(q)/R(q=0)$ versus qR_g obtained from aqueous solutions of pure YD in comparison with theoretical scattering curves of different model structures. The symbols indicate: (□) 0.039 g/L pure YD; (■) 0.118 g/L pure YD. The lines represent theoretical scattering curves of polydisperse compact spheres²² (···), flexible worm-like chains²³ (---, ratio of persistence length to weight-averaged contour length = 1:100), and stiff wormlike chains²³ (—, ratio of persistence length to weight-averaged contour length = 2:1). Polydispersity has been accounted for by Schultz–Zimm distributions⁸ of the sphere volume or the contour length of the worm with a relative standard deviation of 50%, respectively.

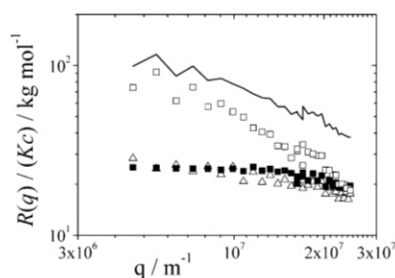


Figure 4. Comparative plot of scattering curves. The symbols indicate: (■) 0.083 g/L pure RD; (□) 0.039 g/L pure YD; (△) 0.122 g/L 1:1 RD:YD. The continuous line represents the sum of (■) and (□).

5A) exhibits increments of approximately 0.5 kDa between neighboring peaks as expected for homoaggregates of YD. These 0.5 kDa increments are accompanied by a smooth intensity distribution that enables the identification of defined peaks up to 14 kDa. The spectrum of the mixed dyestuff solution (Figure 5B) exhibits similar increments of 0.5 kDa; however, its intensity distribution is less smooth than the one found in Figure 5A and peaks can be identified only up to 6 kDa. The latter qualitatively supports the results of the corresponding light scattering experiments shown in Table 1 and Figure 4; i.e., it indicates that the tendency to aggregate is considerably lower for mixed solutions of RD and YD than for pure YD solutions. The

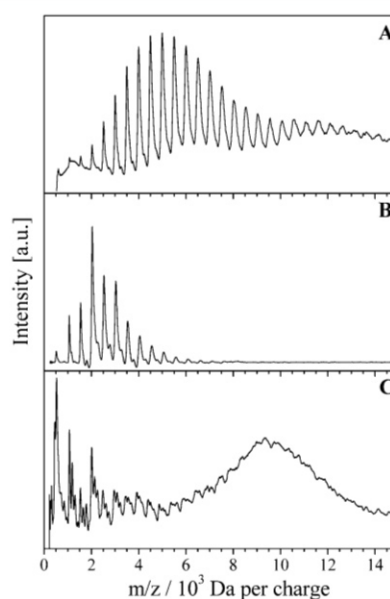


Figure 5. LILBID-MS spectra of dyestuff solutions: (A) 0.132 g/L YD; (B) 0.132 g/L mixed dye in a molar ratio of 1:1; (C) 0.132 g/L mixed dye in a molar ratio of 1:1 in the presence of 0.16 mM MgSO_4 and recorded 50 min after mixing the components.

weakening of aggregation upon addition of RD to RD points to a specific interaction between RD and YD. Whether this interaction already leads to heteroaggregates in the absence of Mg^{2+} cannot be unambiguously established by means of the present LILBID-MS experiments alone. However, LILBID-MS provides the following hints for heteroaggregation even without Mg^{2+} in line with the SLS experiments shown in Figure 4. First and foremost, if the degradation of pure YD aggregates is induced by specific interaction between YD and RD, it is most likely accompanied by the formation of heteroaggregates, though smaller than pure YD aggregates. Second, peaks from solutions of pure YD are fairly weak below $m/z < 4$ kDa. However, it is exactly this regime where peaks from mixed solutions are most intense and contributions to these intensities may stem not only from homoaggregates but also from heteroaggregates. To give but an example, while almost no peak is visible at $m/z = 1.5$ kDa in pure YD solution, an intense peak occurs at this m/z value for solutions of mixed YD and RD. This supports the existence of the species YD_1RD_1 . Due to its higher charge state, RD and its complexes are expected to show greater detection efficiency than YD. This may serve to explain the step-like discontinuity in the

intensity distribution, assigning $m/z = 2000$ mainly to RD_2 and YD_2RD_1 , $m/z = 2500$ to YD_1RD_2 , and $m/z = 3000$ to YD_2RD_2 . However, without higher mass resolution, an assignment solely from the relative intensities remains ambiguous.

The aggregation of the mixed dyestuffs in the presence of Mg^{2+} (Figure 5C) extends to much larger species, while the mixed solution without Mg^{2+} (Figure 5B) shows a distribution with mainly smaller species. The large dyestuff aggregates produced by Mg^{2+} -induced aggregation between YD and RD are on no account resolvable by LILBID-MS due to their low number concentration. A similar observation was recently made for the oligomers of β -amyloid $A\beta_{42}$, where the large species could only be detected by transmission electron microscopy.²⁴ The species remaining in the spectrum shown in Figure 5C would be those that have not yet undergone a Mg^{2+} -induced aggregation ($m/z < 5$ kDa) and fragments of the large aggregates ($m/z > 5$ kDa). This rationalization would agree with the findings from light scattering in the present work.

In order to shed further light on the state of the dye solutions before the addition of Mg^{2+} , a concentration series of stoichiometric mixtures of RD and YD has been investigated by combined SLS and DLS. The results are summarized in Figure 6. Figure 6A demonstrates that, for all four concentrations, the

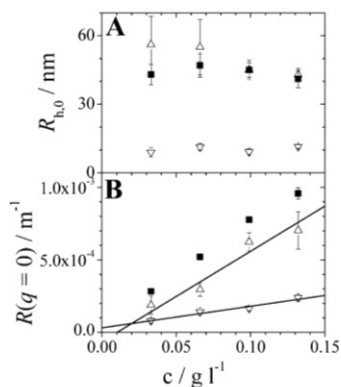


Figure 6. Hydrodynamic radii (A) and zero angle scattering (B) of stoichiometric mixtures of RD and YD as a function of the total dye concentration. Open symbols in both graphs represent results obtained by fitting the intensity correlation function with a double exponential, where (Δ) denotes the slow mode and (∇) denotes the fast mode. Straight lines represent linear extrapolations of $R(q = 0)$ to zero concentration for the two separated modes. The symbols (\blacksquare) represent the z -averaged hydrodynamic radius obtained by means of the cumulant analysis (A) and the total Rayleigh ratio at zero scattering angle (B).

same two diffusive modes are found, one stemming from particles with about 10 nm and the other one with about 50 nm in particle size. The corresponding z -averaged hydrodynamic radius, which was determined by means of cumulant fits (eq 4) covers the entire ensemble of both components and is between 40 and 50 nm. The determination of two modes separated by a factor of 5 in terms of R_h is indeed supported by a CONTIN analysis²¹ of the corresponding DLS data which confirms the bimodal character of the particle size distribution (cf. the Supporting Information). Its significance is further strengthened by the relatively low statistical uncertainties of the hydrodynamic radii and the fact that the same diffusive modes are found for all four concentrations.

In order to estimate the weight fraction of dye molecules and the weight-averaged molar mass for each diffusive mode, we write on the basis of eq 9

$$R_1(q = 0) = Kc_1M_{w,1} \quad (10)$$

$$R_2(q = 0) = Kc_2M_{w,2} \quad (11)$$

where indices “1” and “2” denote the two modes. We now assume a specific correlation of the weight-averaged molar mass with the hydrodynamic radius for the two particle sizes found

$$R_{h,i} \sim M_{w,i}^\alpha; \text{ therefore, } M_{w,1} = M_{w,2} \left(\frac{R_{h,1}}{R_{h,2}} \right)^{1/\alpha} \quad (12)$$

For a given exponent α , eqs 10–12 can be solved with respect to $M_{w,1}$, $M_{w,2}$, c_1 , and c_2 if the total dye concentration $c = c_1 + c_2$ is known. The ρ -value for the mixed RD and YD solutions is about 1.2 (cf. Table 1), suggesting an exponent α which falls in between $1/3 < \alpha < 1/2$.²⁵ The two limiting exponents enable the lower and upper limits of c_1 , c_2 , $M_{w,1}$, and $M_{w,2}$ to be estimated. These limits are indicated in Figure 7 as the relative quantities c_i/c and

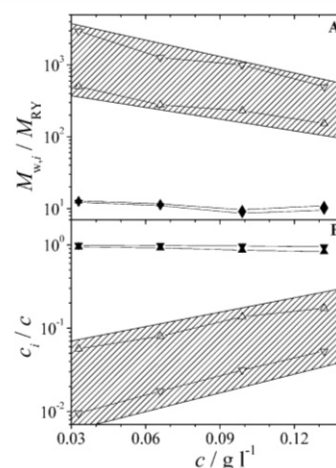


Figure 7. Values of the weight-averaged number of building units per aggregate (A) and the weight fractions of dye molecules (B) that correspond to the two separated diffusive modes found within the solutions of stoichiometric mixtures of RD and YD. A “building unit” is considered as a dimer consisting of one RD molecule and one YD molecule with a total molar mass of $M_{RY} = 1566 \text{ g mol}^{-1}$. The symbols indicate the following: fast mode, $\alpha = 1/2$ (\blacktriangle); fast mode, $\alpha = 1/3$ (\blacktriangledown); slow mode, $\alpha = 1/2$ (\triangle); slow mode, $\alpha = 1/3$ (∇). The values are estimated by means of eqs 10–12.

$M_{w,i}/M_{RY}$ corresponding to the mass fraction and to the degree of polymerization of the mode i , respectively. The degree of polymerization is expressed as a manifold of M_{RY} , which corresponds to the molar mass of a dimer consisting of one RD and one YD molecule (cf. Figure 1). For the slow mode, the corresponding limits form a range which is illustrated as a shaded regime in Figure 7. The results indicate that the weight fraction of the fast mode lies within a range of $80\% < c_1/c < 100\%$, proving that the slow mode only comprises a minor part of the dye monomers. According to Figure 7A, the weight-averaged number of RD-YD-dimers per aggregate $M_{w,i}/M_{RY}$ is about 10 for the fast mode and in between a few hundreds and a few thousands for the slow mode.

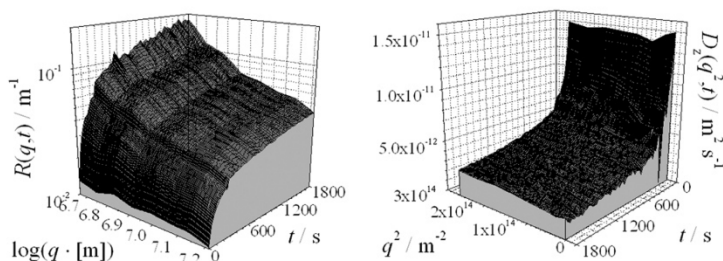


Figure 8. Primary results of time-resolved combined DLS and SLS measurements on a sample containing 0.066 g/L of stoichiometrically mixed RD and YD and 1.63 mM MgSO_4 . The data is represented as the Rayleigh ratio (left-hand side) and z-averaged diffusion coefficient (right-hand side) as functions of momentum transfer and time after the addition of Mg^{2+} , respectively.

On the basis of these experimental findings, mixed solutions of RD and YD with a stoichiometric ratio of 1:1 can be described as a bimodal system where the major part of the dye molecules exists as monomeric and small oligomeric units, while a minor part forms larger aggregates with a size of about 50 nm that contain about 10^3 monomers. Upon an increase of the total dye concentration c , the mass concentration c_2 of these large aggregates increases, yet their size remains unaffected. Together with the fact that the concentration of the particles within the fast mode stays constant, this suggests the existence of dyestuff micelles which correspond to the 50 nm mode and which form above a critical micelle concentration. According to Figure 6B, the critical micelle concentration is probably smaller than 0.05 g/L, yet its value cannot be determined more exactly on the basis of the light scattering data.

Having established the stoichiometry of the Mg^{2+} -induced formation of binary heteroaggregates together with the solution state at the onset of aggregation, we are now well prepared for a further analysis of this heteroaggregation process. To this end, a new technique of time-resolved combined SLS and DLS analysis with a multiangle instrument is applied in situ at the stoichiometric point. The primary results of a time-resolved combined SLS and DLS experiment performed to follow the aggregation of stoichiometrically mixed RD and YD in the presence of Mg^{2+} are shown in Figure 8. Evaluation of these data gives access to R_g , R_h , and M_w as functions of the time. Figure 9 illustrates a continuous increase of the particle size in terms of R_g and R_h , as it has also been shown for R_g in preceding time-resolved SLS experiments on the aggregation of RD and YD.^{5,6} In close agreement with these light scattering results, LILBID-MS data from the same solution also indicate a drastic increase of the

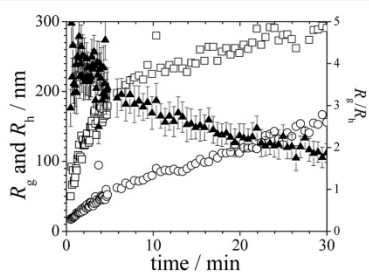


Figure 9. Evolution of the z-averaged radius of gyration R_g (\square), the hydrodynamic radius R_h (\circ), and the shape-sensitive parameter $\rho = R_g/R_h$ with time for a solution containing 0.066 g/L 1:1 RD:YD and 1.63 mM MgSO_4 . R_g was determined by means of eq 2, whereas R_h was evaluated by means of eqs 4 and 5.

propensity to aggregate once Mg^{2+} has been added to the solution of mixed dyestuffs. Like in Figures 5A and 4B, the increment of 0.5 kDa is again recovered and the main peak is shifted to m/z values beyond 10 kDa (Figure 5C).

The combination of SLS and DLS enables the simultaneous evaluation of R_g and R_h and therefore also of ρ . As illustrated in Figure 9, R_h increases less pronounced with time than R_g such that the value of ρ decreases continuously from values >4 to values <2 . A model that is compatible with this ρ -regime and known to be appropriate for the dyestuff system under consideration is the worm-like chain model.⁷ On the basis of this model, the initially large ρ -values suggest the presence of short and stiff, rather rod-like chains. These chains undergo an elongation process, as indicated by the increasing size parameters R_g , R_h , and M_w . The corresponding chain elongation generates increasingly coiled structures, which is compatible with a continuously decreasing ρ -value that drops to about 1.7 within 30 min after initiation of the aggregation process.²⁵

The correlation of M_w and R_g shown in Figure 10 approaches a power law according to

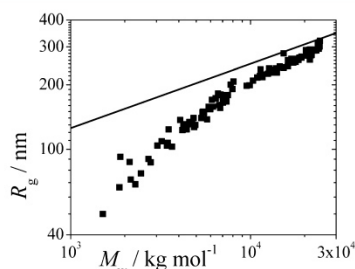


Figure 10. Correlation of z-averaged radius of gyration and weight-averaged molar mass of dye aggregates which grow in the presence of Mg^{2+} (\blacksquare). The straight line represents a power law corresponding to $R_g \sim M_w^{0.3}$.

$$R_g \sim M_w^\alpha \quad (13)$$

with $\alpha = 0.3$. In the light of an anticipated worm-like shape of the growing aggregates, this limiting exponent is unexpectedly low, in close agreement with earlier findings.^{5,6} In order to interpret the exponent of 0.3 and its curved approach from the low molar mass side, we have to consider how the exponent is influenced by the underlying growth mechanism.

If larger particles grew by arbitrary interparticular agglomeration, similar to a polycondensation, one would expect the topological exponents, which is 1 for stiff rods, 0.5 and 0.6 for ideal coils and coils with excluded volume, and 0.33 for compact

spheres or cubes, respectively.²⁶ Thus, the limiting exponent close to 0.3 would suggest an agglomeration of spheres or cubes in a coalescence-like process. However, a formation of three-dimensional compact particles can be excluded due to ρ -values > 1.5 . An alternative mechanism to the coalescence-like agglomeration is that particles grow by a stepwise addition of small building units corresponding to a growth by “monomer addition”. The monomer addition mechanism thereby generates a bimodal system, which influences the two different averaging procedures of R_g^2 and M_w in disparate ways. It could be shown for this alternative way that the exponent α in eq 13 gets smaller by a factor of 2 compared to the value expected from topology.²⁶ This draws our attention immediately to semiflexible chains which exhibit topologically based exponents in a regime of $0.5 \leq \alpha \leq 0.6$.

By combining the exponent of 0.3 with the evolution of R_g/R_h illustrated in Figure 9, we are now able to establish a consistent picture of the dyestuff aggregation under consideration. An exponent that is as small as 0.3 is exclusively compatible with a growth of semiflexible chains by “monomer addition”, whereby the downward bending of the curve toward low molar mass values is due to the impact of chain stiffness.²⁷ The species which are added to the growing chains are possibly reflected by the fast mode found in mixed RD and YD solutions free of Mg^{2+} . However, as the disappearance of the slow mode suggests, the addition of Mg^{2+} may immediately cause drastic structural changes and we may not be able at this point to unambiguously identify the actual (“monomeric”) species that is added to the growing particles.

A closer look at the initial phase of the dye aggregation and a direct comparison of the structural parameters prior to and after the addition of Mg^{2+} to a mixed dyestuff solution are provided by Figure 11. Three features which all refer to the first seconds after

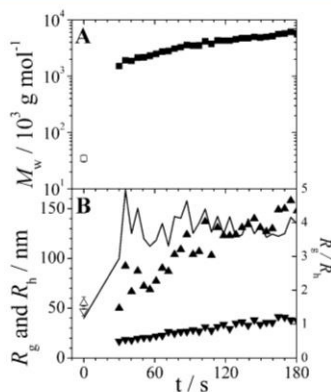


Figure 11. Initial evolution of the data from Figure 9. The symbols indicate the stable state before the addition of Mg^{2+} (\square for M_w , \triangle for R_g , and ∇ for R_h , all shown at $t = 0$) and the time-dependent aggregation after the addition of Mg^{2+} (\blacksquare for M_w , \blacktriangle for R_g , and \blacktriangledown for R_h). The line denotes the trend of R_g/R_h . The values have been extracted from the experimental data by means of eqs 2 and 4.

the addition of Mg^{2+} attract immediate attention: (i) the total scattering intensity, which is proportional to M_w of the entire ensemble including monomers/oligomers and aggregates increases by a factor of about 20, (ii) the value of ρ changes from about 1 to 4, and (iii) the z -averaged hydrodynamic radius decreases from about 50 nm to less than 20 nm.

The decrease in hydrodynamic radius suggests that the small amount of large, micelle-like aggregates which are found in the dye solutions prior to the addition of Mg^{2+} disassembles quickly in the presence of Mg^{2+} . At the same time, the drastic increase of the forward scattering corresponding to the weight-averaged molar mass of the entire ensemble indicates that a large number of new, comparatively small particles are formed, which act as nuclei. The results also support that the major part of dye molecules exists as monomeric and/or small oligomeric units before Mg^{2+} is added (cf. Figures 4 and 5). It is such monomeric and/or oligomeric species which generate the considerable number of anisometric particles with $R_h \approx 20$ nm and $R_g \approx 40$ nm within the first 30 s.

SUMMARY

The investigation of binary dyestuff solutions with different RD:YD ratios that were combined with Mg^{2+} solutions in order to induce self-assembly revealed a coaggregation process of two dyestuffs in aqueous solution. Thereby, we succeeded to identify a 1:1 stoichiometry of RD and YD within the formed coaggregates.

In order to achieve an optimal investigation of the coaggregation at the stoichiometric point, suitable reference data are highly desirable. Consequently, solutions of the pure RD, the pure YD, and mixed solutions containing RD and YD in a molar ratio of 1:1 were investigated by means of LILBID-MS and of combined static and dynamic light scattering. These measurements clearly show that pure and mixed dye solutions already contain aggregates in the absence of Mg^{2+} . The mixed dyestuff solution with a stoichiometric ratio of RD:YD = 1:1 scattered significantly less than the summed-up signals of the two scattering curves that were measured for the pure RD and the pure YD at corresponding concentrations, respectively. These light scattering results together with LILBID-MS data from the same solutions of mixed dyestuffs indicate that structural changes take place when a pure RD solution and a pure YD solution are combined. Possibly, the stoichiometry of RD:YD = 1:1 that was found for the aggregates which had grown in the presence of Mg^{2+} preforms already during these structural changes. DLS measurements with 1:1 mixed dyestuff solutions revealed a bimodal distribution of diffusive modes, with the slower diffusive mode containing only a minor fraction of the total number of dye molecules. This fraction, however, increases significantly with increasing total dye concentration, suggesting that the slow mode consists of micellar aggregates with a critical micelle concentration of less than 0.05 g/L. The major part of the dye molecules is covered by the faster diffusive mode, which comprises single dyestuff molecules and small oligomers thereof.

The self-assembly process that is induced upon the addition of Mg^{2+} to the mixed dyestuff solution was for the first time investigated at the stoichiometric point of RD and YD. The investigation was carried out with a multiangle combined static and dynamic light scattering instrument, which allowed for the simultaneous detection of the scattered light at eight scattering angles and hence for the extrapolation of both the z -averaged diffusion coefficient and the Rayleigh ratio toward $q = 0$. A great benefit from this instrumental improvement compared to former TR-SLS^{5,6} is the gain of a reliable ratio of $\rho = R_g/R_h$ as a function of the time. The evolution of this structure-sensitive quantity indicated a quick formation of elongated structures immediately after the addition of Mg^{2+} to the mixed RD and YD solution. At the same time, the micellar aggregates discernible from a slow diffusive mode before the addition of Mg^{2+} disappeared. With

further progress of the dyestuff aggregation, the growing aggregates exhibit a correlation of R_g and M_w which, in combination with the observed trend of the ρ -ratio, can be unambiguously attributed to the growth of semiflexible chains⁷ by the addition of comparatively small building units.

■ ASSOCIATED CONTENT

● Supporting Information

UV spectra of pure dyestuffs in the presence of Mg^{2+} cations, CONTIN analysis of DLS data from dyestuff mixtures in the absence of Mg^{2+} cations, Zimm plot of yellow dyestuff in the absence of Mg^{2+} cations, outline of data evaluation from combined time-resolved DLS/SLS analysis of Mg^{2+} -induced aggregation, and LILBID-MS spectra from dyestuff solutions containing Mg^{2+} . This material is available free of charge via the Internet at <http://pubs.acs.org>.

■ AUTHOR INFORMATION

Corresponding Author

*E-mail: klaus.huber@upb.de. Phone: +49 5251 602125.

Notes

The authors declare no competing financial interest.

■ REFERENCES

- Haller, R. *Kolloid-Z.* **1918**, *22*, 4.
- Aggregation behaviour of azo dyes has been reviewed by: Edwards, D. J.; Ormerod, A. P.; Tiddy, G. J. T.; Jaber, A. A.; Mahendrasingham, A. In *Physico-Chemical Principles of Colour Chemistry*; Peters, A. T., Freeman, H. S., Eds.; Advances in Colour Chemistry Series, Vol. 4; Blackie Academic & Professional, Chapman & Hall: London, 1996; p 83.
- A good introduction into the field is provided by: Alberst, B.; Bray, D.; Lewis, J.; Raff, M.; Roberts, K.; Watson, J. D. *The Molecular Biology of the Cell*, 3rd ed.; Garland Publishers: New York, 1994 (and references therein).
- Selkoe, D. J. Cell Biology of the Amyloid Beta-Protein Precursor and the Mechanism of Alzheimer's Disease. *Annu. Rev. Cell Biol.* **1994**, *10*, 373–403.
- Escudero Inglés, S.; Katzenstein, A.; Schlenker, W.; Huber, K. Time-Resolved Recording of Ionic Dyestuff Aggregation by Static Light Scattering. *Langmuir* **2000**, *16*, 3010–3018.
- Katzenstein, A.; Huber, K. Model of Polydisperse Wormlike Stars and Its Application to Dyestuff Aggregates. *Langmuir* **2002**, *18*, 7049–7056.
- Kratky, O.; Porod, G. Röntgenuntersuchung Gelöster Fadenmoleküle. *Recl. Trav. Chim. Pays-Bas* **1949**, *68*, 1106–1123.
- Schulz, G. V. Über die Kinetik der Kettenreaktionen. V. Der Einfluss Verschiedener Reaktionsarten auf die Polymolekularität. *Z. Phys. Chem.* **1939**, *B43*, 25–46.
- Lomakin, A.; Chung, D. S.; Benedek, G. B.; Kirschner, D. A.; Teplow, D. B. On the Nucleation and Growth of Amyloid Beta Protein Fibrils: Detection of Nuclei and Quantification of Rate Constants. *Proc. Natl. Acad. Sci. U.S.A.* **1996**, *93*, 1125–1129.
- Lomakin, A.; Teplow, D. B.; Kirschner, D. A.; Benedek, G. B. Kinetic Theory of Fibrillogenesis of Amyloid Beta Protein. *Proc. Natl. Acad. Sci. U.S.A.* **1997**, *94*, 7942–7947.
- Sabaté, R.; Gallardo, M.; Estelrich, J. An Autocatalytic Reaction as a Model for the Kinetics of the Aggregation of Beta-Amyloid. *Biopolymers* **2003**, *71*, 190–195.
- Sabaté, R.; Gallardo, M.; Estelrich, J. Evidence of the Existence of Micelles in the Fibrillogenesis of Beta-Amyloid Peptide. *J. Phys. Chem. B* **2005**, *109*, 11027–11032.
- (a) Egelhaaf, S. U.; Schurtenberger, P. Micelle-to-Vesicle Transition: A Time-Resolved Structural Study. *Phys. Rev. Lett.* **1999**, *82*, 2804–2807. (b) Meng, Z.; Hashmi, S. M.; Elimelech, M. Aggregation Rate and Fractal Dimensions of Fullarene Nanoparticles via Simultaneous Multiangle Static and Dynamic Light Scattering Measurements. *J. Coll. Interf. Sci.* **2013**, *392*, 27–33.
- Morgner, N.; Barth, H. D.; Brutschy, B. A New Way to Detect Noncovalently Bonded Complexes of Biomolecules from Liquid Micro-Droplets by Laser Mass Spectrometry. *Aust. J. Chem.* **2006**, *59*, 109–114.
- Morgner, N.; Kleinschroth, T.; Barth, H. D.; Ludwig, B.; Brutschy, B. A Novel Approach to Analyze Membrane Proteins by Laser Mass Spectrometry: From Protein Subunits to the Integral Complex. *J. Am. Soc. Mass Spectrom.* **2007**, *18*, 1429–1438.
- Hoffmann, J.; Aslimovska, L.; Bamann, Ch.; Glaubitz, C.; Bamberg, E.; Brutschy, B. Studying the Stoichiometries of Membrane Proteins by Mass Spectrometry: Microbial Rhodopsins and a Potassium Ion Channel. *Phys. Chem. Chem. Phys.* **2010**, *12*, 3480–3485.
- Siegert, A. J. F. On the Fluctuations in Signals Returned by Many Independently Moving Scatterers. *MIT Radiation Laboratory Report* **1943**, *465*, 1–14.
- Zimm, B. The Scattering of Light and the Radial Distribution Function of High Polymer Solutions. *J. Chem. Phys.* **1948**, *16*, 1093–1099.
- Zimm, B. Apparatus and Methods for Measurement and Interpretation of the Angular Variation of Light Scattering; Preliminary Results on Polystyrene Solutions. *J. Chem. Phys.* **1948**, *16*, 1099–1116.
- Koppel, D. E. Analysis of Macromolecular Polydispersity in Intensity Correlation Spectroscopy: The Method of Cumulants. *J. Chem. Phys.* **1972**, *57*, 4814–4820.
- Provencher, S. W. A Constrained Regularization Method for Inverting Data Represented by Linear Algebraic or Integral Equations. *Comput. Phys.* **1982**, *27*, 213–227.
- Rayleigh, J. W. S. On the Diffraction of Light by Spheres of Small Relative Index. *Proc. R. Soc. A* **1914**, *90*, 219–225.
- Pedersen, J. S.; Schurtenberger, P. Scattering Functions of Semiflexible Polymers with and without Excluded Volume Effects. *Macromolecules* **1996**, *29*, 7602–7612.
- Cernescu, M.; Stark, T.; Kalden, E.; Kurz, C.; Leuner, K.; Deller, T.; Göbel, M.; Eckert, G. P.; Brutschy, B. LILBID-MS – A Novel Approach to Precisely Monitor the Oligomerization of the Amyloid Beta Peptide. *Anal. Chem.* **2012**, *84*, 5276–5284.
- Burchard, W. Static and Dynamic Light Scattering from Branched Polymers and Biopolymers. *Adv. Polym. Sci.* **1983**, *48*, 1–124.
- Liu, J.; Rieger, J.; Huber, K. Analysis of the Nucleation and Growth of Amorphous $CaCO_3$ by Means of Time-Resolved Static Light Scattering. *Langmuir* **2008**, *24*, 8262–8271.
- Norisuye, T.; Fujita, H. Excluded-Volume Effects in Dilute Polymer-Solutions. 13. Effects of Chain Stiffness. *Polymer Journal* **1982**, *14*, 143–147.

Co-Aggregation of two Anionic Azo Dye-stuffs at a Well-Defined Stoichiometry

Rolf Michels,[†] Thomas Sinemus,[‡] Jan Hofmann,[§] Bernhard Brutschy,[§] and Klaus Huber^{*†}

[†]Universität Paderborn, Department für Physikalische Chemie, Warburger Straße 100, D-33098 Paderborn, Germany

[‡]Berufliche Schulen Korbach und Bad Arolsen, Kasseler Straße 17, D-34497 Korbach, Germany [§]Goethe Universität Frankfurt, Institut für Physikalische und Theoretische Chemie, Max-von-Laue-Str. 7, D-60438 Frankfurt am Main, Germany

*to whom correspondence should be addressed

E-mail: klaus.huber@upb.de

Phone: +49 5251 602125

Supporting Information

SUPPORTING INFORMATION. UV-spectra of pure dye-stuffs in the presence of Mg^{2+} cations; CONTIN-analysis of DLS data from dye-stuff mixtures in the absence of Mg^{2+} cations; Zimm-plot of yellow dye-stuff in the absence of Mg^{2+} cations; outline of data evaluation from combined time-resolved DLS/SLS analysis of Mg^{2+} -induced aggregation; LILBID-MS spectra from. This material is available free of charge via the Internet at <http://pubs.acs.org>.

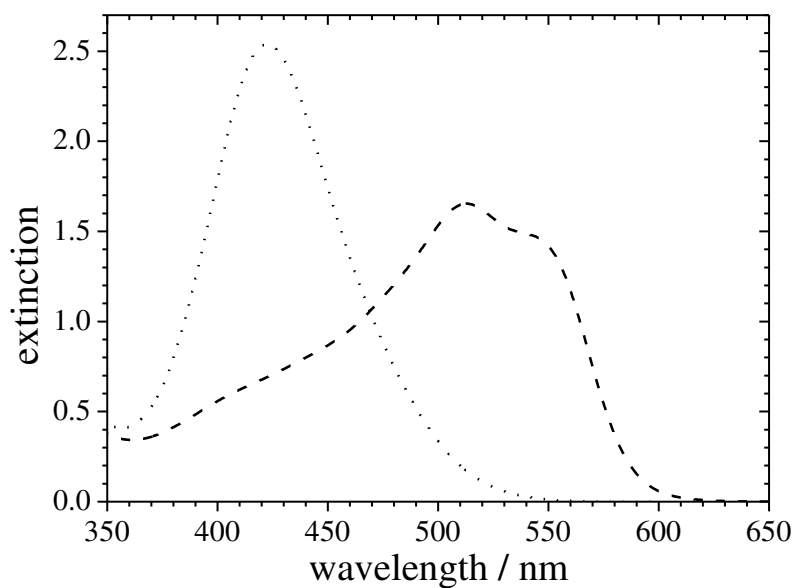


Figure SI-1. Absorption spectra of the pure RD (---) and pure YD (···).

Table SI-1. Extinction coefficients of the RD and YD in aqueous solutions containing Mg^{2+} measured at a wavelength of 633 nm.

dyestuff	$[\text{Mg}^{2+}] / \text{mM}$	ext. coef. / $\text{m}^2 \text{mol}^{-1}$
RD	6.4	4179
RD	12.8	4393
YD	6.4	5255
YD	12.8	5077

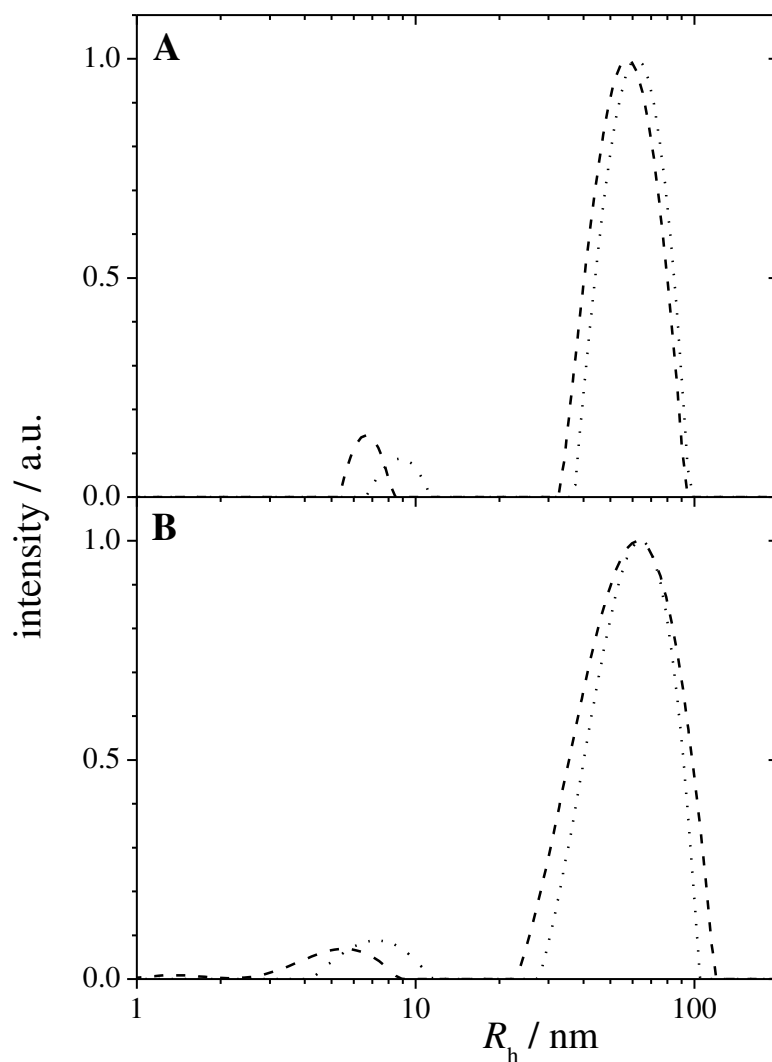


Figure SI-2. Size distributions of dyestuff particles in the absence of Mg^{2+} . The distributions have been calculated by means of the CONTIN analysis¹ of the corresponding intensity correlation functions obtained by DLS. Figure A shows the results for a solution of 0.066 g/l of mixed RD and YD at a ratio of 1:1; Figure B shows the results for a solution of 0.132 g/l of mixed RD and YD at a ratio of 1:1. The dashed lines stem from correlation functions measured at a scattering angle of $\theta = 60^\circ$, the dotted lines stem from measurements at $\theta = 20^\circ$.

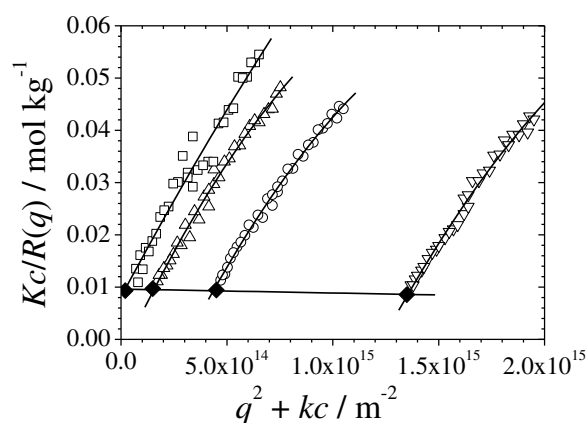


Figure SI-3. Zimm plot² measured with solutions of pure YD in the absence of magnesium ions. The second virial coefficient is close to zero for the YD aggregates.

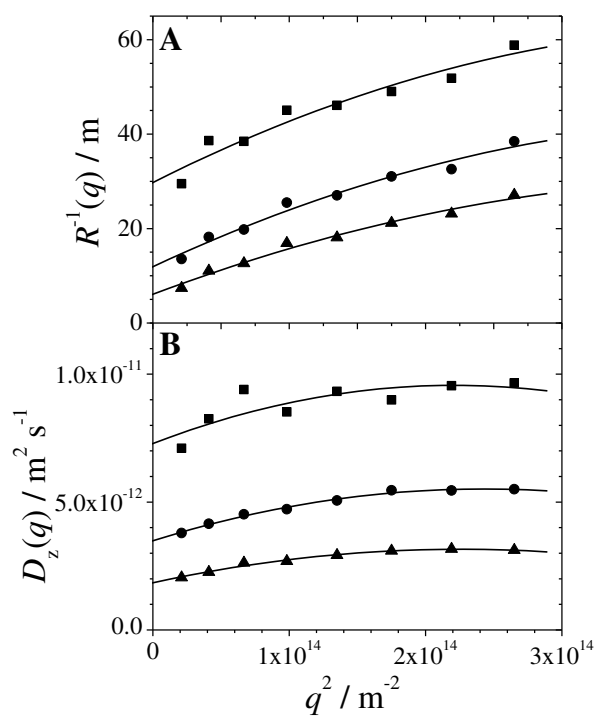


Figure SI-4. Evaluation of data from time-resolved combined static and dynamic light scattering exemplified with three selected curves. Inverse Rayleigh Ratios (A) and z-averaged diffusion coefficients (B) have been extrapolated towards zero momentum transfer q by means of 2nd order polynomials (straight lines). The sample contained 0.066 g/l stoichiometrically mixed RD and YD and 1.63 mM MgSO_4 . Symbols indicate different times after the addition of Mg^{2+} to the mixed dyestuff solution, corresponding to 100 s (■), 350 s (●) and 1200 s (▲).

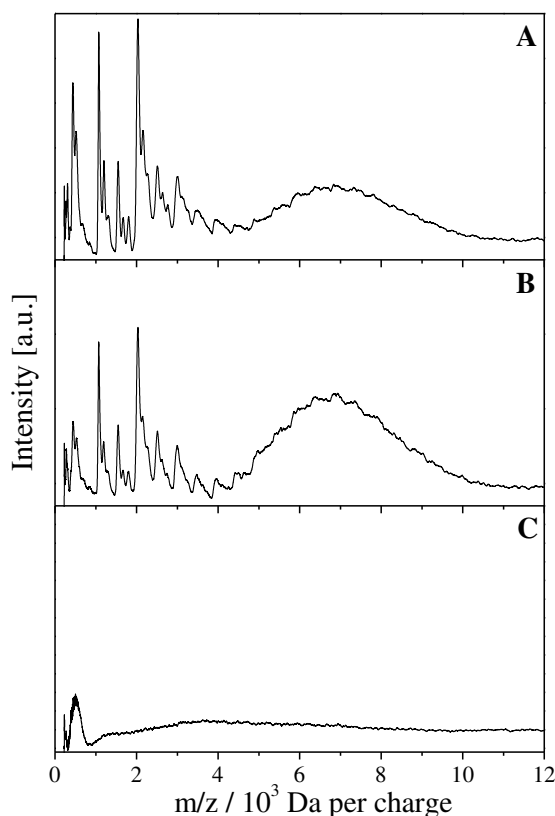


Figure SI-5. LILBID-MS spectra of aqueous solutions containing 0.132 g/l (~ 0.08 mM) stoichiometrically mixed RD and YD in the presence of Mg^{2+} . The spectra shown in Figures (A) and (B) were measured with a sample containing 0.08 mM MgSO_4 and the spectra were recorded 7 minutes (A) and 26 minutes (B) after the aggregation process had been initiated by adding the MgSO_4 solution to the mixed dye solution. In Figure (C), the solution contained 0.4 mM MgSO_4 and the spectrum was recorded 12 minutes after initiation of the aggregation. The intensity of the broad peak located at $5000 < m/z < 10000$ in Figures (A) and (B) changes over time with respect to the sharper peaks at $m/z < 4000$, thereby suggesting the consumption of small dyestuff oligomers in favor of larger ones. Figure (C) illustrates that for the dyestuff aggregation under consideration, no significant peaks are detected at Mg^{2+} contents of 0.4 mM or higher.

References.

1. Provencher, S. W. *Comput. Phys.* **1982**, 27, 213.
2. Zimm, B. J. *Chem. Phys.* **1948**, 16, 1093. Zimm, B. J. *Chem. Phys.* **1948**, 16, 1099.

5. Kinetic and Structural Features of a Dyestuff Coaggregation Studied by Time-Resolved Static Light Scattering

Reproduced with permission from *J. Phys. Chem. B* **2013**, *117*, 15165-15175.
Copyright 2013 American Chemical Society.

Kinetic and Structural Features of a Dyestuff Coaggregation Studied by Time-Resolved Static Light Scattering

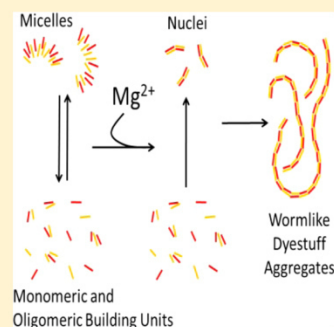
Rolf Michels,[†] Yvonne Hertle,[‡] Thomas Hellweg,[‡] and Klaus Huber^{*,†}

[†]Physikalische Chemie, Universität Paderborn, Warburger Straße 100, D-33098 Paderborn, Germany

[‡]Physikalische und Biophysikalische Chemie, Universität Bielefeld, Universitätsstraße 25, D-33615 Bielefeld, Germany

Supporting Information

ABSTRACT: A binary dyestuff aggregate with a distinct stoichiometry is formed in dilute aqueous solution upon addition of Mg^{2+} ions. The aggregation process was investigated with time-resolved multiangle static light scattering resulting in a sequence of static scattering curves. The scattering curves were analyzed with respect to the aggregation kinetics as well as the structure of the growing aggregates. The aggregation kinetics was based on the time evolution of the weight-averaged molar mass values extracted from the intercepts of the static scattering curves. A kinetic model that considers solely a nucleation step and monomer addition in its most simple form was developed in order to describe the evolution of time-dependent mass data. In addition, a kinetic model introduced by Lomakin et al. (*Proc. Natl. Acad. Sci. U.S.A.* **1996**, *93*, 1125) for the description of β -amyloid aggregation was adapted to the same experimental data. Application of the two kinetic models offered significant information on the role of magnesium ions within the aggregation process and provided a deeper understanding of the aggregation mechanism. Correlation of the size parameters extracted from the initial slopes of the scattering curves with the respective mass data as well as direct fitting of the scattering curves with the wormlike chain model yield a consistent set of model parameters.



INTRODUCTION

Organic azo-dyestuff molecules are usually equipped with polar groups, ionic groups, and hydrophobic residues. The resulting molecular architectures lend the molecules a marginal solubility in water in combination with a suitable affinity to substrates like textiles or paper.¹ Whereas the competition between the tendency to aggregate in solution and to adsorb from solution onto substrates is interesting from a technical point of view, the phenomenon of dyestuff aggregation provides an even broader relevance in fundamental science. This relevance stems from a structural similarity between dyestuff molecules and proteins, which is originated in the common feature of a combination of ionic and polar groups with hydrophobic patches in both classes of molecules. Like in the case of dyestuffs, this set of structural features manifests itself in a large variety of aggregating proteins in biological systems. Among them are systems indispensable for the survival of the hosting biological individuals like blood-clotting^{2,3} connected with the aggregation of fibrin or like the reversible aggregation of proteins in the cytoplasm⁴ including the formation of actin fibers or tubes from tubulin with the latter providing roads for intracellular transportation. Other aggregation processes of proteins are undesired or even live threatening to the respective biological individuals. To give but an example, amyloidosis is a signature of several neuronal diseases like Alzheimer's dementia.⁵

In preceding contributions,^{6–8} we could identify a binary mixture of two azo-dyestuffs, a red (RD) and a yellow anionic dye (YD), which form fiberlike composite aggregates upon

addition of Mg^{2+} cations to a dilute aqueous solution of the two dyestuffs. The major achievements have been established by a new technique of time-resolved multiangle static light scattering⁹ and are similar to two contributions published recently on fibrin aggregation¹⁰ and on β -amyloid.¹¹ The morphological features of the RD-YD-aggregates, established by light scattering, exhibit striking similarities to results extracted for fiberlike protein aggregates.^{10–15}

Progress in light scattering instrumentation^{8–10} results in detailed time-resolved data and meanwhile generates a need for suitable kinetic relationships, capable of reproducing the evolution of particle mass and size with time. An excellent overview on the achievements in interpreting particle nucleation and growth including the formation of fiberlike aggregates is provided by Finke et al.^{16–18} The authors established a kinetic scheme denoted as “2-Step Minimal/Ockham's Razor model”,^{17,18} which leads to a simple set of equations describing the consumption of monomers and the increase in mass fraction of the particles/aggregates. This set of equations turned out to successfully fit experimental data such as time-dependencies of aggregate concentrations for a large number of growing systems, but in general it is inadequate to satisfactorily reproduce scattering data of the same systems for the following reasons. In the simplest case, the scattering

Received: May 27, 2013

Revised: October 30, 2013

Published: October 31, 2013

intensity at zero scattering angle is proportional to the product of the concentration and the averaged molar mass of the scattering particles. For larger particles and/or higher concentrations, the scattering signal recorded at finite scattering angles (i.e., finite momentum transfer values q) is modulated by the formfactor and/or a structure factor. Hence, a direct correlation of the scattering signal with the concentration of aggregates according to the 2-Step Minimal/Ockham's Razor model^{17,18} is possible only under specific circumstances, which are rarely met. An example where the circumstances meet the respective requirements is an ensemble of growing fiberlike aggregates, which have a constant cross section and which are longer than the inverse of the momentum transfer q applied in the experiment.^{19,20} Kinetic interpretation of refined scattering data like the increase of the weight averaged molar mass of the particles growing with time is entirely impossible with the 2-Step Minimal/Ockham's Razor model.^{17,18}

First significant achievements in this direction could be provided by Lomakin et al.^{14,21} and Murphy et al.¹⁵ who investigated the growth of β -amyloid fibers at pH = 2 and at pH = 7.4, respectively. Both research groups used a nucleation step followed by fiber elongation and developed differential equations for the variation of the moments of the molar mass distribution of the fibrils. While the two models are based on two different nucleation steps, the elongation steps in the model of Murphy et al.¹⁵ differ from the elongation steps in the model of Lomakin et al.²¹ only in that the former are reversible and the latter are irreversible. Lomakin et al.²¹ could extract an analytical expression for the evolution of the weight-averaged particle mass with time. Murphy et al.¹⁵ solved the evolution of the moments numerically in order to predict the growing averages of the mass and size distribution of fibers with time. Unfortunately, neither of the authors had available an instrumentation which gave direct access to the evolution of weight averaged particle mass data with time. Both groups were forced instead to use dynamic and static light scattering data recorded at a single observation angle and to adjust the results to the model parameters by means of complex transformations and various assumptions. Lomakin et al.²¹ translated the lengths of growing β -amyloid fibers into an averaged hydrodynamically effective radius to be compared with time-resolved single-angle dynamic light scattering data. To this end, the authors had to assume two simplifications, namely monodispersity and a stiff rodlike shape of the growing β -amyloid fibers. In the work published by Murphy et al.,¹⁵ the numerically established distribution of the evolving fiber mass and size in combination with the application of suitable wormlike chain parameters prepared the model to be fitted to experimentally determined hydrodynamic radii and static scattering intensities, established at an angle of 90°.

At this point, we have to draw the reader's attention to a simpler model for the formation of chainlike aggregates, the so-called irreversible protein aggregation introduced by Roberts.²² Herein, the nucleation step consists solely in the irreversible transformation of a monomer into a nucleus and is therefore less complicated than the nucleation described by Lomakin et al.²¹ In what follows, we start to interpret our static light scattering data with the model used by Roberts,²² denoted herein as irreversible nucleation-elongation (INE) model. This interpretation shall be complemented by also applying the more complex kinetic model published by Lomakin et al.²¹ Unlike to former analysis of scattering data with kinetic models^{15,21} mentioned above, the present work is able to make

available time-resolved weight averaged mass values, which could thus be directly compared with theoretical values established with the kinetic models, without making any further transformations or assumptions with respect to particle morphology. Application of these kinetic models to the formation of RD-YD-heteroaggregates under present consideration has been made possible by a preceding study⁸ revealing several mechanistic details of this dyestuff heteroaggregation with the most striking feature being a 1:1 stoichiometry of RD/YD. The state of the dissolved dyestuff mixture prior to the onset of the aggregation, that is, prior to the moment when magnesium cations are added, constitutes a solution wherein about 90% of RD and YD are existent as monomeric and small oligomeric units, and the remaining 10% form micellar aggregates with about 10³ dye molecules per aggregate. Most likely, the dyestuff oligomers and possibly also the micelles already exhibit the 1:1 stoichiometric ratio of RD/YD that is found for the aggregates that form in the presence of Mg²⁺.

In order to establish a suitable set of experimental data, we performed time-resolved multiangle static light scattering at four different concentrations of the dyestuff mixture at the stoichiometric ratio of RD/YD = 1:1. In this series of experiments, the initiating Mg²⁺ content was kept constant. In a second series of time-resolved experiments, the initiating Mg²⁺ content was varied at a constant concentration of the stoichiometric dyestuff mixture. Modeling the experimental data by means of the INE model could not explain the origin of the growing dyestuff particles adequately and hence pointed to a more complex process. First aspects from this complex process could be revealed by an application of the scheme established by Lomakin et al.,²¹ which assumes the nucleation of growing fibers from micelles. The choice of the Lomakin model²¹ for the dyestuff aggregation under consideration was inspired by our preceding study⁸ of the initial states of the process that suggested the occurrence of micellar aggregates prior to the addition of Mg²⁺. Finally, results from the kinetic interpretation of the data will be compared with a detailed analysis of the same data with the wormlike chain model. To this end, concepts could be applied that turned out to be highly significant in preceding studies on time-resolved aggregation experiments with fibers.^{6,7,11} This joint use of kinetic and structural models does not only reveal a consistent model interpretation, but it also provides further mechanistic details, which complement the preceding work.^{6,7}

EXPERIMENTS AND DATA TREATMENT

Materials. Figure 1 shows the chemical structures of the two dyes used. Dyestuffs were received as a donation from Ciba Geigy, Switzerland. They were available as sodium salts and purified by dialysis as described in the preceding article.⁶ Magnesium sulfate (assay >99.5%) was purchased from Sigma-Aldrich.

Transmission Electron Microscopy (TEM). The micrographs were taken using a CM100 (PW6021) microscope (Philips, acceleration voltage of 80 kV). The specimen were prepared on copper-grids (Science Services, carbon only, 200 μ m mesh) at room temperature. For the TEM measurements, 3 μ L of a sample solution were dropped on the copper-grid and after one minute the residual solvent was blotted off with a filter paper.

Preparation of Light Scattering Experiments. A solution containing 4.47 g/L RD and 2.13 g/L YD, resulting in an overall dye concentration of 6.6 g/L (molar ratio RD/YD

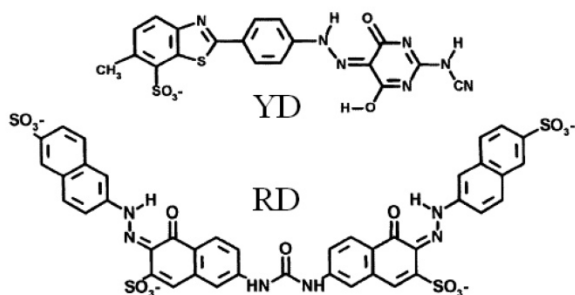


Figure 1. Molecular structures of the two azo dyes. YD denotes the yellow dye and RD denotes the red dye.

= 1:1) and a solution containing 13 mM MgSO_4 were prepared in distilled water. These solutions served as stock solutions and were further diluted in order to achieve the concentrations desired for the time-resolved static light scattering experiments. For the preparation of stock solutions, the required amounts of pure solids were weighed into volumetric flasks and the appropriate amounts of distilled water were successively added. Each self-assembly process discussed within the present article was initiated by hand-mixing of the two components. For this purpose, 3 mL of a dye solution and 3 mL of a MgSO_4 solution were injected simultaneously into a scattering cuvette through syringe filters (Macherey-Nagel CHROMAFIL PET-20/25, 1.2 μm pore size). Filtration removed dust particles from the solutions. The start of each process was defined as the time when 1.5 mL of each syringe had entered the cuvette. All dyestuff solutions had a pH value of 6.7 independent of the dyestuff concentration.

Time-Resolved Static Light Scattering (TR-SLS). Cylindrical quartz cuvettes from Helma with a diameter of 20 mm were used as scattering cells. Prior to any measurement, cuvettes were cleaned from dust by continuously injecting freshly distilled acetone from below for 5 min. TR-SLS measurements were carried out with a home-built multiangle instrument that had been developed by Becker and Schmidt.⁹ All measurements were performed at a temperature of 25 °C. A He–Ne-Laser from Melles Griot, operating at a wavelength of $\lambda = 632.8$ nm, served as light source. The scattering signal was detected within an angular range of $25.8^\circ < \theta < 143.1^\circ$, corresponding to a q -regime of $4.6 \times 10^{-3} \text{ nm}^{-1} < q < 2.5 \times 10^{-2} \text{ nm}^{-1}$, where

$$q = \frac{4\pi n}{\lambda} \sin\left(\frac{\theta}{2}\right) \quad (1)$$

is the scattering vector and n is the refractive index of the solvent. As a primary result from any scattering measurement, the time-dependent Rayleigh ratio of the aggregating sample

$$R(q, t) = \frac{S_{\text{sample}}(q, t) - S_{\text{solvent}}(q)}{S_{\text{standard}}(q)} R_{\text{standard}} \quad (2)$$

was calculated. In eq 2, $S_{\text{sample}}(q, t)$ is the time-dependent scattering signal of a mixed dyestuff solution activated with Mg^{2+} cations, R_{standard} is the absolute Rayleigh ratio of toluene, and $S_{\text{solvent}}(q)$ and $S_{\text{standard}}(q)$ are the scattering signals of the solvent (water) and the standard (toluene), respectively. In order to obtain the particle scattering factor $P(q)$ from the Rayleigh ratio, $R(q)$ was divided by its extrapolation to zero scattering vector q .

$$P(q) = \frac{R(q)}{\lim_{q \rightarrow 0} R(q)} \quad (3)$$

For the experiments discussed within the present work, the concentration of dye aggregates was not constant. Therefore, we had to refrain from an extrapolation of $R(q, t)$ to zero concentration. However, the use of dye concentrations smaller than 0.1 g/L justifies this approximation and makes the consideration of scattering contributions stemming from interparticular interferences (structure factor) obsolete.

Determination of Model-Independent Size Parameters. The limit of the Rayleigh ratio at zero scattering vector can be represented as a product of the scattering contrast K , the mass concentration c of the dyestuff and the weight-averaged molar mass M_w of the solute.

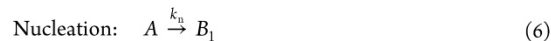
$$\lim_{q \rightarrow 0} R(q) = KcM_w \quad (4)$$

For the determination of the model-independent parameters, we established the Rayleigh ratio at low q according to an extended Zimm approximation^{23,24} given by

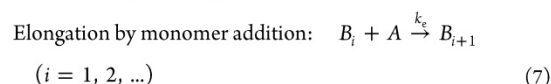
$$\frac{Kc}{R(q)} = \frac{1}{M_w} + \frac{\langle R_g^2 \rangle_z}{3M_w} q^2 + \nu q^4 \quad (5)$$

wherein the quantity ν served as a fitting parameter only and was not considered any further. It was demonstrated in preceding works^{6,11,25} that this approximation holds up to $q^2 \langle R_g^2 \rangle_z = 4$ for the scattering patterns of semiflexible chains. Its application makes the apparent weight-averaged molar mass M_w and the z -averaged square radius of gyration $\langle R_g^2 \rangle_z$ of the solute accessible from fitting $Kc/R(q)$ by a quadratic polynomial if the scattering contrast and the concentration are known.

Determination of Kinetic Parameters. We consider a simple kinetic model consisting of two fundamental steps. In a nucleation step, a monomeric species A transforms into a nucleus B_1 .



B_1 is capable of adding further monomers via a nonlimited number of elongation steps.



In the following, this model will be denoted as irreversible nucleation-elongation (INE) model. The particles that are in the focus of this work are expected to exhibit a wormlike shape. Therefore, the number of growing sites per particle and the rate constant of elongation, k_e , are assumed to be independent of the degree of polymerization i of the growing species B_i . The change in number concentration of B_i with time t can thus be written as

$$\frac{d[B_i]}{dt} = k_n[A]\delta_{i1} + k_e[A]((1 - \delta_{i1})[B_{i-1}] - [B_i]) \quad (8)$$

Here, $[A]$ and $[B_i]$ are the number concentrations of unconsumed monomers A and of growing particles B_i with degree of polymerization i , respectively, and δ represents the Kronecker-Delta.

We will now establish the first three moments of the ensemble of growing species for the INE model. This route is similar to the one followed by Lomakin et al.²¹ in order to

describe fiber formation in a solution of monomers which equilibrate with micelles. As we will show, this will allow for the prediction of the weight-averaged molar mass M_w accessible by static light scattering. The k^{th} moment of the ensemble can be written as

$$[B]^{(k)} = \sum_i i^k [B_i] \quad (9)$$

Multiplication of eq 8 with i^k and subsequent summation over all i yield a set of recursive equations that define the change of the k^{th} moment with time.

$$\frac{d[B]^{(k)}}{dt} = k_n[A] + k_e[A] \sum_{j=0}^{k-1} \binom{k}{j} [B]^{(j)} \quad (10)$$

Accordingly, the first two moments ($k = 0$ and $k = 1$) are expressed as follows.

$$\frac{d[B]^{(0)}}{dt} = k_n[A] \quad (11)$$

$$\frac{d[B]^{(1)}}{dt} = k_n[A] + k_e[A][B]^{(0)} \quad (12)$$

Equations 11 and 12 nicely demonstrate that the number concentration of all growing particles $[B]^{(0)}$ changes only as a consequence of nucleation, whereas the total concentration of monomers within the growing particles $[B]^{(1)}$ changes due to nucleation as well as elongation. If we further take into account the constant total concentration of monomers

$$[A]_{\text{tot}} = [A](t) + [B]^{(1)}(t) \quad (13)$$

we obtain a set of equations of the state variables $[A]$, $[B]^{(0)}$, and $[B]^{(1)}$ that can be solved analytically. For this purpose, $[A]$ and $[B]^{(1)}$ as well as their derivatives are eliminated from eqs 11–13 in favor of $[B]^{(0)}$ and its derivatives.

$$\frac{d^2[B]^{(0)}}{dt^2} + k_n \frac{d[B]^{(0)}}{dt} + k_e B^{(0)} \frac{d[B]^{(0)}}{dt} = 0 \quad (14)$$

The solution of eq 14 can be written as

$$[B]^{(0)}(t) = \frac{1}{k_e} (\sqrt{2} c_1 f(t) - k_n) \quad (15)$$

with

$$f(t) = \tanh\left(\frac{c_1 t}{\sqrt{2}} + c_2\right) \quad (16)$$

$$c_1 = \sqrt{\frac{1}{2} ((k_e [B]_{t=0}^{(0)})^2 + 2k_n k_e [B]_{t=0}^{(0)} + k_n^2 + 2k_n k_e ([A]_{\text{tot}} - p_0 [B]_{t=0}^{(0)}))} \quad (17)$$

$$c_2 = \operatorname{arctanh}\left(\frac{k_e [B]_{t=0}^{(0)} + k_n}{\sqrt{2} c_1}\right) \quad (18)$$

As indicated in eqs 17 and 18, eq 14 was solved for the general case including an initial number of aggregates $[B]_{t=0}^{(0)}$ with number-averaged degree of polymerization p_0 that are capable of growing from $t = 0$ on.

Time-resolved multiangle static light scattering provides the evolution of the molar mass M_w , which is a weight-average over all species including monomers and growing aggregates. It can be expressed as the sum of the monomer concentration $[A](t)$

and the second moment of the ensemble of growing aggregates $[B]^{(2)}(t)$

$$M_w(t) = \frac{M_A}{[A]_{\text{tot}}} ([A](t) + [B]^{(2)}(t)) \quad (19)$$

with M_A the molar mass of a monomeric unit A .

The time-dependent evolution of the monomer concentration $[A](t)$ required in eq 19 can be calculated by inserting $[B]^{(0)}(t)$ given by eq 15 into eq 12 and solving eqs 12 and 13 to yield $[A](t)$ and $[B]^{(1)}(t)$

$$[A](t) = \frac{c_1^2}{k_n k_e} (1 - f^2(t)) \quad (20)$$

The remaining step in order to make eq 19 applicable is the calculation of the second moment $[B]^{(2)}(t)$, which can be determined using eqs 10 and 13.

$$\begin{aligned} [B]^{(2)}(t) &= [B]_{t=0}^{(2)} + \int_0^t [A](t') \\ &\quad (k_n + k_e ([B]^{(0)}(t') + 2([A]_{\text{tot}} - [A](t')))) dt' \\ &= [B]_{t=0}^{(2)} + \frac{c_1^2(t)}{6k_n^2 k_e} (12\sqrt{2} (k_n k_e [A]_{\text{tot}} - c_1^2) + 6k_n c_1 f(t) \\ &\quad + 4\sqrt{2} c_1^2 f^2(t)) - I_0 \end{aligned} \quad (21)$$

where

$$I_0 = \frac{c_1(c_3 + c_4 + c_5)}{3k_n^2 k_e (1 + e^{6c_2} + 3e^{4c_2} + 3e^{2c_2})} \quad (22)$$

$$c_3 = 3k_n c_1 (1 + e^{6c_2} - e^{2c_2} - e^{4c_2}) \quad (23)$$

$$c_4 = 6\sqrt{2} k_n k_e C (e^{4c_2} + e^{6c_2} - e^{2c_2} - 1) \quad (24)$$

$$c_5 = 4\sqrt{2} c_1^2 (1 - e^{6c_2} - 3e^{4c_2} + 3e^{2c_2}) \quad (25)$$

In eq 21, the term $[B]_{t=0}^{(2)}$ considers initial aggregates already existing at $t = 0$. As will be shown, $[B]_{t=0}^{(2)}$ can be expressed as a function of the number concentration $[B]_{t=0}^{(0)}$ of initial aggregates, their number-averaged degree of polymerization p_0 , and their polydispersity $\text{PD}_{t=0}$. The assumption of initial aggregates, that is, $[B]_{t=0}^{(0)} > 0$ and $p_0 > 1$, can account for seeds or for a nucleation burst. Neither of these two features would be considered by simply setting $[B]_{t=0}^{(0)} = [B]_{t=0}^{(1)} = [B]_{t=0}^{(2)} = 0$, thereby attributing the origin of all growing aggregates to a continuous nucleation as described by eq 6.

The polydispersity $\text{PD}(t)$ of the aggregates can at any time t be expressed as the ratio of the weight-averaged molar mass $M_{w,\text{ag}}$ and the number-averaged molar mass $M_{n,\text{ag}}$ of the existing aggregates.

$$\text{PD}(t) = \frac{M_{w,\text{ag}}(t)}{M_{n,\text{ag}}(t)} = \frac{[B]^{(0)}(t)[B]^{(2)}(t)}{[B]^{(1)}(t)[B]^{(1)}(t)} \quad (26)$$

Combination of eq 26 at $t = 0$ with the number-averaged degree of polymerization p_0 of the initial aggregates and the respective polydispersity $\text{PD}_{t=0}$ yields the second moment at $t = 0$ as

$$[B]_{t=0}^{(1)} = p_0 [B]_{t=0}^{(0)} \quad \text{and} \quad [B]_{t=0}^{(2)} = p_0^2 \text{PD}_{t=0} [B]_{t=0}^{(0)} \quad (27)$$

together with the polydispersity $\text{PD}_{t=0}$ and Having established the solutions for $A(t)$ and $[B]^{(2)}(t)$ given by eqs 20 and 21, eq

19 can be fitted to the experimental data by variation of one or several of the parameters M_A , k_w , k_e , p_0 , $PD_{t=0}$ and $[B]_{t=0}^{(0)}$.

A limiting case of the INE model that turned out to be relevant for the present work arises by prohibiting continuous nucleation as described by eq 6. Thereby, the zeroth moment keeps the constant value of $[B]_{t=0}^{(0)}$ and the higher moments increase solely due to the addition of monomers to the initial aggregates. For this case

$$[A](t) = ([A]_{\text{tot}} - p_0[B]_{t=0}^{(0)})\exp(-k_e[B]_{t=0}^{(0)}t) \quad (28)$$

$$[B]^{(2)}(t) = c_6 + c_7 \exp(-k_e[B]_{t=0}^{(0)}t) + c_8 \exp(-2k_e[B]_{t=0}^{(0)}t) \quad (29)$$

with

$$c_6 = \frac{[A]_{\text{tot}}^2}{[B]_{t=0}^{(0)}} - p_0[B]_{t=0}^{(0)} + [A]_{\text{tot}}[B]_{t=0}^{(0)} - p_0^2[B]_{t=0}^{(0)} + p_0^2[B]_{t=0}^{(0)}PD_{t=0} \quad (30)$$

$$c_7 = 2p_0[A]_{\text{tot}} - \frac{2[A]_{\text{tot}}^2}{[B]_{t=0}^{(0)}} + p_0[B]_{t=0}^{(0)} - [A]_{\text{tot}} \quad (31)$$

$$c_8 = p_0^2[B]_{t=0}^{(0)} - 2p_0[A]_{\text{tot}} + \frac{[A]_{\text{tot}}^2}{[B]_{t=0}^{(0)}} \quad (32)$$

We followed a route similar to the one just outlined for the INE model in order to also describe the evolution of the weight-averaged molar mass for the Lomakin model.²¹ For this purpose, the crucial steps leading to expressions that are analogous to eqs 19 and 21 are outlined in the Supporting Information.

For all fits with both kinetic models, the molar mass of a monomeric unit M_A was set to $1451 \text{ g mol}^{-1} + 2.5 M_{\text{Mg}} = 1512 \text{ g mol}^{-1}$. Here, the first term is equal to the sum of the molar masses of the anionic RD and YD, and the second term corresponds to the molar mass of magnesium ions required to neutralize the total negative charge of a red and a yellow dye anion. It is important to note that the choice of the monomeric unit, and therefore of M_A , will not have any influence on the interpretation of kinetic data within the present article because M_A solely represents a scaling factor between the experimental data and the model (cf. eq 19).

Determination of Wormlike Chain Parameters. It is well established²⁶ that aggregates formed by dyestuffs exhibit fiberlike structures. This is also the case for the system under consideration.^{6–8} A suitable model to describe the behavior of fiberlike structures is the wormlike chain model introduced by Kratky and Porod.²⁷ It is based on two parameters, the contour length L corresponding to the overall length of the semiflexible chain, and the persistence length l_p as a measure of the chain stiffness. The rigid rod limit and the random coil limit are captured at $L/l_p \rightarrow 0$ and $L/l_p \rightarrow \infty$, respectively. Form factors of wormlike chains can be satisfactorily reproduced by means of the approximate formula given by Pedersen and Schurtenberger.²⁸

In our present work, estimation of contour lengths and persistence lengths of dye aggregates shall be carried out in two different ways. The first way uses the q^{-1} dependency of wormlike chain form factors at intermediate q -regime from which the weight-averaged contour length L_w can be

determined using so-called bended-rod-plots²⁹ of the type $qP(q)$ versus q .

$$qP(q)l_{\text{plateau}} = \frac{qR(q)}{KcM_w} \Big|_{\text{plateau}} = \frac{\pi}{L_w} \quad (33)$$

Once L_w and $\langle R_g^2 \rangle_z$ are established, the persistence length l_p can be calculated by means of the equation derived by Benoit, Doty,³⁰ and Oberthür,³¹ which expresses $\langle R_g^2 \rangle_z$ as a function of L_w and l_p for polydisperse semiflexible chains obeying a Schulz-Zimm distribution^{24,32} of the contour length.

$$\langle R_g^2 \rangle_z = \frac{(z+2)L_w l_p}{3(z+1)} - l_p^2 + \frac{2l_p^3}{L_w} - \frac{2l_p^4(z+1)}{L_w^2 z} \left[1 - \left(\frac{(z+1)l_p}{(z+1)l_p + L_w} \right)^z \right] \quad (34)$$

The number-weighted Schulz-Zimm distribution³²

$$N(L, L_w, z) = z \left(\frac{z+1}{L_w} \right)^z L^{z-1} \frac{\exp\left(-\frac{(z+1)L}{L_w}\right)}{\Gamma(z+1)} \quad (35)$$

is defined by its normalized variance $\sigma^2 = 1/(z+1)$ where the polydispersity parameter

$$z = \frac{1}{PD - 1} = \frac{1}{\frac{L_w}{L_n} - 1} \quad (36)$$

is determined by the ratio of the weight-averaged contour length L_w and the number-averaged contour length L_n of the chains. In eq 35, Γ is the Gamma function.

In the second way to determine L_w and l_p , scattering data $R(q)$ were fitted with the scattering function for semiflexible chains given by Pedersen and Schurtenberger²⁸ for two selected cases. Fitting was performed by means of SansView,³³ a tool developed by the DANSE project group for the analysis of scattering data. Within SansView, the “FlexibleCylinderModel” was used, corresponding to “Method 3 with excluded volume effects” developed by Pedersen and Schurtenberger.²⁸ Polydispersity was taken into account by a most-probable Schulz-Zimm³² distribution of the contour length, corresponding to eq 35 with $z = 1$. The fitting function was thus calculated according to

$$R(q, L_w, l_p, z) = KcM_w \frac{\int_0^\infty L^2 N(L, L_w, z) P_{\text{PS}}(q, L, l_p) dL}{\int_0^\infty L^2 N(L, L_w, z) dL} \quad (37)$$

where $P_{\text{PS}}(q, L, l_p)$ is the scattering function of monodisperse wormlike chains.

RESULTS AND DISCUSSION

The present experimental findings on the aggregation of a binary dyestuff mixture will be discussed in terms of kinetics and structural evolution. To this end, we will apply the INE model, the Lomakin model,²¹ and the semiflexible chain model that have been described within the Experimental Section. Each of these models is in line with the longitudinal growth of fiberlike structures. The coaggregation of RD and YD in the presence of Mg^{2+} ions can be considered as a distinct example for such a fiber growth. This view is first and foremost based on

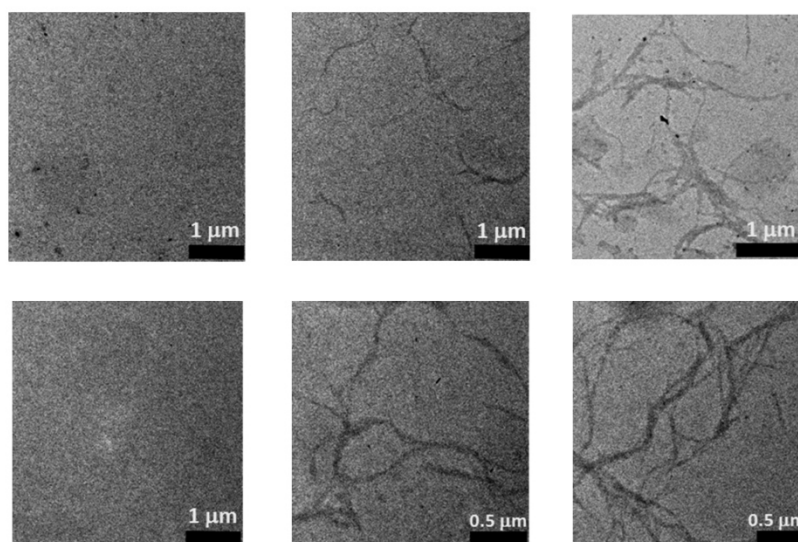


Figure 2. TEM images of dyestuff samples. All samples contain RD and YD in a molar ratio of 1:1. The three columns illustrate the following: sample taken from a solution containing 0.066 g/L dyestuff without magnesium ions (left); sample taken from a solution containing 0.033 g/L dyestuff and 3.25 mM Mg^{2+} three minutes after initiation of the aggregation (middle); sample taken from a solution containing 0.033 g/L dyestuff and 3.25 mM Mg^{2+} ten minutes after initiation of the aggregation (right).

preceding light scattering studies.^{6–8} Further support for a fiberlike shape of the dyestuff aggregates under consideration is provided by the transmission electron micrographs shown in Figure 2. The images have been taken from intermediates of an aggregation process close to those investigated by light scattering experiments. Comparison with images of a reference state in the absence of Mg^{2+} ions clearly confirms the formation of thin, elongated particles induced by the addition of Mg^{2+} ions.

The present work focuses on the results of seven experiments with different metal-to-dye ratios, split into two series. One series varies the concentration of the stoichiometric dyestuff mixture at constant metal concentration and the other one does vice versa. The experiments will be referred to as indicated in Table 1. We will start by discussing the increase of the weight-

Table 1. Symbols Used in Table 2 and Figures 3–8 in Order to Denote the Samples That Were Investigated within the Present Work

[Mg]/mM	1.63	2.44	3.25	5.20
$c_{\text{dye}}/\text{g l}^{-1}$				
0.044		(□)		
0.066	(■)	(◇, ◆)	(●)	(▲)
0.088		(○)		
0.124		(△)		

averaged molar mass of the dyestuff aggregates with time as it has been measured by TR-SLS for all samples. The discussion will focus on the modeling of $M_w(t)$ by the INE model and the Lomakin model,²¹ which have been described in the preceding paragraph.

The INE model in its general form depends on five parameters, comprising the rate constants for nucleation, k_n , and for elongation, k_e , and the three parameters $[B]_{t=0}^{(0)}$, p_0 , and $\text{PD}_{t=0}$, which are the molar concentration, the number-averaged degree of polymerization and the polydispersity of

initial aggregates. These initial aggregates are not generated by the nucleation reaction given by eq 6 but already exist at $t = 0$, thereby the INE model does not present any further information about their origin.

The application of the INE model in its general form based on eq 19 together with eqs 20 and 21 revealed two striking features. First, the fit quality with respect to our experimental data becomes extremely poor by assuming $[B]_{t=0}^{(0)} = 0$. Thus the assumption of initial aggregates characterized by $[B]_{t=0}^{(0)}$, p_0 , and $\text{PD}_{t=0}$ is essential for an adequate modeling of the dyestuff aggregation. Second, when allowing for the presence of initial aggregates, the factor by which the number of aggregates increases due to continuous nucleation at $t > 0$ keeps close to $[B]_{t=0}^{(0)}/[B]_{t=\infty}^{(0)} = 1$ (cf. Supporting Information). This indicates that the INE model takes into account the major part of growing particles by means of the parameter $[B]_{t=0}^{(0)}$. A consequence of these two results is that an ongoing nucleation as suggested by eq 6 without initially existing nuclei obviously fails to describe the dyestuff system under consideration.

We thereupon applied the INE model in terms of eqs 19 and 28 without considering the nucleation reaction given by eq 6 but by solely assuming a constant number of aggregates already existing at $t = 0$. For this case, the model does not depend on k_n anymore. Out of the remaining four parameters, we fixed the values of $\text{PD}_{t=0}$ and p_0 in advance. $\text{PD}_{t=0}$ was estimated by extrapolating the polydispersity obtained from the correlation of R_g and L_w (eq 34) to $t = 0$ at a given persistence length of 200 nm. These extrapolations yielded initial polydispersities of $2 < \text{PD}_{t=0} < 4$ for all of the seven experiments. Variation of the three remaining parameters resulted in least-squares fits that yielded values of $10^3 < p_0 < 10^4$ for the number-averaged degree of polymerization of initial aggregates. This led us to fix p_0 at a value of 3000.

The final fits are based on the variation of the two remaining independent parameters, k_e and $[B]_{t=0}^{(0)}$, and are shown in Figure 3. These fits reproduce satisfactorily the experimental trends. Deviations from the experimental data especially at low

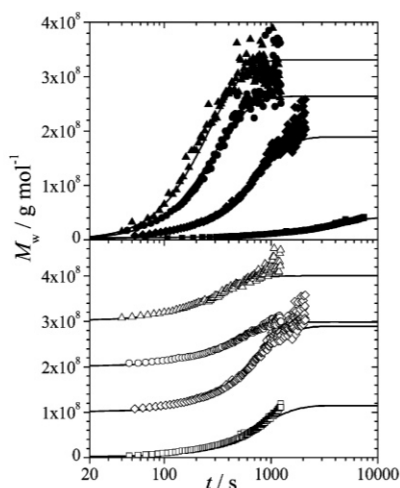


Figure 3. Evolution of the weight-averaged molar mass at variable Mg^{2+} content (top) and at variable dye concentration (bottom). Error bars are not shown for the sake of clarity. The denotations of the symbols are given by Table 1. Because the results obtained for different dye concentrations are similar, the curves with symbols (\diamond), (\circ), and (\triangle) are shifted by 1×10^8 , 2×10^8 , and $3 \times 10^8 \text{ g mol}^{-1}$, respectively, in order to visually set them apart from each other. The continuous lines represent fits with the INE model based on eq 19 in combination with eqs 28 and 29.

molar masses are hardly visible from Figure 3 but are highlighted in the Supporting Information, where a logarithmic scale has been used instead. Nevertheless, the fact that the overall fit quality is acceptable supports the view of a short nucleation phase after which the process is dominated by elongation. Yet, this short nucleation phase had to be inferred from the INE model in an indirect manner by introducing an initial number of aggregates at $t = 0$.

An overview on the fit parameters resulting from an application of the INE model is given in Figure 4. The weight-averaged molar mass at total conversion, $M_{w,t=\infty}$, is determined solely by the constant number concentration of aggregates, $[B]_{t=0}^{(0)}$. The slight changes of $M_{w,t=\infty}$ with increasing dye concentration (cf. Figure 3 bottom) are hence directly reflected by the changes in $[B]_{t=0}^{(0)}$ (cf. Figure 4 bottom). Accordingly, an increase of the Mg^{2+} concentration results in an increase of $M_{w,t=\infty}$ (cf. Figure 3 top) and hence in a decrease of $[B]_{t=0}^{(0)}$ (cf. Figure 4 bottom). The rate constant of elongation, k_e , increases with increasing Mg^{2+} concentration but is independent of the dye concentration (cf. Figure 4 top). This result is a quantification of the trend that is already apparent from Figure 3 and suggests the following features. First, the occurrence of a stable elongation constant k_e throughout the entire concentration regime of dyestuff is a strong indication of the suitability of the applied kinetic model. Second, The dependence of k_e on the Mg^{2+} content points to an involvement of Mg^{2+} in the formation of active “monomers” A and/or of reactive “chain ends” of growing B_i .

Hints on a fast nucleation phase in connection with evidence for the existence of micellar dyestuff aggregates at the very beginning of the self-assembly process as provided by former experiments⁸ led us to also apply the kinetic scheme developed by Lomakin et al.,²¹ which considers both of these aspects. It assumes micelles that are in fast equilibrium with monomers

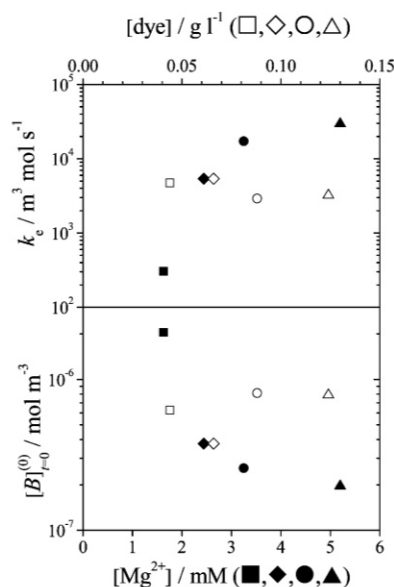


Figure 4. Initial molar concentrations of aggregates and rate constants of elongation for all seven samples as obtained from fitting the INE model to the experimental data. The corresponding fits are illustrated in Figure 3.

and that are capable of forming nuclei. As soon as the micelles are consumed, nucleation is terminated and further conversion solely proceeds via elongation of the existing aggregates by stepwise addition of monomers.

The Lomakin model²¹ in its most general form allocates nine independent fitting parameters (cf. Supporting Information). For the modeling of our kinetic data, we excluded the existence of initial aggregates, setting the parameters $[B]_{t=0}^{(0)}$, and p_0 to zero. Furthermore, the molar mass of a monomer, M_A , was fixed at 1512 g mol^{-1} as indicated above, and the parameter p_M that defines the number of monomers per micelle was set to 500. The latter number is adapted to the magnitude former experiments⁸ have suggested for micellar dyestuff aggregates in the absence of Mg^{2+} . Hence, the Lomakin model²¹ in terms of eq SI-16 (cf. Supporting Information) was fitted to the experimental data by variation of the remaining four parameters, which are the rate constants of nucleation and elongation, k_n and k_e , the critical micelle concentration (cmc) denoted as $[A]^*$, and the number of monomers per nucleus p_n . The resulting fits are shown in Figure 5 and in Figure SI-3 (cf. Supporting Information).

The values of the fitting parameters obtained from the application of the INE model and the Lomakin model²¹ are summarized in Table 2. Before commenting on the actual values, we will discuss the two models with respect to their comparability. Chain elongation for both models takes place at any time and is described by eq 6. Therefore the corresponding rate constants k_e (INE) and k_e (Lomakin) have the same meaning and are directly comparable. The “period of nucleation”, if restricted to $t = 0$ for the INE model, is described by the parameters $[B]_{t=0}^{(0)}$, p_0 , and $\text{PD}_{t=0}$. For the Lomakin model, nucleation proceeds at $0 < t < T$ and is modeled by the four parameters k_n , $[A]^*$, p_n , and p_M . These four parameters can be used to calculate T and $[B]_{t=T}^{(0)}$ given in Table 2. $[B]_{t=T}^{(0)}$ is the total amount of aggregates formed

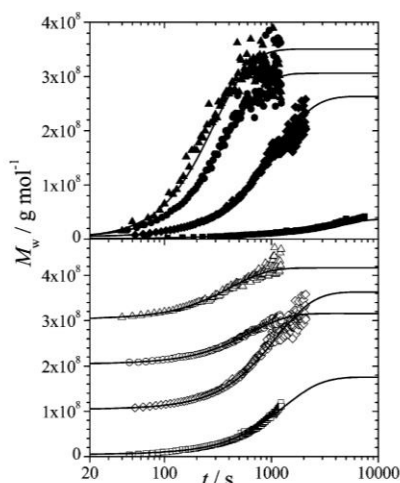


Figure 5. Evolution of the weight-averaged molar mass at variable Mg^{2+} content (top) and at variable dye concentration (bottom). Error bars are not shown for the sake of clarity. The denotations of the symbols are given by Table 1. Since the results obtained for different dye concentrations are similar, the curves with symbols (\diamond), (\circ), and (\triangle) are shifted by 1×10^8 , 2×10^8 , and $3 \times 10^8 \text{ g mol}^{-1}$, respectively, in order to visually set them apart from each other. The continuous lines represent fits with to the Lomakin model²¹ based on eq SI-16 of the Supporting Information neglecting initial aggregates, that is, assuming $[B]_{t=0}^{(0)} = 0$.

throughout the nucleation period in the Lomakin model²¹ and therefore is directly comparable with $[B]_{t=0}^{(0)}$ from the INE model.

In general, the Lomakin model²¹ describes the time period in between 20 and 100 s better than the INE model (cf. Figures SI-2 and SI-3 in the Supporting Information). The total amounts of aggregates formed throughout the process and the rate constants of elongation exhibit similar values and trends for both models and therefore cannot serve as a reason for the improved fit quality of the Lomakin model.²¹ This improvement also cannot be attributed to the fact that the Lomakin model²¹ introduces a finite nucleation period in excess of the INE model since this period is shorter than 10 s for all sets of

parameters obtained (cf. Table 2) and hence is not captured by the light scattering measurements. The slight improvement achieved by the Lomakin model²¹ thus has to be attributed to differences of the degrees of polymerization and of the polydispersities of the particles as they appear directly after the period of nucleation. These quantities were fixed as described above in the case of the INE model but were indirectly varied via the parameters $k_w [A]^*$, and p_n in the case of the Lomakin model.²¹ The comparatively good fit quality of the Lomakin fits is hence a result of the additional degrees of freedom provided by variation of $k_w [A]^*$, and p_n during fitting.

By consistently yielding values of $T < 10 \text{ s}$, the Lomakin model²¹ confirms the existence of a short period of nucleation as already suggested by the INE model. Additionally, the Lomakin model²¹ gives a possible explanation for the origin of the aggregates as it interprets the narrow period of nucleation as follows. Monomers and/or building units equilibrate with micelles transferring a small fraction of the overall amount of dye molecules into micellelike aggregates. In a period of less than 10 s, a burst of nucleation transforms micelles into nuclei. This causes a drop of the concentration $[A]$ below the cmc $[A]^*$ prohibiting further nucleation and restricting monomer consumption to further growth of the existing nuclei from $t = T$ on. In this context, a feature that might appear unrealistic at first glance is the fairly large size of the nuclei. According to the ratios of p_n/p_M given in Table 2, a nucleus would contain at least 10 times more building units than a micelle. This can be explained as follows. The addition of Mg^{2+} causes an instant jump of the scattered intensity.⁸ The Lomakin model²¹ can capture this high initial scattering intensity by adopting a high molar mass of either the micelles or the nuclei. The degree of polymerization of the micelles was fixed to $p_M = 500$ corresponding to the value found in stoichiometrically mixed solutions of RD and YD prior to the addition of Mg^{2+} ions.⁸ Hence, an assumption of large nuclei is compulsory for the modeling of the high initial scattering. However, the structure of the micelles as well as the cmc may be considerably affected by the addition of Mg^{2+} . Therefore, the values of p_n/p_M and $[A]^*$ given in Table 2 should be regarded as fitting parameters with qualitative meaning only. Nevertheless, our application of the Lomakin model²¹ remains physically meaningful in that it suggests a mechanism capable of modeling a short period of

Table 2. Model Parameters Obtained from Fitting the INE Model in Terms of Equations 19, 28, and 32 and the Lomakin Model²¹ in Terms of Equation SI-16 (cf. Supporting Information) to the Experimental Data^a

model	INE	INE	Lom. ²¹	Lom.	Lom.	Lom.	Lom.	Lom.
parameter	k_e	$[B]_{t=0}^{(0)}$	k_e	$[B]_{t=T}^{(0)}$	T	k_n	$[A]^*$	p_n/p_M
	$[\text{m}^3/(\text{mol}\cdot\text{s})]$	$[\text{mM}]$	$[\text{m}^3/(\text{mol}\cdot\text{s})]$	$[\text{mM}]$	$[\text{s}]$	$[\text{s}^{-1}]$	$[\text{mM}]$	$[-]$
$[\text{Mg}^{2+}] / \text{mM}$								
1.63 (\blacksquare)	3.1×10^{02}	2.0×10^{-06}	2.0×10^{02}	1.4×10^{-06}	3.7	8.5×10^{-03}	3.0×10^{-02}	10
2.44 (\blacklozenge)	5.4×10^{03}	3.8×10^{-07}	5.1×10^{03}	2.8×10^{-07}	1.2	8.8×10^{-03}	3.8×10^{-02}	22
3.25 (\bullet)	1.7×10^{04}	2.6×10^{-07}	1.7×10^{04}	2.2×10^{-07}	2.2	1.3×10^{-01}	3.9×10^{-02}	21
5.20 (\blacktriangle)	3.0×10^{04}	2.0×10^{-07}	2.6×10^{04}	1.9×10^{-07}	1.3	9.9×10^{-01}	4.1×10^{-02}	15
$c_{\text{dye}} / \text{g l}^{-1}$								
0.044 (\square)	4.7×10^{03}	4.3×10^{-07}	4.3×10^{03}	2.5×10^{-07}	1.5	8.8×10^{-03}	2.5×10^{-02}	18
0.066 (\diamond)	5.4×10^{03}	3.8×10^{-07}	5.1×10^{03}	2.8×10^{-07}	1.2	8.8×10^{-03}	3.8×10^{-02}	22
0.088 (\circ)	2.9×10^{03}	8.1×10^{-07}	2.9×10^{03}	7.6×10^{-07}	9.3	9.1×10^{-02}	4.6×10^{-02}	15
0.124 (\triangle)	3.2×10^{03}	1.1×10^{-06}	3.2×10^{03}	1.1×10^{-06}	3.6	1.3×10^{-01}	6.8×10^{-02}	12

^aIt is k_e the rate constant of elongation for both models, $[B]^{(0)}$ the number of aggregates existing at the time when nucleation is terminated (which is $t = 0$ for the INE model and $t = T$ for the Lomakin model), k_w and $[A]^*$ the rate constant of nucleation and the cmc for the Lomakin model²¹ and p_n/p_M the ratio of the degree of polymerization of a nucleus and a micelle for the Lomakin model.²¹

nucleation. Hereby, we would like to draw attention to the analogy of the Lomakin model²¹ with the model of nucleation from supersaturated solutions developed by Dinegar and LaMer.³⁴ According to the latter, the critical concentration beyond which nucleation sets in takes the role of the critical micelle concentration. In both the Lomakin²¹ and the Dinegar-LaMer model,³⁴ nuclei begin to form in supersaturated solution only if the concentration of solute has reached a critical value well above its solubility. After reaching this critical value, nuclei are formed until the solute concentration has dropped below this critical limit. From that point on, nucleation is terminated and further attachment of dissolved species to the existing nuclei takes place. In a system where nuclei form from micelles, the latter are intermediates only. Therefore, such a system is not distinguishable from the Dinegar-LaMer model³⁴ with respect to its kinetic modeling.

In summary, three main aspects have been settled on the basis of our discussion: (i) $M_w(t)$ can be conveniently parametrized using either the INE model or the Lomakin model.²¹ Out of the two models, the latter exhibits the advantage to provide a physically plausible explanation for the short period of nucleation. (ii) Increase of the Mg^{2+} content enhances the activity of monomeric and/or of growing species and at the same time leads to a decrease in the number concentration of the growing species. (iii) The nucleation phase is terminated within the first second(s) after initiation of the reaction.

After having established an interpretation of the TR-SLS data with suitable kinetic models, we will now analyze the same data with respect to structural features of the growing aggregates. The correlation between the z -averaged radius of gyration, R_g , and the weight-averaged molar mass of the aggregates, $M_{w,ag}$, may give valuable hints on the nature of colloidal particles. By attempting to establish such a correlation for the dye aggregates, we faced the complication that $M_{w,ag}$ is not directly accessible by light scattering. The quantity M_w shown in Figure 3 is an average over the whole ensemble of scatterers and hence includes also unbound monomers. The same also holds for $\langle R_g^2 \rangle_z$, however, the z -average favors the aggregates so strongly that the contribution of unbound monomers to R_g is negligible.³⁵ Thus, two possible routes will be discussed within the present work in order to obtain $M_{w,ag}$ which refers exclusively to aggregates.

The first route by which the molar mass of the growing aggregates may be separated from the weight-averaged mass of the entire ensemble of particles shall be based on the kinetic fits which have been performed using the INE model. Once the kinetic parameters are established, the quantity $M_{w,ag}$ that refers solely to the aggregates can be calculated as

$$M_{w,ag}(t) = \frac{M_A[B]^{(2)}(t)}{[B]^{(1)}(t)} \quad (38)$$

Together with the access to $M_{w,ag}(t)$, the kinetic fits yield corresponding polydispersities $PD(t)$ in terms of eq 26. These polydispersities are of relevance in the next step, where $R_g(t)$ shall be fitted as a function of $M_{w,ag}(t)$ by means of eq 34, since eq 34 also includes the polydispersity of the aggregates in terms of the coupling parameter z . In order to consistently rely on the results of the kinetic study, polydispersity was adopted as received from the INE model fits of the mass data according to

$$z(t) = \frac{[B]^{(1)}(t)[B]^{(1)}(t)}{[B]^{(0)}(t)[B]^{(2)}(t) - [B]^{(1)}(t)[B]^{(1)}(t)} \quad (39)$$

for successive fits of $R_g(t)$ versus $M_{w,ag}(t)$ with eq 34. Equation 39 evolves from combining eq 26 and eq 36. The resulting fits are shown in Figure 6. Since the coupling parameter $z(t)$ was

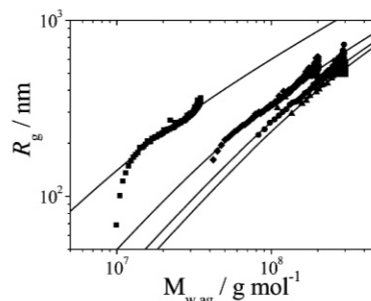


Figure 6. Correlation of the radius of gyration and the weight-averaged molar mass of the aggregates. $M_{w,ag}$ has been calculated using eq 38. The symbols correspond to four different Mg^{2+} concentrations at a constant dye concentration (cf. Table 1). Lines represent fits based on eq 34 revealing a persistence length l_p and a linear mass density $M_L = M_{w,ag}/L_w$ for each curve, given a polydispersity that obeys eq 39.

obtained by means of eq 39, only the persistence length l_p and the mass per unit length M_L (where L_w in eq 34 = $M_{w,ag}/M_L$) served as fitting parameters and are available in the Supporting Information. The agreement between the fits and the experimental data is acceptable and the resulting persistence lengths are close to 200 nm and thus in line with the ones that evolve from the second route described below. Hence, the approach supports the combination of the wormlike chain model with the INE model in order to describe the dye aggregation under consideration.

The second route was already pursued in our earlier works^{6,7,11} and consists in the evaluation of the weight-averaged contour length L_w by means of eq 33. The resulting values of L_w like R_g remain unaffected by the unbound monomers because the effect of the total concentration including monomers and aggregates cancels in the product $c \cdot M_w$. The weight-averaged contour length, L_w , thus is directly proportional to $M_{w,ag}$ assuming a constant mass per unit length M_L such that $L_w = M_{w,ag}/M_L$. The correlation of R_g and L_w is exemplified in Figure 7. For all samples, the trends could be described qualitatively with the predictions for wormlike chains given by eq 34 using persistence lengths close to $l_p = 200$ nm and polydispersities of $PD \approx 2$ corresponding to $z = 1$. However, a closer look at the data shows that the trends do not strictly obey eq 34 under the assumption of constant l_p and z , but are slightly less steep.

An explanation of the slight deviations of the data from the trend predicted by eq 34 may be achieved by one or a combination of the following two features. (i) The set of data (l_p , R_g , L_w) can be calculated with eq 34 at constant z releasing the constraint of a constant persistence length (cf. Figure 8B). Yet, a decrease of the persistence length over the time (i.e., with increasing L_w) points to a decrease of the chain stiffness of linear wormlike chains and thus is difficult to be explained with a physically realistic reasoning. One attempt in this direction has been outlined in former works: A gradual onset of chain branching would lead to an apparent decrease of l_p if evaluated

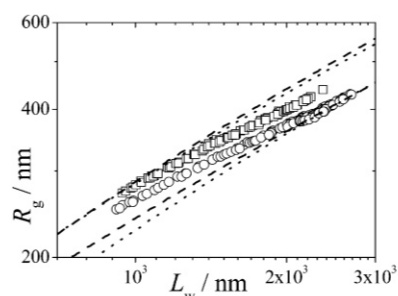


Figure 7. Correlations of the averaged radius of gyration $R_g = (\langle R_g^2 \rangle)^{1/2}$ determined by means of eq 5 and the weight-averaged contour length L_w , determined by eq 33 for two samples. Correlations for other samples look similar and are not shown for the sake of clarity. The dashed lines represent model curves with $l_p = 150$ nm and $l_p = 240$ nm for $z = 1$. The dotted lines represent model curves with $z = 0.5$ and $z = 3$ for $l_p = 200$ nm. The model curves were calculated using eq 34.

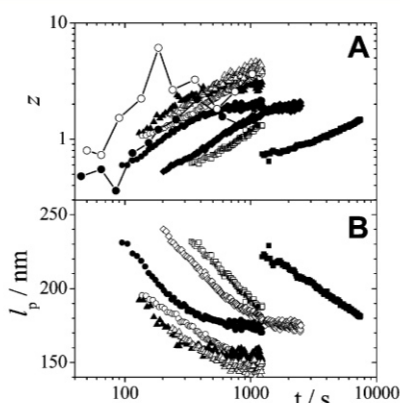


Figure 8. Time evolution of the polydispersity parameter z assuming a constant persistence length of 200 nm (A) and of the persistence length l_p assuming a constant $z = 1$ (B) for all samples. The values have been calculated by means of eq 34. The denotations of the symbols are given in Table 1. Interconnected points in panel A illustrate the results obtained from form factor fits (cf. Figure 9) with eq 37 by assuming a constant persistence length of 200 nm.

in terms of linear wormlike chains.⁷ (ii) The set of data (z , R_g , L_w) can be calculated with eq 34 at constant l_p releasing the constraint of a constant polydispersity. As demonstrated in Figure 8A, the resulting polydispersities ($PD = 1 + z^{-1}$) decrease significantly during the process if l_p is kept constant. This route of interpretation implies that the initial phase of the process is dominated by a short period of nucleation yielding chains with a certain size distribution. After termination of the nucleation phase, the relative broadness of the particle size distribution would steadily decrease by the proceeding incorporation of monomers.

Out of the two discussed features, that is, the effects of chain branching and of a short period of nucleation, the latter is probably of major relevance for the system under consideration since the trends in z which are extracted with eq 34 and which base on structural features (cf. Figure 8A) are in full agreement with the trends received from the kinetic study using eq 39. Both the kinetic and the structural approach suggest an increase of z with time and therefore a decrease of polydispersity.

Finally, representative scattering curves of two samples are shown in Figure 9 along with the corresponding model fits²⁸

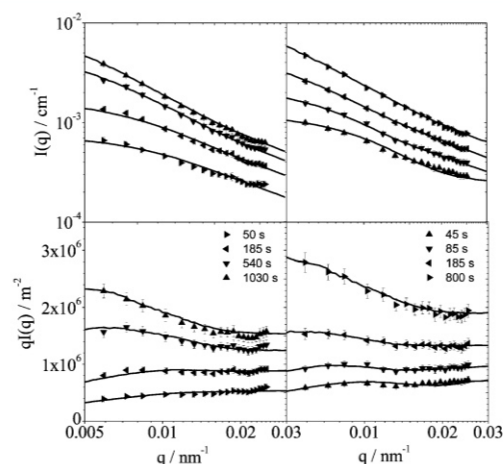


Figure 9. Scattering curves of a sample containing 0.066 g/L dye and 3.25 mM Mg^{2+} (left-hand column) and a sample containing 0.088 g/L dye and 2.44 mM Mg (right-hand column). Different times after initiation of the reaction are indicated within the graphs. The curves are represented logarithmically (upper row) and as bended-rod-plots²⁹ (lower row). Lines correspond to fits by means of eq 37. For the fits, the persistence length was kept constant ($l_p = 200$ nm), whereas L_w , z , and the forward scattering served as variable fitting parameters.

based on eq 37 assuming a constant persistence length of $l_p = 200$ nm. The fits describe the experimental curves in an acceptable way and yield similar trends of z (cf. Figure 8A) and L_w (not shown) as achieved by the use of eq 34.

■ SUMMARY

Upon adding aqueous Mg^{2+} solutions to aqueous solutions of mixtures of RD and YD, the dyestuffs self-assemble into fibers. The growing fibers adopt a distinct stoichiometry of RD/YD = 1:1.⁸ The growth process was analyzed by means of time-resolved static light scattering at variable Mg^{2+} content and at variable dyestuff concentration, where the composition of the dyestuff mixture prior to the addition of Mg^{2+} was kept at the stoichiometric point. Successively, two kinetic growth models, the INE model and the Lomakin model,²¹ have been applied to describe the evolution of aggregate mass values with time. To this end, explicit formulas were derived for the calculation of weight-averaged molar mass data. The application of the INE model suggests a short period of nucleation for the dyestuff aggregation and permits to quantify a distinct dependence of the aggregation rate on the Mg^{2+} concentration. Both of these features are confirmed by the application of the Lomakin model.²¹ Unlike the INE model, the Lomakin model²¹ gives an explanation for the origin of nuclei by generating them from micelles. This is plausible since micellar aggregates are present in solutions of RD and YD even when Mg^{2+} is absent.⁸

TEM images, the analysis of scattering patterns and the correlation of size parameters suggest a wormlike shape of the growing dyestuff aggregates. Thereby, a constant persistence length of about 200 nm could be established accompanied with a decrease of polydispersity toward increasing contour length of the dyestuff aggregates. The assumption of a polydispersity that decreases as chains grow longer is in full agreement with a short

period of nucleation as identified by the kinetic study. The width of the initial distribution of aggregate masses is caused by the finite period of nucleation and inevitably gets narrower as soon as solely chain elongation proceeds. A constant persistence length, corresponding to a constant stiffness of the chains, further supports the idea of a purely longitudinal fiber growth since a lateral growth would most likely cause a chain stiffening.

■ ASSOCIATED CONTENT

■ Supporting Information

Outline of kinetic equations for the Lomakin model; $[B]_{t=\infty}^{(0)}/[B]_{t=0}^{(0)}$ for fits with the INE model; representation of $M_w(t)$ in logarithmic scale fitted with the INE model and with the Lomakin model; resulting parameters for fits of R_g versus $M_{w,app}$. This material is available free of charge via the Internet at <http://pubs.acs.org>.

■ AUTHOR INFORMATION

Corresponding Author

*E-mail: klaus.huber@upb.de. Phone: +49 5251 602125.

Notes

The authors declare no competing financial interest.

■ REFERENCES

- Haller, R. Beiträge zur Kenntnis der Adsorptionsverbindungen. *Kolloid-Z.* **1918**, *22*, 113–133.
- Edwards, D. E.; Ormerod, A.; Tidley, G. J. T.; Jabar, A. A.; Mahendrasingham, A. In *Physico-Chemical Principles of Color Chemistry*; Springer: New York, 2011.
- Advances in Color Chemistry Series*; Peters, A. T., Freeman, H. S., Eds.; Blackie Academic&Professional: London, 1996; Vol. 4; p 83.
- Alberts, B.; Bray, D.; Lewis, J.; Raff, M.; Roberts, K.; Watson, J. D. *The Molecular Biology of the Cell*, 3rd ed.; Garland Publishers: New York, 1994.
- Selkoe, D. J. Cell Biology of the Amyloid Beta-Protein Precursor and the Mechanism of Alzheimer's Disease. *Annu. Rev. Cell Biol.* **1994**, *10*, 373–403.
- Escudero Inglés, S.; Katzenstein, A.; Schlenker, W.; Huber, K. Time-Resolved Recording of Ionic Dye-stuff Aggregation by Static Light Scattering. *Langmuir* **2000**, *16*, 3010–3018.
- Katzenstein, A.; Huber, K. Model of Polydisperse Wormlike Stars and its Application to Dye-stuff Aggregates. *Langmuir* **2002**, *18*, 7049–7056.
- Michels, R.; Sinemus, T.; Hofmann, J.; Brutschy, B.; Huber, K. Co-Aggregation of Two Anionic Azo-Dye-stuffs at a Well-Defined Stoichiometry. *J. Phys. Chem. B* **2013**, *117*, 8611–8619.
- Becker, A.; Schmidt, M. Time-Resolved Static Light Scattering: New Possibilities in Polymer Characterization. *Macromol. Chem. Macromol. Symp.* **1991**, *50*, 249–260.
- Bernocco, S.; Ferri, F.; Profumo, A.; Cuniberti, C.; Rocco, M. Polymerization of Rod-Like Macromolecular Monomers Studied by Stopped-Flow, Multiangle Light Scattering: Set-Up, Data Processing, and Application to Fibrin Formation. *Biophys. J.* **2000**, *79*, 561–583.
- Witte, T.; Haller, L. A.; Luttmann, E.; Krüger, J.; Fels, G.; Huber, K. Time Resolved Structure Analysis of Growing β -Amyloid Fibers. *J. Struct. Biol.* **2007**, *159*, 71–81.
- Denkinger, P.; Burchard, W. Determination of Chain Stiffness and Polydispersity from Static Light Scattering. *J. Polym. Sci.* **1991**, *B 29*, 589–600.
- Müller, M.; Burchard, W. Fibrinogen-Fibrin Transformations Characterized during the Course of Reaction by their Intermediate Structures. A light scattering Study in Dilute Solution under Physiological Conditions. *Biochim. Biophys. Acta* **1978**, *537*, 208–225.
- Lomakin, A.; Chung, D. S.; Benedek, G. B.; Kirschner, D. A.; Teplow, D. B. On the Nucleation and Growth of Amyloid Beta Protein Fibrils: Detection of Nuclei and Quantification of Rate Constants. *Proc. Natl. Acad. Sci. U.S.A.* **1996**, *93*, 1125–1129.
- Pallitto, M. M.; Murphy, R. M. A Mathematical Model of the Kinetics of β -Amyloid Fibril Growth from the Denatured State. *Biophys. J.* **2001**, *81*, 1805–1822.
- Morris, A. M.; Watzky, M. A.; Finke, R. G. Protein Aggregation Kinetics, Mechanism, and Curve-Fitting: A Review of the Literature. *Biochim. Biophys. Acta* **2009**, *1794*, 375–397.
- Watzky, M. A.; Finke, R. G. Transition Metal Nanocluster Formation Kinetic and Mechanistic Studies. A New Mechanism When Hydrogen is the Reductant: Slow, Continuous Nucleation and Fast Autocatalytic Surface Growth. *J. Am. Chem. Soc.* **1997**, *119*, 10382–10400.
- Morris, A. M.; Watzky, M. A.; Agar, J. N.; Finke, R. G. Fitting Neurological Protein Aggregation Kinetic Data via a 2-Step, Minimal/“Ockham's Razor” Model: The Finke-Watzky Mechanism of Nucleation Followed by Autocatalytic Surface Growth. *Biochemistry* **2008**, *47*, 2413–2427.
- Wegner, A.; Savko, P. Fragmentation of Actin Filaments. *Biochemistry* **1982**, *21*, 1909–1913.
- Casassa, E. F. Light Scattering from Very Long Rod-Like Particles and an Application to Polymerized Fibrinogen. *J. Phys. Chem.* **1955**, *23*, 596–597.
- Lomakin, A.; Teplow, D. B.; Kirschner, D. A.; Benedek, G. B. Kinetic Theory of Fibrillogenesis of Amyloid Beta Protein. *Proc. Natl. Acad. Sci. U.S.A.* **1997**, *94*, 7942–7947.
- Roberts, J. R. Kinetics of Irreversible Protein Aggregation: Analysis of Extended Lumry-Eyring Models and Implications for Predicting Protein Shelf Life. *J. Phys. Chem. B* **2003**, *107*, 1194–1207.
- Zimm, B. The Scattering of Light and the Radial Distribution Function of High Polymer Solutions. *J. Chem. Phys.* **1948**, *16*, 1093–1099.
- Zimm, B. Apparatus and Methods for Measurement and Interpretation of the Angular Variation of Light Scattering; Preliminary Results on Polystyrene Solutions. *J. Chem. Phys.* **1948**, *16*, 1099–1116.
- Lages, S.; Michels, R.; Huber, K. Coil-Collapse and Coil-Aggregation due to the Interaction of Cu^{2+} and Ca^{2+} Ions with Anionic Polyacrylate Chains in Dilute Solution. *Macromolecules* **2010**, *43*, 3027–3035.
- Imae, T.; Gagel, L.; Tunich, C.; Platz, G.; Iwamoto, T.; Funayama, K. Formation of Supramolecular Fibril by Water-Soluble Azo Dye. *Langmuir* **1998**, *14*, 2197–2200.
- Kratky, O.; Porod, G. Röntgenuntersuchung gelöster Fadenmoleküle. *Recl. Trav. Chim.* **1949**, *68*, 1106–1123.
- Pedersen, J. S.; Schurtenberger, P. Scattering Functions of Semiflexible Polymers with and without Excluded Volume Effects. *Macromolecules* **1996**, *29*, 7602–7612.
- Holtzer, A. Interpretation of the Angular Distribution of the Light Scattered by a Polydisperse System of Rods. *J. Polym. Sci.* **1955**, *17*, 432–434.
- Benoit, H.; Doty, P. Light Scattering from Non-Gaussian Chains. *J. Phys. Chem.* **1953**, *57*, 958–963.
- Oberthür, R. C. Radius of Gyration versus Molar Mass Relations from Light Scattering for Polydisperse Non-Gaussian Chain Molecules. Polystyrene in Toluene and Short DNA-Fragments in Aqueous NaCl-Solution. *Makromol. Chem.* **1978**, *179*, 2693–2706.
- Schulz, G. V. Über die Kinetik der Kettenreaktionen. V. Der Einfluss verschiedener Reaktionsarten auf die Polymolekularität. *Z. Phys. Chem.* **1939**, *B43*, 25–46.
- Alina, G.; Cortes Hernandez, R.; Butler, P.; Doucet, M.; Jackson, A.; Kienzle, P.; Kline, S.; Zhou, J. The SansView software; DANSE.
- LaMer, V. K.; Dinegar, R. H. Theory, Production, and Mechanism of Formation of Monodispersed Hydrosols. *J. Am. Chem. Soc.* **1950**, *72*, 4847–4854.
- Liu, J.; Rieger, J.; Huber, K. Analysis of the Nucleation and Growth of Amorphous CaCO_3 by Means of Time-Resolved Static Light Scattering. *Langmuir* **2008**, *24*, 8262–8271.

Kinetic and Structural Features of a Dye-stuff Co-Aggregation Studied by Time-Resolved Static Light Scattering

Rolf Michels,[†] Yvonne Hertle,[§] Thomas Hellweg,[§] and Klaus Huber*^{·†}

[†]Universität Paderborn, Department für Physikalische Chemie, Warburger Straße 100, D-33098 Paderborn, Germany

[§]Universität Bielefeld, Physikalische und Biophysikalische Chemie, Universitätsstraße 25, D-33615 Bielefeld, Germany

*to whom correspondence should be addressed

E-mail: klaus.huber@upb.de

Phone: +49 5251 602125

Supporting Information

SUPPORTING INFORMATION. Outline of kinetic equations for the Lomakin model; $[B]_{t=\infty}^{(0)}/[B]_{t=0}^{(0)}$ for fits with the INE model; representation of $M_w(t)$ in logarithmic scale fitted with the INE model and with the Lomakin model; resulting parameters for fits of R_g vs. $M_{w,app}$. This material is available free of charge via the Internet at <http://pubs.acs.org>.

Outline of Kinetic Equations in Order to Calculate $M_w(t)$ for the Lomakin Model¹

The fundamental reaction steps of the Lomakin model are summarized in Figure 1 of Reference 1. Within the time regime $0 \leq t < T$, micelles M consisting of p_M monomers are present and in fast equilibrium with free monomers, and the monomer concentration constantly remains at the critical micelle concentration $[A]^*$. The micelles are capable of generating nuclei (k_n = rate constant of nucleation) that consist of p_n monomers. In addition to these nuclei, monodisperse “seeds” that consist of p_0 monomers, respectively, may be present already at $t = 0$. According to our denotation, these seeds would correspond to the “number of nuclei at $t = 0$ ”, $[B]_{t=0}^{(0)}$, with $[B]_{t=0}^{(1)} = p_0[B]_{t=0}^{(0)}$ and $[B]_{t=0}^{(2)} = p_0^2 PD_{t=0}[B]_{t=0}^{(0)}$ (cf. eq(27) in the main article). The seeds as well as the generated nuclei grow by successive addition of “monomers” A (rate constant of elongation k_e). At $t \geq T$, the micelles are entirely consumed (number concentration of micelles $[M] = 0$). This terminates nucleation and the concentration of free monomers from $t = T$ on decreases solely due to chain elongation.

In order to derive the 2nd moment of the ensemble of aggregates according to the kinetic model introduced by Lomakin et al, we start from eq(5) of Ref 1. In our denotation, it writes as

$$\frac{d[B]^{(k)}}{dt} = k_n p_n^k [M] + k_e [A] \sum_{j=0}^{k-1} \binom{k}{j} [B]^{(j)}, \quad (\text{SI-1})$$

where

$$[B]^{(k)} = \sum_i i^k [B_i] \quad (\text{SI-2})$$

is the k^{th} moment of the ensemble of growing particles. We first consider the regime $0 \leq t < T$. Here, the monomer concentration remains constant at $[A] = [A]^*$. According to eq(SI-1), the changes of the 0th and the 1st moment of the ensemble of growing particles are given by

$$\frac{d[B]^{(0)}}{dt} = k_n [M](t), \quad (\text{SI-3})$$

$$\frac{d[B]^{(1)}}{dt} = k_n p_n [M](t) + [A]^* k_e [B]^{(0)}(t). \quad (\text{SI-4})$$

The overall concentration of monomers is

$$[A]_{\text{tot}} = [A]^* + p_M [M](t) + [B]^{(1)}(t). \quad (\text{SI-5})$$

From eq(SI-3), eq(SI-4) and eq(SI-5), $[B]^{(1)}$ and $[M]^{(0)}$ as well as their derivatives can be eliminated in favor of $[B]^{(0)}$.

$$\frac{d^2[B]^{(0)}}{dt^2} + \frac{k_n p_n}{p_M} \frac{d[B]^{(0)}}{dt} + \frac{k_n k_e [A]^*}{p_M} [B]^{(0)} = 0 \quad (\text{SI-6})$$

Lomakin et al. gave the solution for $[B]^{(0)}$ neglecting the first derivative with time. A general solution of eq(SI-6) including also the first derivative term may be written as

$$[B]^{(0)}(t) = c_6 \exp(c_7 t) + c_8 \exp(c_9 t) \quad (\text{SI-7})$$

with

$$c_6 = [B]_{t=0}^{(0)} - c_8 = \frac{k_n([A]_{\text{tot}} - [A]^* - p_0[B]_{t=0}^{(0)}) - c_9 p_M [B]_{t=0}^{(0)}}{p_M(c_7 - c_9)} ,$$

$$c_7 = -\frac{p_n k_n - \sqrt{p_n^2 k_n^2 - 4k_n k_e p_M [A]^*}}{2p_M} ,$$

$$c_9 = -\frac{p_n k_n + \sqrt{p_n^2 k_n^2 - 4k_n k_e p_M [A]^*}}{2p_M} .$$

Reinserting the solution for $[B]^{(0)}$ into eq(SI-3) and eq(SI-5) enables the calculation of $[B]^{(1)}$ and $[M]$.

$$[B]^{(1)}(t) = [A]_{\text{tot}} - [A]^* - \frac{p_M}{k_n} (c_6 c_7 \exp(c_7 t) + c_8 c_9 \exp(c_9 t)) \quad (\text{SI-8})$$

$$[M](t) = ([A]_{\text{tot}} - [A]^* - [B]^{(1)}(t)) / p_M \quad (\text{SI-9})$$

The change of the 2nd moment is

$$\frac{d[B]^{(2)}}{dt} = k_n p_n^2 [M](t) + [A]^* k_e ([B]^{(0)}(t) + 2[B]^{(1)}(t)) .$$

The solution thereof can be written as

$$[B]^{(2)}(t) = p_0^2 [B]_{t=0}^{(0)} P D_{t=0} + \int_0^t \{k_n p_n^2 [M](x) + k_e [A]^* ([B]^{(0)}(x) + 2[B]^{(1)}(x))\} dx. \quad (\text{SI-10})$$

$$B^{(2)}(t) = p_0^2 [B]_{t=0}^{(0)} P D_{t=0} + c_{10} t + c_6 (\exp(c_7 t) - 1) \left(c_{11} + \frac{k_e [A]^*}{c_7} \right) + c_8 (\exp(c_9 t) - 1) \left(c_{11} + \frac{k_e [A]^*}{c_9} \right) \quad (\text{SI-11})$$

with

$$c_{10} = 2k_e [A]^* ([A]_{\text{tot}} - [A]^*) ,$$

$$c_{11} = p_n^2 - \frac{2k_e [A]^* p_M}{k_n} .$$

The time T by which all micelles are consumed can be determined with eq(SI-9) by considering $[M](t=T) = 0$

$$T = \frac{\ln\left(-\frac{c_6 c_7}{c_8 c_9}\right)}{c_9 - c_7} . \quad (\text{SI-12})$$

For $t \geq T$, nucleation is terminated since there are no more micelles. In this regime, the monomer concentration $[A](t) = [A]_{\text{tot}} - B^{(1)}(t)$. The first three moments evolve as

$$B^{(0)}(t \geq T) = [B]_{t=T}^{(0)} , \quad (\text{SI-13})$$

$$B^{(1)}(t \geq T) = [A]_{\text{tot}} + ([B]_{t=T}^{(1)} - [A]_{\text{tot}}) \exp(k_e [B]_{t=T}^{(0)} (T - t)) , \quad (\text{SI-14})$$

$$B^{(2)}(t \geq T) = c_{12} + c_{13} \exp(k_e[B]_{t=T}^{(0)}(T-t)) + c_{14} \exp(2k_e[B]_{t=T}^{(0)}(T-t)) \quad (\text{SI-15})$$

with

$$\begin{aligned} c_{12} &= [B]_{t=T}^{(2)} + \frac{[A]_{\text{tot}} - [B]_{t=T}^{(1)}}{[B]_{t=T}^{(0)}} \left([A]_{\text{tot}} + [B]_{t=T}^{(0)} + [B]_{t=T}^{(1)} \right) , \\ c_{13} &= \frac{[B]_{t=T}^{(1)} - [A]_{\text{tot}}}{[B]_{t=T}^{(0)}} \left(2[A]_{\text{tot}} + [B]_{t=T}^{(0)} \right) , \\ c_{14} &= \frac{\left([A]_{\text{tot}} - [B]_{t=T}^{(1)} \right)^2}{[B]_{t=T}^{(0)}} , \end{aligned}$$

where $[B]_{t=T}^{(0)}$, $[B]_{t=T}^{(1)}$ and $[B]_{t=T}^{(2)}$ can be calculated by setting $t = T$ in eq(SI-7), eq(SI-8) and eq(SI-11), respectively. The weight-averaged molar mass of the whole ensemble, including monomers, micelles and growing aggregates, can then be calculated as

$$M_w(t) = \begin{cases} \frac{M_A}{[A]_{\text{tot}}} ([A]^* + p_M^2 [M](t) + [B]^{(2)}(t)) & \text{for } 0 \leq t < T \\ \frac{M_A}{[A]_{\text{tot}}} ([A](t) + [B]^{(2)}(t)) & \text{for } T \leq t \end{cases} . \quad (\text{SI-16})$$

The Lomakin model can be applied to the results obtained from static light scattering in terms of eq(SI-16). In its most general form, the model allocates 9 independent fitting parameters provided that $[A]_{\text{tot}}$ is known:

p_0	number-averaged degree of polymerization of initial aggregates (“seeds”)
p_M	number of monomers within a micelle
p_n	number of monomers within a nucleus
k_n	rate constant of nucleation (first order)
k_e	rate constant of chain elongation (second order)
$[A]^*$	critical micelle concentration
M_A	molar mass of a monomeric unit
$PD_{t=0}$	polydispersity of the initial aggregates
$B_{t=0}^{(0)}$	number concentration of initial aggregates

Table SI-1. Symbols denoting the samples that were investigated within the present work. The symbols of the experiments used within the Supporting Information are the same as in the main article.

$c_{\text{dye}} / \text{g l}^{-1}$	$[\text{Mg}] / \text{mM}$			
	1.63	2.44	3.25	5.20
0.044		(□)		
0.066	(■)	(◇, ◆)	(●)	(▲)
0.088		(○)		
0.124		(△)		

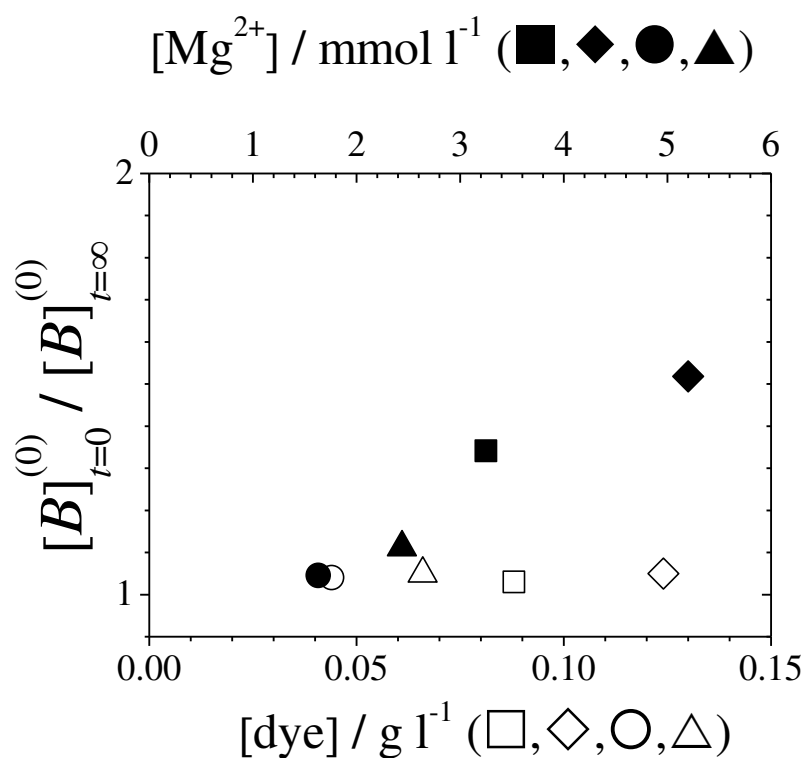


Figure SI-1. Factor by which the number concentration of aggregates represented by $[B]_{t=0}^{(0)}$ increases for the INE model due to nucleation at $t > 0$ if both nucleation at $t > 0$ according to eq(6) in the main article and initial aggregates are enabled, corresponding to eq(20) and (23) together with eq(19) from the main article. The factors hardly differ from unity, indicating that the major part of the nuclei form right in the beginning of the aggregation process. This suggests the application of the INE model without considering continuous nucleation, corresponding to eq(28) and eq(29) together with eq(19) from the main article.

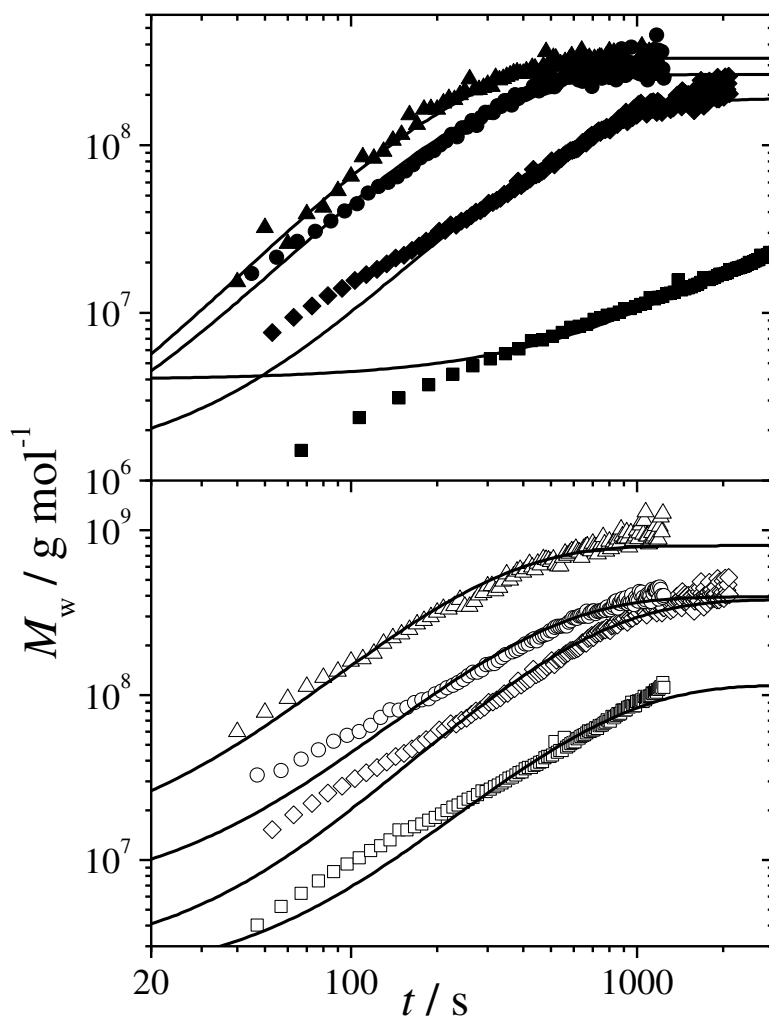


Figure SI-2. Evolution of the weight-averaged molar mass at variable Mg^{2+} content (top) and at variable dye concentration (bottom). Error bars are not shown for the sake of clarity. The denotations of the symbols are given by Table SI-1. Since the results obtained for different dye concentrations lie close to each other, the curves with symbols (\diamond), (\circ) and (\triangle) are shifted by factors of 2, 4 and 8, respectively, in order to visually set them apart from each other. The continuous lines represent fits with to the INE model based on eq(19) in combination with eq(28) and eq(29), which restricts nucleation to time $t = 0$. The logarithmic scale of the ordinate highlights the deviations of the fits from the experimental data at low molar masses.

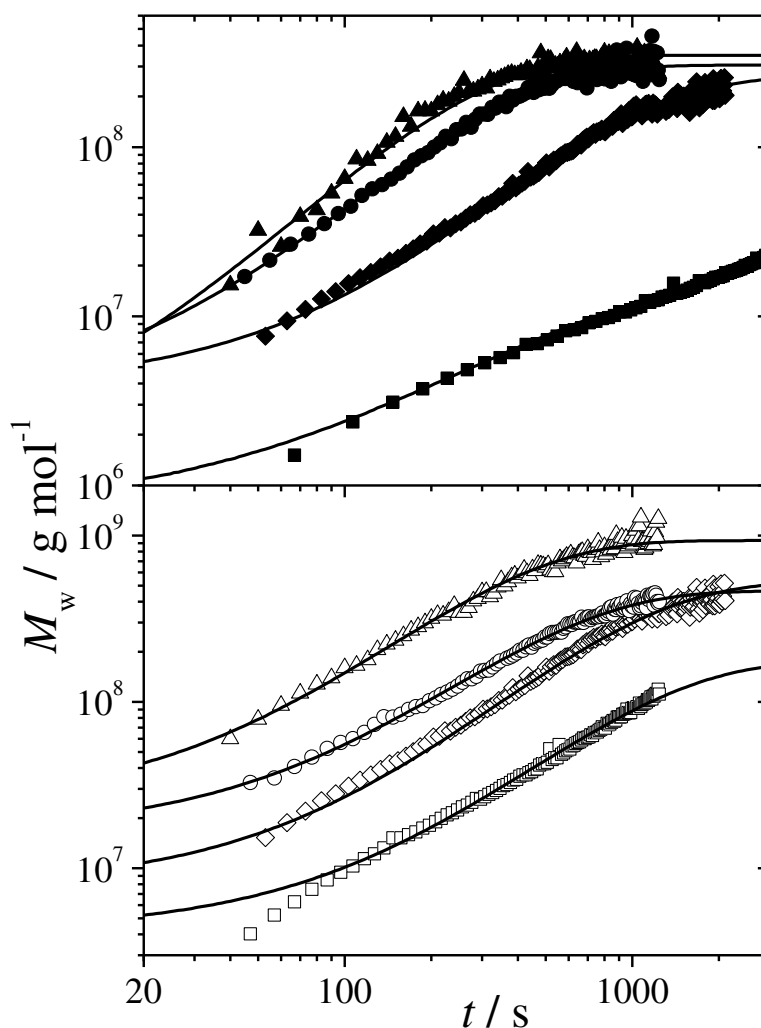


Figure SI-3. Evolution of the weight-averaged molar mass at variable Mg^{2+} content (top) and at variable dye concentration (bottom). Error bars are not shown for the sake of clarity. The denotations of the symbols are given by Table SI-1. Since the results obtained for different dye concentrations lie close to each other, the curves with symbols (\diamond), (\circ) and (\triangle) are shifted by factors of 2, 4 and 8, respectively, in order to visually set them apart from each other. The continuous lines represent fits with to the Lomakin model¹⁹ based on eq(SI-16) of the Supporting Information without allowing for initial aggregates, i.e. assuming $[B]_{t=0}^{(0)} = 0$. The logarithmic scale of the ordinate highlights the deviations of the fits from the experimental data at low molar masses.

Table SI-2. Linear mass densities M_L and persistence lengths l_p evaluated by modeling the correlation of R_g and $M_{w,ag}$, obtained from eq(5) and eq(33), respectively, with eq(34). Corresponding fits are shown in Figure 5 in the manuscript.

parameter: symbol	M_L [g mol ⁻¹ nm ⁻¹]	l_p [nm]	[Mg] ²⁺ / mM	c_{dye} / g l ⁻¹
(■)	41000	230	1.63	0.066
(◆)	98000	180	2.44	0.066
(●)	140000	190	3.25	0.066
(▲)	130000	230	5.20	0.066
(□)	71000	150	2.44	0.044
(◇)	98000	180	2.44	0.066
(○)	48000	180	2.44	0.088
(△)	65000	180	2.44	0.124

Reference.

1. Lomakin, A.; Teplow, D. B.; Kirschner, D. A.; Benedek, G. B. *Proc. Natl. Acad. Sci. USA* **1997**, *94*, 7942-7947.

6. Coaggregation of Two Anionic Azo Dye-stuffs: A Combined Static Light Scattering and Small Angle X-Ray Scattering Study

Reproduced with permission from *J. Phys. Chem. B* **2014**, *118*, 7618-7629.
Copyright 2014 American Chemical Society.

Coaggregation of Two Anionic Azo Dyestuffs: A Combined Static Light Scattering and Small-Angle X-ray Scattering Study

Rolf Michels,[†] Günter Goerigk,[‡] Ulla Vainio,[§] Jérémie Gummel,[¶] and Klaus Huber^{*,†}

[†]Physikalische Chemie, Universität Paderborn, Warburger Straße 100, D-33098 Paderborn, Germany

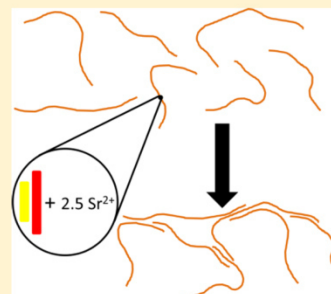
[‡]Institut Weiche Materie und Funktionale Materialien, Helmholtz-Zentrum Berlin, Hahn-Meitner-Platz 1, D-14109 Berlin, Germany

[§]Deutsches Elektronen-Synchrotron, Notkestraße 85, D-22607 Hamburg, Germany

[¶]Procter & Gamble Technical Centre, Whitley Road, Longbenton, Newcastle Upon Tyne, Tyne And Wear, NE12 9SR, United Kingdom

Supporting Information

ABSTRACT: The formation of azo dyestuff aggregates in dilute aqueous solution induced by the addition of Mg^{2+} , Ca^{2+} , Sr^{2+} , or Ba^{2+} ions is followed by time-resolved static light scattering (SLS) and time-resolved small-angle X-ray scattering (SAXS). Time-dependent molar mass data of the growing aggregates is interpreted by means of a kinetic model introduced by Lomakin et al. (*Proc. Natl. Acad. Sci. U.S.A.* **1996**, *93*, 1125) for the description of β -amyloid aggregation. This interpretation reveals significant trends within the homologous series of alkaline earth cations. The trends refer to the nucleation and the growth rate of the dyestuff fibers. Time-resolved SAXS experiments indicate that these first two stages are followed by a third one during which a network forms by partial lateral alignment of fibers. At high enough dyestuff concentrations, this network formation even leads to a gel-like phase. Anomalous SAXS (ASAXS) on such a gel phase formed upon the addition of Sr^{2+} revealed the extent of neutralization of the dyestuff molecules within the gel by the specifically interacting alkaline earth cations.



INTRODUCTION

Anionic azo dyestuffs form fiberlike aggregates in aqueous solution,¹ which resembles the formation of protein aggregates. Although proteins are usually much larger than anionic azo dyestuff molecules, they bear striking similarities with the latter. Both types of molecules are organic compounds with ionic residues, polar groups, and hydrophobic patches the interplay of which controls their solubility in water.

In several preceding papers,^{2–5} we have identified a binary system of two azo dyestuffs which form aggregates in dilute aqueous solution on a time scale of minutes if magnesium ions are added. This property makes the respective dyestuff system an exceptionally interesting candidate for time-resolved investigation of aggregate formation by multiangle light scattering.

The binary system includes a red dye and a yellow dye hereafter denoted as RD and YD. Each of the two components forms stable aggregates in dilute aqueous solution. Aggregates formed in pure YD solution are significantly larger but less compact than aggregates formed in pure RD solution. In solutions of mixed RD and YD, a bimodal system is observed in which small dyestuff monomers and oligomers coexist with micelle-like aggregates with a size of about 50 nm, while the larger and less compact aggregates observed in pure YD solutions have disappeared. This points to a rearrangement of the constituent molecules from pure aggregates as soon as they are mixed. The addition of magnesium ions to the resulting

mixed RD and YD solution initiates a self-assembly process yielding large wormlike aggregates that grow to a length of several micrometers. An addition of magnesium ions to a pure RD or a pure YD solution does not cause any comparable aggregation. Interestingly, the large wormlike aggregates induced by the presence of magnesium ions exhibit a 1:1 molar stoichiometry of RD and YD. The discovery of this stoichiometry supports the above-mentioned hypotheses of a rearrangement of the dyestuff molecules upon combining solutions of pure RD and pure YD. Probably, stoichiometric aggregates of RD and YD with a ratio of 1:1 are already established during this rearrangement, i.e., prior to the addition of magnesium ions.⁴

The kinetics of self-assembly of RD and YD in the presence of magnesium ions could be described by a short period of nucleation followed by an extended growth period. During the growth period, nucleation comes to a standstill and the generated fibers grow by a stepwise addition of small building units.⁵ The period of nucleation itself could not yet be directly investigated since the self-assembly experiments were initiated by the time-consuming hand mixing of dyestuff solution with alkaline earth solutions. In the present work, the combination of these two components will be performed by means of

Received: March 7, 2014

Revised: June 11, 2014

Published: June 17, 2014

stopped flow devices, which enable a much faster and more defined mixing. Since this makes earlier stages of the dyestuff aggregation observable, it was originally intended to provide a direct access to the nucleation period of the process. However, nucleation either provided scattering signals not good enough to enable time-resolved experiments at low concentration or was too fast for time-resolved experiments at higher concentration. Nevertheless, application of a defined and fast mixing by means of stopped-flow devices turned out to be a prerequisite for performing time-resolved small-angle X-ray scattering (SAXS) experiments.

Two interesting yet unanswered questions concerning the dyestuff aggregation will be in the focus of the present work. The first one is aimed at a better understanding of the mechanism by which the dyestuff fibers form networks. Hints on the existence of branching as the origin of networks have already been provided in the preceding study⁵ by the correlation between the radius of gyration and the contour length of the aggregates as well as by TEM micrographs. The present work will address this feature of mature dyestuff fibers by means of time-resolved SAXS on the alkaline earth cation induced aggregation. The second question concerns the number ratio of alkaline earth cations per dyestuff molecule and the spatial distribution of alkaline earth counterions within the dyestuff aggregates, which shall be addressed by means of anomalous small-angle X-ray scattering (ASAXS). The use of X-rays requires a high enough scattering contrast of the investigated species with respect to its (aqueous) environment, which is provided by preferably heavy ions. Therefore, the introductory feature of the present work will consist in a series of time-resolved static light scattering (SLS) experiments comparing the dyestuff aggregation induced by homologous Mg^{2+} , Ca^{2+} , Sr^{2+} , and Ba^{2+} ions. The results of this comparative series will be discussed first since they represent the necessary background for the use of Sr^{2+} and Ba^{2+} ions in the succeeding time-resolved SAXS and ASAXS experiments.

EXPERIMENTAL METHODS

All experiments within this work are performed with a molar ratio of RD:YD = 1:1 in agreement with the stoichiometry found for the dyestuff aggregates which form in the presence of magnesium ions.⁴ The temperature is set to 25 °C and the pH values of aqueous samples lie in between 6.6 and 6.8. For all aggregation experiments, a sufficiently high excess of positive electric charges from alkaline earth cations with respect to the negative charges from the anionic dyestuffs is used. Therefore, aggregation always leads to a complete consumption of all dyestuff monomers. Additionally, the excess of positive charges assures the screening of interparticular electrostatic correlations.

Materials. Figure 1 shows the chemical structures of the two dyes under present consideration. Dyestuffs were received as a donation from Ciba Geigy, Switzerland. They were available as sodium salts and were purified by dialysis as described earlier.² Magnesium sulfate and the chlorides of calcium, strontium, and barium (assay >99.5%, respectively) were purchased from Sigma-Aldrich.

Preparation of Time-Resolved Scattering Experiments. A solution containing 4.47 g/L (4.2 mM) RD and 2.13 g/L (4.2 mM) YD, corresponding to a total dye concentration of 6.6 g/L with a molar ratio of RD:YD = 1:1, as well as four solutions containing 13 mM $MgSO_4$, 13 mM $CaCl_2$, 13 mM $SrCl_2$, and 13 mM $BaCl_2$, were prepared in

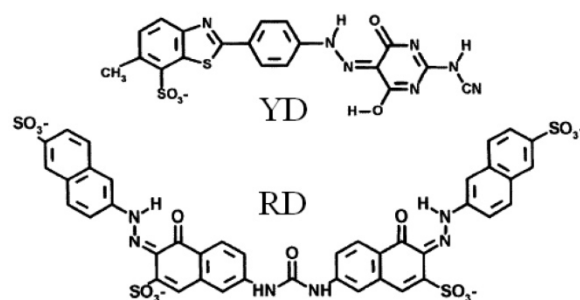


Figure 1. Molecular structures of the yellow dye (YD) and the red dye (RD). The molar mass of the dyestuffs including their sodium counterions is 505 g mol^{-1} for YD and 1061 g mol^{-1} for RD. A dimer consisting of one RD and one YD molecule will be considered as "building unit".

distilled water, respectively. These five solutions served as stock solutions and were further diluted in order to achieve the desired concentrations for the time-resolved scattering experiments. Dyestuff aggregation was initiated by mixing equal amounts of an alkaline earth chloride solution and a mixed RD and YD solution.

For the SLS experiments, this mixing was performed by means of an SF-20 stopped flow device from BioLogic. As demonstrated in the Supporting Information (Figure S1), the use of this device yields similar results as hand mixing. The SF-20 was used to simultaneously press the mixed dyestuff solution and an alkaline earth chloride solution through syringe filters (Macherey-Nagel CHROMAFIL PET-20/25, $1.2 \mu\text{m}$ pore size) installed directly at the opposing entrances of a T-mixer. After passing the mixer, the mixed solutions containing the two dyestuffs and one type of alkaline earth cations were guided directly into cylindrical quartz cuvettes (Helma, diameter = 20 mm) that had been cleaned and placed inside the goniometer of the light-scattering instrument. For all experiments, a total flow rate of 2 mL/s was used to push a total volume of 3 mL into the respective cuvette. This procedure enabled the recording of the first SLS curve about 3 s after initiation of the aggregation process, i.e., after injecting the respective solutions into the scattering cell. A more precise knowledge of the sample age and hence application of the actual "stopped flow" would not have been of advantage during SLS measurements since the filling of the scattering cell as well as the recording of a single SLS curve took at least 1 s, respectively. The samples used for SLS experiments contained 0.033 or 0.066 g/L dyestuff (0.021 or 0.042 mM) and in between 0.8 and 3.2 mM alkaline earth cations.

For SAXS experiments, the mixing of the two components was performed with a SF-400 stopped flow device from BioLogic installed at the ID02 beamline of the ESRF. X-ray scattering was measured in a flow-through cell connected to the outlet of the stopped flow device. All time-resolved experiments reported within the present article were initiated at a total flow rate of 2 mL/s . In this way, the first SAXS curve could be recorded 30 ms after the initiation of the aggregation process corresponding to the dead time between the mixing point and the beam position on the sample (= measurement position). Damaging of the samples by the highly intensive X-ray beam could only be avoided by reducing the sample exposure time for a single measurement to 5 ms, which in turn made higher dyestuff concentrations than for the light scattering experiments

necessary in order to achieve an acceptable quality of the SAXS signal. The dyestuff concentrations used for SAXS measurements were 0.11 and 0.33 g/L (0.07 and 0.21 mM). The alkaline earth concentrations varied between 1.6 and 3.2 mM.

Time-Resolved Static Light Scattering. Measurements were carried out with a home-built multiangle instrument, which had been developed by Becker and Schmidt.⁶ A He–Ne laser from Melles Griot, operating at a wavelength of $\lambda = 632.8$ nm, served as light source. The scattering signal was detected within an angular range of $25.8^\circ < \theta < 143.1^\circ$, corresponding to a q -regime of $4.6 \times 10^{-3} \text{ nm}^{-1} < q < 2.6 \times 10^{-2} \text{ nm}^{-1}$, where

$$q = \frac{4\pi n}{\lambda} \sin\left(\frac{\theta}{2}\right) \quad (1)$$

is the scattering vector and n is the refractive index of the solvent. As a primary result from any SLS measurement, the time-dependent Rayleigh ratio of the aggregating sample

$$R(q, t) = \frac{S_{\text{sample}}(q, t) - S_{\text{solvent}}(q)}{S_{\text{standard}}(q)} R_{\text{standard}} \quad (2)$$

was calculated. In eq 2, $S_{\text{sample}}(q, t)$ is the time-dependent scattering signal of a mixed dyestuff solution activated with alkaline earth cations, R_{standard} is the absolute Rayleigh ratio of toluene, and $S_{\text{solvent}}(q)$ and $S_{\text{standard}}(q)$ are the scattering signals of the solvent (water) and the standard (toluene), respectively.

Time-Resolved SAXS. Measurements were performed at the ID02 beamline of the ESRF. Two-dimensional SAXS patterns were measured by means of a CCD camera. These patterns were subsequently corrected for the dark current and for spatial inhomogeneities of the detector and were normalized to an absolute scale using the transmitted beam intensity, the pixel size of the detector, and the respective sample-to-detector distance.⁷ Each normalized two-dimensional SAXS pattern was azimuthally averaged in order to obtain the corresponding one-dimensional scattering profile. Subtraction of the solvent scattering resulted in a net differential scattering cross section of the solute denoted as $d\Sigma/d\Omega$. Hence, all final scattering curves were obtained as differential scattering cross sections $d\Sigma/d\Omega$ in units of reciprocal meters as functions of momentum transfer q .

Measurements were performed at sample-to-detector distances of 1, 5, and 10 m in order to access the broadest possible q -regime. All time-resolved scattering runs were initiated by a shot with the SF-400. Due to the finite readout time of the CCD camera, the frequency of measurements was restricted to 5 s^{-1} (200 ms per single measurement). However, the time resolution of the SAXS experiments was not strictly limited to this frequency, since it was possible to record several series of scattering curves with various starting points. To give but an example, if a first series of scattering curves was recorded at times $t = 50 \text{ ms}$, 250 ms , 450 ms , ..., the frequency of measurements could be doubled by combining this data set with another series of scattering curves recorded at $t = 150 \text{ ms}$, 350 ms , 550 ms , Yet, the primary scattering curves obtained in this way were of poor statistical quality due to the short exposure time (5 ms) of a single measurement. Therefore, all time-resolved SAXS data shown within the Results and Discussion section have been calculated by averaging at least five primary curves, resulting in a better statistical quality at the expense of time resolution. The good reproducibility of those averaged curves enabled the combination of corresponding data

measured at different sample-to-detector distances (see Figure S2 in the Supporting Information).

Evaluation of Time-Resolved Scattering Data. The time-dependent Rayleigh ratio $R(q, t)$ obtained from time-resolved SLS was evaluated by means of Zimm's approximation^{8,9}

$$\frac{Kc}{R(q, t)} = \frac{1}{M_w(t)} \left(1 + \frac{\langle R_g^2 \rangle_z(t)}{3} q^2 \right) + k_1 q^4 \quad (3)$$

where c is the total mass concentration of dyestuff and the contrast factor

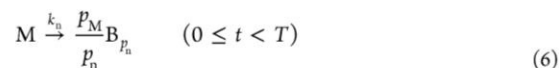
$$K = \frac{4\pi^2 n^2}{\lambda^4 N_A} \left(\frac{dn}{dc} \right)^2 \quad (4)$$

depends on the vacuum wavelength λ of the laser, the refractive index n of the solvent, the increment of refractive index dn/dc of the scattering particles, and Avogadro's number N_A . It was demonstrated in preceding works^{2,10,11} that the approximation given by eq 3 holds up to $q^2 \langle R_g^2 \rangle_z = 4$ for the scattering patterns of wormlike chains. Its application makes the apparent weight-averaged molar mass $M_w(t)$ and the z -averaged square radius of gyration $\langle R_g^2 \rangle_z(t)$ of the solute accessible from fitting $Kc/R(q, t)$ by a polynomial quadratic in q^2 if K and c are known. A previously estimated value of $dn/dc = 0.374 \text{ mL g}^{-1}$ was used for the dyestuff mixture in H_2O .⁴ The coefficient k_1 of the q^4 term in eq 3 served as a fitting parameter only and was not further considered.

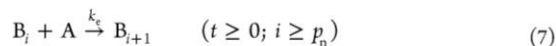
The time-dependent weight-averaged molar mass data $M_w(t)$ obtained by the application of eq 3 was approximated by kinetic fits with the Lomakin model.¹² The Lomakin model assumes an initial coexistence of monomeric units "A" at a molar concentration $[A]^*$ and micellar aggregates M consisting of p_M monomeric units.



If the total molar concentration of monomers within a sample is $[A]_{\text{tot}}$, the molar concentration of micellar aggregates at time $t = 0$ is $([A]_{\text{tot}} - [A]^*)/p_M$. Within the period $0 \leq t < T$, the micellar aggregates generate nuclei B_{p_n} consisting of p_n monomeric units, with k_n being the rate constant of the first-order nucleation reaction.



At any time $t \geq 0$, nuclei formed from the micellar aggregates are capable of growing by a consecutive stepwise addition of monomeric units.



As indicated in eq 7, the rate constant of the second-order growth reaction, k_e , is independent of the degree of polymerization i of the growing aggregates B_i . This simplification is justified if we assume that the number of reactive sites per growing aggregate is independent of i , which is a reasonable approach for worm-, rod-, or chainlike aggregates where longitudinal growth predominates over lateral growth. Another feature of the Lomakin model¹² is that the monomer concentration constantly remains at the "critical micelle concentration" $[A]^*$ as long as micellar aggregates are existent; i.e., the equilibrium represented by eq 5 is reached infinitely

fast. During this period of time, monomers that are consumed by chain growth (eq 7) will be instantly replenished at the expense of micelles. This in turn establishes a time T by which all micellar aggregates will be consumed. Hence at $t > T$, nucleation is terminated and the monomer concentration $[A](t) < [A]^*$ continuously decreases due to the growth of existing aggregates according to eq 7. Provided that $[A]_{\text{tot}}$ is known and excluding the existence of seeds, the Lomakin model¹² allocates five independent fitting parameters k_n , k_c , $[A]^*$, p_n and p_M . The dependence of the first three moments of the particle mass distribution on these parameters has been derived in the preceding article.⁵ The k th moment is defined as

$$[B]^{(k)} = \sum_i i^k [B_i] \quad (8)$$

where $[B_i]$ is the molar concentration of aggregates B_i with degree of polymerization i . The zeroth moment $[B]^{(0)}$ represents the molar concentration of aggregates. In the case of the Lomakin model,¹² it reaches its final value $[B]_{t=T}^{(0)}$ at time T when nucleation is terminated. The first moment $[B]^{(1)}$ corresponds to the total amount of monomers that are incorporated into the aggregates. The second moment $[B]^{(2)}$ finally enables the calculation of the weight-averaged molar mass, which is the primary result of SLS.

$$M_w(t) = \begin{cases} \frac{M_A}{[A]_{\text{tot}}} ([A]^* + p_M^2 [M](t) + [B]^{(2)}(t)), & \text{for } 0 \leq t < T \\ \frac{M_A}{[A]_{\text{tot}}} ([A](t) + [B]^{(2)}(t)), & \text{for } T \leq t \end{cases} \quad (9)$$

In eq 9, M_A is the molar mass of a monomeric unit or building unit. The primary results from SAXS measurements are the net differential scattering cross section of the solute, $d\Sigma/d\Omega(q)$, and the Porod invariant.¹³

$$Q(t) = \int \frac{d\Sigma}{d\Omega}(q, t) q^2 dq \\ = 2\pi^2 (\Delta\rho)^2 \phi(t) (1 - \phi(t)) \cong k_2 \phi(t) \quad (10)$$

In eq 10, $\Delta\rho$ and $\phi(t)$ represent the excess scattering length density and the volume fraction of the solute, respectively. For small volume fractions, $Q(t)$ becomes proportional to $\phi(t)$.

The scattering from samples was interpreted by means of the cylinder model.¹⁴ The corresponding formulas are given in the Supporting Information (eqs SI-1 and SI-2).¹⁴

Anomalous Small-Angle X-ray Scattering (ASAXS).

Experiments were carried out with two samples containing RD and YD in a molar ratio of 1:1 where strontium ions were used to induce the dyestuff aggregation. Both samples contained the same total dyestuff concentration of 0.66 g/L (0.42 mM), but differed in their strontium chloride concentrations, which were 6.5 and 13 mM, respectively. In this concentration regime, the entire aggregation proceeds in a few seconds and almost instantly causes a separation into a colorless, aqueous phase and a dark red gel-like phase that contains the entire amount of dyestuff molecules in aggregated state. Due to the higher mass density of this dyestuff gel with respect to the colorless supernatant phase, it was possible to discriminate between the two phases and to effectively separate them by centrifugation. The two samples used for the present work were prepared by mixing an aqueous solution of RD and YD (molar ratio = 1:1) with the respective aqueous strontium chloride solution. The mixing of these two components and the following

centrifugation (5 min, 1500g) were carried out directly in a cylindrical scattering cuvette (Hilgenberg, Malsfeld, Germany, 4 mm inner diameter). The gel-like dyestuff phase had thereupon formed with a height of 5–10 mm at the bottom of the scattering cuvette. The two samples prepared in this way have been used to determine the concentration of Sr^{2+} ions that are specifically bound to the dyestuff aggregates within the gel phase, $[\text{Sr}^{2+}]_{\text{spec}}$ and to estimate the dyestuff concentration within the gel phase, $c_{\text{RY-b}}$. The estimation of $c_{\text{RY-b}}$ was based on X-ray absorption measurements and is outlined in detail in the Supporting Information. The determination of $[\text{Sr}^{2+}]_{\text{spec}}$ by means of ASAXS will be briefly described in the following. Knowledge of $[\text{Sr}^{2+}]_{\text{spec}}$ and $c_{\text{RY-b}}$ will give access to the extent to which anionic dyestuff charges within the aggregates are neutralized by Sr^{2+} cations.

In the vicinity of an X-ray absorption edge, the scattering length of an ion or atom is a function of the photon energy E and can be written as

$$b(E) = r_{\text{el}}(Z + f'(E) + if''(E)) \quad (11)$$

where $r_{\text{el}} = 2.82 \times 10^{-15}$ m is the scattering length of an electron, Z is the atom number, and $f'(E)$ and $f''(E)$ are the real part and the imaginary part of the energy-dependent anomalous scattering factor, respectively. Due to this energy dependence, it is possible to vary the partial scattering stemming from a selected species by choosing photon energies close to an absorption edge of this species. In the present case, SAXS patterns of the gel-like dyestuff phase were recorded in the vicinity of the strontium K-edge ($E_{\text{edge}} = 16\,105$ eV) at three different photon energies ($E_1 = 15\,500$ eV, $E_2 = 16\,076$ eV, $E_3 = E_{\text{edge}}$). The measurements have been performed at the B1 beamline of the HASYLAB at DESY (Hamburg, Germany). According to eq 11, the contributions of scattering from strontium ions to the three measured total scattering curves $d\Sigma/d\Omega(q, E_1)$, $d\Sigma/d\Omega(q, E_2)$, and $d\Sigma/d\Omega(q, E_3)$ are different. This enables the extraction of the pure resonant scattering contribution which refers solely to the strontium ions

$$S_{\text{res}}(q) = \left[(f'_k - f'_j) \left(\frac{d\Sigma}{d\Omega}(q, E_i) - \frac{d\Sigma}{d\Omega}(q, E_k) \right) \right. \\ \left. + (f'_i - f'_k) \left(\frac{d\Sigma}{d\Omega}(q, E_j) - \frac{d\Sigma}{d\Omega}(q, E_k) \right) \right] \\ \left/ \left[(f'_k - f'_j)(f_i'^2 - f_k'^2 + f_j''^2 - f_k''^2) \right. \right. \\ \left. \left. + (f'_i - f'_k)(f_j'^2 - f_k'^2 + f_j''^2 - f_k''^2) \right] \quad (12)$$

In eq 12, the indices i, j, k indicate the three energies E_i, E_j , and E_k where $i, j, k \in \{1, 2, 3\}$ and $i \neq j, j \neq k$, and $k \neq i$. Any background scattering caused by solvent molecules is canceled in the numerator of the right-hand side of eq 12. Due to the symmetry of eq 12 with respect to i, j , and k , only three independent combinations exist in order to calculate $S_{\text{res}}(q)$ from eq 12. These combinations can be represented by $(i = 1, j = 2, k = 3)$, $(i = 2, j = 3, k = 1)$, and $(i = 3, j = 1, k = 2)$. A detailed outline of this combinatorics and its statistical consequences for the determination of $S_{\text{res}}(q)$ has been presented by Goerigk.^{15,16} In the present work, the final pure resonant scattering is calculated as an average of the three independent combinations. Principally, $S_{\text{res}}(q)$ refers to the scattering of all strontium ions, independent of whether they are specifically bound to dyestuff aggregates or unbound (i.e.,

freely dissolved in water). However, due to the lack of a spatial correlation between the unbound strontium ions, their contribution to $S_{\text{res}}(q)$ in the low q regime is negligible. Therefore, the resonant invariant

$$Q_{\text{res}} = \int S_{\text{res}}(q)q^2 dq \quad (13)$$

obtained from the low q regime that is accessed by small-angle scattering methods solely addresses strontium ions that are spatially correlated to the dyestuff aggregates. Their molar concentration $[\text{Sr}^{2+}]_{\text{spec}}$ is related to the resonant invariant by¹⁷

$$[\text{Sr}^{2+}]_{\text{spec}} = \frac{2Q_{\text{res}}R_{\text{Sr}}^3}{3\pi N_{\text{A}}r_{\text{el}}^2} \quad (14)$$

In eq 14, $R_{\text{Sr}} = 126$ pm is used for the radius of a strontium ion.¹⁸

RESULTS AND DISCUSSION

Results from Time-Resolved SLS. Time-dependent weight-averaged molar mass data $M_w(t)$ of growing dyestuff aggregates were obtained from eq 3 and subsequently modeled with the Lomakin model.¹² To this end, eq 9 was adapted to the experimental data by least-squares fits, where seeds have been excluded as outlined in ref 5. The molar mass of a monomeric unit was set to $M_A = 1451 \text{ g mol}^{-1} + 2.5M_{\text{M}^{2+}}$, signifying the composite molar mass of the anionic RD and YD (1451 g mol^{-1}) and of the number of alkaline earth cations M^{2+} required to neutralize the total negative charge of a red and a yellow dye anion ($2.5M_{\text{M}^{2+}}$).⁵ As is demonstrated further down below, the present ASAXS experiments justify such an approach. The choice of the monomeric unit, and with it of M_A , does not influence the interpretation of kinetic data because M_A solely represents a scaling factor (see eq 9).

The Lomakin model¹² as we shall apply it is based on the rate constants of nucleation and elongation, k_n and k_e , the critical micelle concentration $[A]^*$, and the numbers of monomers per nucleus and per micelle, p_n and p_M . In order to facilitate the identification of possible trends in parameters that are freely variable during fitting, we had to limit their number to the greatest possible extent. Therefore, we had to identify appropriate candidates that might be excluded from variation during fitting without reducing the significance of the remaining variable model parameters. To this end, we performed two fitting cycles with all sets of experimental data. In a first fitting cycle, all five model parameters k_n , k_e , $[A]^*$, p_n , and p_M were treated as adjustable. This first fitting cycle revealed two general aspects, which will justify our choice of the model parameters to be excluded from variation during the second fitting cycle. The first general aspect is reflected in the fact that we found

$$[B]_{t=T}^{(0)} \cong \frac{[B]_{t=T}^{(1)}}{p_n} = \frac{[A]_{\text{tot}} - [A]^*}{p_n} \quad (15)$$

for all fits. Equation 15 holds if the number of monomers added to a nucleus until $t = T$ is on average much smaller than p_n . This in turn indicates that, during nucleation, the amount of monomers transferred from micelles into nuclei per time is much larger than the amount of monomers added to existing nuclei/aggregates per time. We will therefore denote the first general aspect indicated by eq 15 as “fast nucleation”. Two consequences of a fast nucleation are $[B]_{t=T}^{(1)} \cong [B]_{t=T}^{(2)}/p_n$ and a

very narrow polydispersity of the ensemble of aggregates at time T . The duration T of a fast nucleation can be approximated as

$$T \cong \frac{1}{k_n} \ln \left(\frac{p_n^2 k_n}{p_M k_e [A]^*} \right) \quad (16)$$

In the limit of large k_n eq 16 approaches $\lim_{k_n \rightarrow \infty}(T) = 0$. This introduces the second general aspect we would like to address: For any fit obtained under free variation of all five model parameters, the period of nucleation is terminated prior to the acquisition of the first scattering curve. This is similar to what was found in the preceding work on the aggregation of RD and YD in the presence of Mg^{2+} .⁵ The results from the first fitting cycle enable us to assume that all aggregation processes we have investigated exhibit fast nucleation in terms of eq 15 and that the end of the nucleation period ($t = T$) is reached before the first experimental mass data can be recorded.

Four of the model parameters, that is, k_n , $[A]^*$, p_n , and p_M , govern the period of nucleation ($t < T$) and will therefore be denoted as “nucleation parameters” in the following. Their impact on $M_w(t > T)$ is merely indirect. It is this indirect impact of the nucleation parameters on the period $t > T$ we need to scrutinize in order to decide whether it is at all possible to gain significant information about a particular nucleation parameter by its variation in fitting $M_w(t > T)$. If this is not the case, we shall exclude this particular nucleation parameter from independent variation during fitting.

Lomakin model¹² curves of M_w at $t > T$ can generally be characterized by three features. (i) The maximum value is given by the limiting plateau $M_w(t \rightarrow \infty)$ where total monomer consumption is achieved. Given that $[A]_{\text{tot}}$ is known, the plateau value $M_w(t \rightarrow \infty)$ is entirely determined by the total number of nuclei formed by the time T , $[B]_{t=T}^{(0)}$. In fact, $M_w(t \rightarrow \infty)$ is proportional to the inverse of $[B]_{t=T}^{(0)}$. The interrelation of $[B]_{t=T}^{(0)}$ with the nucleation parameters in turn becomes quite simple in the case of a fast nucleation: from eq 15, we see directly that $[B]_{t=T}^{(0)}$ and hence the plateau value $M_w(t \rightarrow \infty)$ are independent of k_n and p_M . (ii) At the end of a fast nucleation, the second moment of the particle mass distribution can be approximated as $[B]_{t=T}^{(2)} \cong p_n [B]_{t=T}^{(1)} = p_n ([A]_{\text{tot}} - [A]^*)$ (cf. eq 15). Since the weight-averaged molar mass achieved at the end of nucleation solely depends on $[B]_{t=T}^{(2)}$ and on the monomer concentration, $M_w(t=T)$ is likewise independent of k_n and p_M . (iii) The growth period during which the weight-averaged molar mass continuously increases depends on k_e , p_n , and $[A]^*$, whereby the latter two parameters determine $M_w(t=T)$ and $M_w(t \rightarrow \infty)$.

Thus, only p_n , $[A]^*$, and k_e have a considerable impact on the period in which we have experimental $M_w(t)$ data available. Therefore, we excluded p_M and k_n from independent variation during our second fitting cycle by setting $p_M = p_n$ and $k_n = 100 \text{ s}^{-1}$ for all fits. This approach on the one hand uses nucleation in its most simple form ($M \rightarrow B_{p_n}$) and accomplishes a fast nucleation in terms of $k_n \gg k_e p_M [A]^* / p_n^2$, which has also been revealed when p_M and k_n were freely varied as additional adjustable parameters. On the other hand, this approach provides a statistically solid basis for the interpretation of the results obtained for p_n , $[A]^*$, and k_e .

The parameter values resulting from the second cycle of Lomakin model¹² fits performed under variation of p_n , $[A]^*$ and k_e with $k_n = 100 \text{ s}^{-1}$ and $p_n = p_M$ are summarized in Table

Table 1. Model Parameters Obtained from Fitting the Lomakin Model¹² in Terms of Eq 9 to the Experimental Data^a

c_{dye} (g L ⁻¹)	[alkaline earth]	k_e (m ³ mol ⁻¹ s ⁻¹)	[A]* (mM)	p_n	$[B]_{t=T}^{(0)}$ (mM)	$[A]^*/[A]_{\text{tot}}$
0.066	3.2 mM Mg ²⁺	1.7×10^4	0.039	2.0×10^4	2.2×10^{-7}	0.899
0.033	1.6 mM Ca ²⁺	6.8×10^3	0.018	6.8×10^3	4.5×10^{-7}	0.857
0.033	3.2 mM Ca ²⁺	2.0×10^5	0.021	1.1×10^3	1.3×10^{-7}	0.993
0.066	3.2 mM Ca ²⁺	1.3×10^5	0.042	7.2×10^3	1.3×10^{-7}	0.977
0.033	1.6 mM Sr ²⁺	6.3×10^4	0.020	6.4×10^2	2.3×10^{-7}	0.995
0.033	3.2 mM Sr ²⁺	4.1×10^5	0.019	2.1×10^3	9.1×10^{-8}	0.987
0.066	1.6 mM Sr ²⁺	4.4×10^4	0.038	6.1×10^3	2.9×10^{-7}	0.955
0.066	3.2 mM Sr ²⁺	5.7×10^5	0.038	1.6×10^4	8.2×10^{-8}	0.966
0.033	1.6 mM Ba ²⁺	1.8×10^5	0.018	5.8×10^2	9.8×10^{-8}	0.997
0.033	3.2 mM Ba ²⁺	9.8×10^5	0.016	3.1×10^4	8.0×10^{-8}	0.864
0.066	0.8 mM Ba ²⁺	7.6×10^3	0.037	3.9×10^2	5.6×10^{-7}	0.994
0.066	1.63 mM Ba ²⁺	1.2×10^5	0.036	8.6×10^2	1.2×10^{-7}	0.992
0.066	3.25 mM Ba ²⁺	2.2×10^6	0.035	1.6×10^4	7.2×10^{-8}	0.964

^a k_e is the rate constant of elongation, [A]* the critical micelle concentration, and $[B]_{t=T}^{(0)}$ the number of aggregates formed by the time T when no micelles are left and nucleation is terminated. p_n is the number of monomers per nucleus set equal to the number of monomers per micelle. $[A]_{\text{tot}}$ is the (constant) total molar monomer concentration, comprising free monomers, monomers in micelles, and monomers in aggregates. For all fits, $k_n p_n^2 / (k_e p_M [A]^*) > 15$ and $T < 0.1$ s.

1. Four out of these fits are exemplified in Figure 2A, suggesting both an acceleration of the aggregation process and an increase of the final weight-averaged molar mass $M_w(t \rightarrow \infty)$ within the series Mg²⁺, Ca²⁺, Sr²⁺, Ba²⁺. These trends are nicely reflected in the values of the rate constant of chain elongation k_e and of the total molar aggregate concentration $[B]_{t=T}^{(0)}$ illustrated in Figure 2B. An increase of the final weight-averaged molar mass occurs

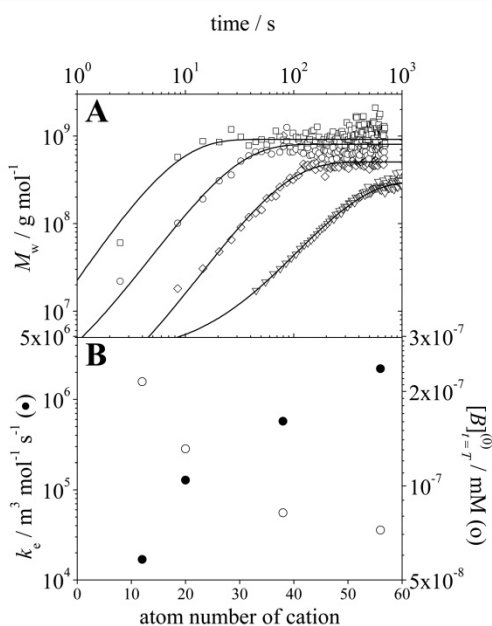


Figure 2. (A) Evolution of the weight-averaged molar mass of growing mixed RD and YD aggregates in the presence of Mg²⁺ (∇), Ca²⁺ (\diamond), Sr²⁺ (\circ), and Ba²⁺ (\square). All samples contain 0.066 g/L of mixed RD and YD (at a molar ratio of 1:1) and 3.25 mM of the respective alkaline earth cation. Continuous lines represent kinetic fits with the Lomakin model.^{5,12} (B) Rate constants of elongation, k_e (\bullet), and molar particle concentration at time $t \geq T$ when nucleation is terminated, $[B]_{t=T}^{(0)}$ (\circ). The parameters are extracted from the fits shown in (A) and are represented as a function of the type of alkaline earth cation.

with a decrease of the number of particles. Similar trends are found for each particular alkaline earth species by increasing the concentration of alkaline earth ions (cf. Table 1 and ref 5), whereas a change of the dyestuff concentration does not induce any comparable effect.

In terms of the Lomakin model,¹² the impact of the type and the concentration of alkaline earth ions on k_e may be interpreted as a modification of the activity of the monomeric species A and/or of the activity of the ends of growing chain B_r. The dependence of such an activation on the type of alkaline earth cation cannot be explained by its diffusion properties, which are similar for Mg²⁺, Ca²⁺, Sr²⁺, and Ba²⁺ in aqueous solution.¹⁹ Hence this dependence has to be attributed to specific interactions between the dyestuff species and the alkaline earth cations the magnitude of which increases from Mg²⁺ to Ba²⁺.

A physically meaningful interpretation of the two remaining fit parameters p_n and [A]* is not evident. The values of p_n show neither any correlation with the total dyestuff concentration nor with the alkaline earth concentration. This is not surprising since p_n is sensitive to the first points of the experimental data where the relative uncertainty is highest. The values of [A]* are consistently above 85% of $[A]_{\text{tot}}$, which is still compatible with the situation in mixed RD and YD solutions in the absence of alkaline earth ions, where the major part of dyestuff molecules form small oligomers whereas only a minor part is arranged in larger, micelle like aggregates.⁴ However, the crude trend $[A]^* \sim [A]_{\text{tot}}$ may at first glance contradict the concept of micellization and hence requires an additional comment. Even the classical micellization theory predicts a correlation between the equilibrium concentration of monomer and the total amphiphile concentration around and beyond the critical micelle concentration.²⁰ The extent of this correlation may be influenced by features that are difficult to quantify, like the size distribution of micelles and the ionic strength of the aggregating samples. Thus, an increase of [A]* with increasing total dyestuff concentration is not necessarily incompatible with the concept of micellization. In the case of the present dyestuff aggregation, there are two strong arguments for assuming an equilibrium between monomers and micelle like aggregates at $t < T$ in terms of the Lomakin model.¹² First, it accounts for the bimodal particle distribution found in salt-free mixed RD and

YD solutions. Furthermore, it succeeds in explaining in a consistent way a fast nucleation during a short initial period where micelles are turned into nuclei.

By the present light-scattering experiments, we have illustrated that also the higher homologues of Mg^{2+} induce comparable dyestuff aggregation. These results give way to SAXS experiments since aggregates containing Sr^{2+} or Ba^{2+} are expected to provide a much better X-ray scattering contrast than Mg^{2+} does. The following subsection will present the results from SAXS measurements that shall reveal further details of the aggregation of RD and YD in the presence of alkaline earth cations.

Results from SAXS. In the present work, each dyestuff aggregation process is initiated by combining an aqueous solution of mixed RD and YD with an aqueous solution of alkaline earth chloride. We start by discussing the SAXS of these precursor solutions since they are important reference systems for dyestuff aggregation experiments. Figure 3 illustrates the scattering of precursor solutions.

Four differently concentrated solutions of RD and YD where the molar ratio of the two dyes was always 1:1 have been measured at a low sample-to-detector distance of 1 m. The results shown in Figure 3A shall be compared with a former

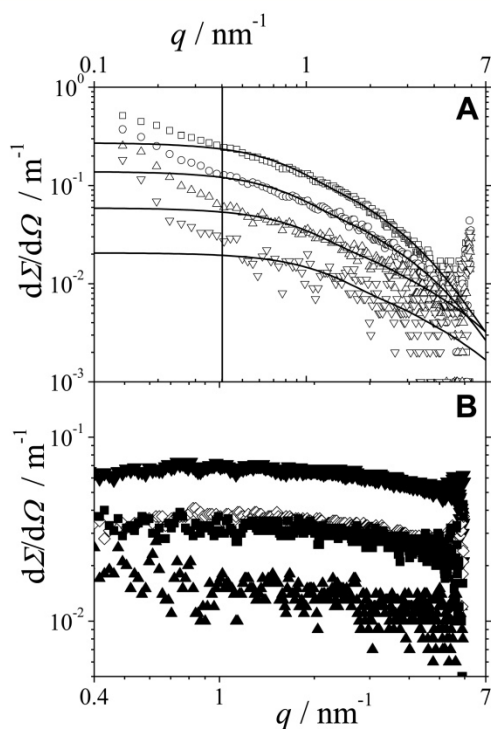


Figure 3. (A) SAXS of aqueous mixed dyestuff solutions without alkaline earth ions being present. The scattering of water has been subtracted. The molar ratio of RD and YD is 1:1 in all cases. The symbols indicate the following total dyestuff concentrations: 0.66 g L^{-1} (\square); 0.33 g L^{-1} (\circ); 0.17 g L^{-1} (\triangle); 0.08 g L^{-1} (∇). Continuous lines represent fitted cylinder model intensities (eq SI-2). For these fits, data points to the left-hand side of the vertical line ($q < 0.4 \text{ nm}^{-1}$) were discarded. (B) SAXS of alkaline earth chloride solutions in logarithmic representation. The scattering of water has been subtracted. The symbols indicate 3.25 mM BaCl_2 (\blacktriangledown); 1.63 mM BaCl_2 (\blacksquare); 0.81 mM BaCl_2 (\blacktriangle); 3.25 mM SrCl_2 (\diamond).

light-scattering study⁴ which characterized mixed RD and YD solutions as bimodal systems. The two diffusive modes found by dynamic light scattering were interpreted in terms of two populations: a mixture of monomers and small oligomers with hydrodynamic radii up to 10 nm coexisting with a larger, possibly micellar dyestuff species with hydrodynamic radii of about 50 nm. The latter is not fully captured by the SAXS data represented in Figure 3A since its Guinier regime appears at $q < 0.1 \text{ nm}^{-1}$; however, the existence of particles with a size of more than 20 nm becomes discernible by the upturn of the curves at $q < 0.4 \text{ nm}^{-1}$. The regime at $q > 0.4 \text{ nm}^{-1}$ though can be satisfactorily reproduced by cylinder model curves (eq SI-2 in the Supporting Information) with lengths of about 5 nm and thicknesses of less than one nanometer (cf. Table 2 and Figure

Table 2. Results from Fitting Cylinder Form Factors¹⁴ to Scattering Curves of Mixed RD and YD Dyestuff Solutions^a

dye concn/ g L^{-1}	0.66	0.33	0.17	0.08
cylinder length/ nm	5.69 ± 0.55	5.55 ± 0.61	4.70 ± 0.63	3.60 ± 0.86
cylinder radius/nm	0.46 ± 0.05	0.37 ± 0.04	0.20 ± 0.08	0.17 ± 0.09

^aThe corresponding fits are shown in Figure 3A and refer to the regime at $q > 0.4 \text{ nm}^{-1}$ only.

S3 in the Supporting Information). These values are in good agreement with the faster of the two diffusive modes found by dynamic light scattering in the preceding study.⁴ Thereby, the present SAXS measurements do not only confirm the bimodal character of pure mixed RD and YD solutions but they also reveal more detailed information on the smaller dyestuff species within the bimodal system, which according to the fits shown in Figure 3A consist of elongated, possibly cylindrical dyestuff oligomers.

The excess scattering of pure dissolved alkaline earth chlorides is depicted in Figure 3B. As expected, the very short-ranged spatial correlations between the ions hardly cause any q -dependency and the scattering increases with the concentration (shown for the case of BaCl_2). Also, dissolved SrCl_2 scatters weaker than dissolved BaCl_2 .

The combined SAXS of a solution of stoichiometrically mixed RD and YD and a solution of barium chloride can be considered as a reference representing the scattering of the solutes (RD+YD, BaCl_2) before they undergo alkaline earth induced aggregation. This combined SAXS of two precursor solutions is compared with the SAXS of the corresponding combined solution in which alkaline earth induced dyestuff aggregation takes place in Figure 4. The scattering at low q as expected increases drastically after initiation, which indicates a fast growth of large dyestuff aggregates. Notably, the scattering of the aggregating solution recorded earliest after initiation (\circ) at $q < 0.5 \text{ nm}^{-1}$ is already an order of magnitude larger than the reference scattering. At high q , any scattering curve independently of whether it represents a state before (\bullet), shortly after (\circ), or long after (\square) initiation drops to the same level, indicating the crossover to a time-independent background scattering. This background scattering can be mainly attributed to freely dissolved Cl^- and Na^+ ions as well as to those Ba^{2+} ions that are not involved into the dyestuff aggregation. For the following interpretation of the SAXS

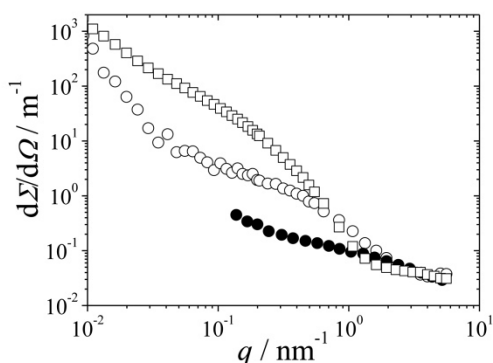


Figure 4. SAXS curves of a solution containing 0.33 g L^{-1} RD and YD (molar ratio = 1:1) and 1.6 mM BaCl_2 recorded at detector distances of 1, 5, and 10 m at times $t = 55 \text{ ms}$ (\circ) and $t = 5.5 \text{ s}$ (\square) after mixing the two corresponding precursor solutions. The linear combination of the SAXS curves from a 1.6 mM BaCl_2 solution and a mixed RD and YD solution at 0.33 g L^{-1} and a molar ratio of RD:YD = 1:1 recorded at 1 m detector distance (\bullet) is shown as a reference. The scattering of water was subtracted as solvent background from each curve shown.

data with the cylinder model,¹⁴ we took this background into account by means of the parameter bg in eq SI-2.

Figure 5A illustrates a set of time-resolved scattering curves in comparison to fitted cylinder model¹⁴ curves. The experimental curves exhibit three characteristic regimes: (i) A regime with strong q dependency at high q , (ii) a regime ranging from $q \approx 0.04 \text{ nm}^{-1}$ up to $q \approx 0.5 \text{ nm}^{-1}$ where the curves exhibit a q^{-1} dependency, and (iii) a regime at $q < 0.04 \text{ nm}^{-1}$ where the q dependency again increases. The upper q limit of regime (ii) depends on the time. As indicated in Figure 5A, regimes (i) and (ii) of the experimental data can be adequately reproduced with cylinder model curves (eq SI-2). Solely the upturn of the scattering intensity toward low q deviates considerably from the cylinder model.

From preceding work,^{2–5} we know that the dyestuff system under consideration forms wormlike aggregates. Such aggregates indeed cause a q^{-1} dependence which for long enough contour lengths turns into a q^{-2} dependence of the scattering intensity at low q and thus could at least partially explain the increasing q dependence of the scattering at $q < 0.04 \text{ nm}^{-1}$.^{21,22} Unfortunately, the lack of a Guinier regime prevents us from gaining information on contour lengths. Moreover, even wormlike chain form factors are not capable of accurately reproducing the strong q dependence of the scattering intensity at low q . However, a fast formation of a large network of wormlike chains is capable of explaining both the strong q dependence at low q and the lack of a Guinier regime. Network formation is likely to occur in the light of the dyestuff concentration used for the present SAXS experiments, which is 10 times higher than for the preceding light-scattering experiments.^{2–5}

On a small enough length scale, isolated wormlike chains as well as networks thereof are characterized by elongated, locally rigid substructures. The existence of such substructures is clearly indicated by the good agreement of cylinder model curves with the experimental data at $q > 0.04 \text{ nm}^{-1}$ (Figure 5A). The model curves were calculated by means of eq SI-2. For all fits, data points at $q < 0.05 \text{ nm}^{-1}$ were disregarded and the cylinder length was fixed at $L = 200 \text{ nm}$. This value suffices to nicely reproduce the q^{-1} dependence of the SAXS curves and is

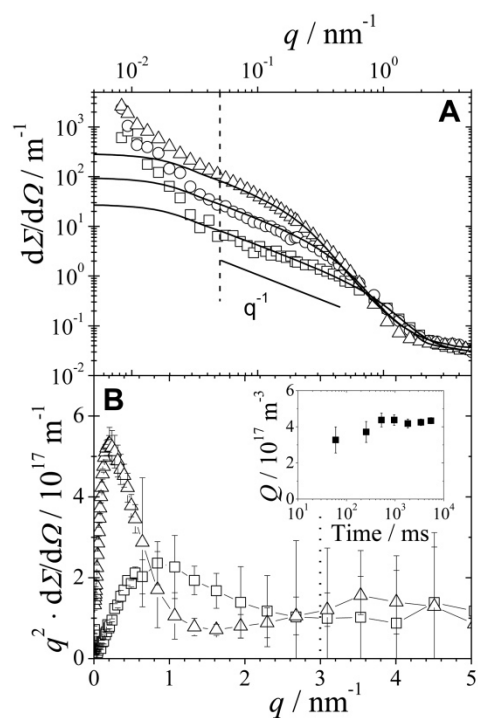


Figure 5. Scattering curves of a sample containing 1.6 mM BaCl_2 and 0.33 g L^{-1} dyestuff at a molar ratio of RD:YD = 1:1 as double logarithmic plots (A) and as Kratky plots (B). The symbols denote increasing times after initiation of the aggregation (\square , 60 ms; \circ , 255 ms; \triangle , 5.46 s). Continuous lines represent fits with the cylinder model (eq SI-2) with a constant cylinder length of $L = 200 \text{ nm}$ and a constant polydispersity of the cross section of $\sigma/R = 0.4$. The best fit was obtained by adjusting the radius of gyration of the cylinder cross section ($R_{g,cs}$), the background scattering (bg), and the scale (I_0), respectively. Data points to the left of the dashed line in (A) were disregarded during fitting. For the calculation of the Kratky representations in (B), the background scattering bg established by the corresponding fit was subtracted from each original curve, respectively. The dotted line in (B) represents the upper q limit for the calculation of the invariant Q (eq 10). The time dependency of Q is shown in the inset.

in line with the persistence lengths of approximately 200 nm that were obtained from an interpretation of previously measured light-scattering data^{3,5} with the wormlike chain model.^{21,22}

Two features of the scattering intensity at $q > 0.04 \text{ nm}^{-1}$ change with time. First, the shoulder that interconnects the q^{-1} -dependent regime with the steeper regime at high q is shifted toward lower q . The cylinder model¹⁴ accommodates this by a thickening of the cylinder cross section. Second, the intensity of the q^{-1} -dependent regime increases significantly. The increase can be quantified by a bended rod plot. This is established by multiplying the scattering intensity with q , which turns the q^{-1} -dependent regime into a plateau. The resulting plateau value is proportional to the total mass concentration c and to the molar mass per unit length M_L of the rigid, elongated substructures:^{23,24}

$$q \frac{d\Sigma}{d\Omega}(q) \Big|_{\text{plateau}} = k_2 c M_L \quad (17)$$

In eq 17, k_2 is a constant that depends on the scattering contrast of the aggregates. In a model system of laterally growing cylinders of constant length, both M_L and c are proportional to the cylinder cross section R^2 , which yields $cM_L \sim R^4$. This theoretical correlation is compared with the experimentally found correlation of the plateau value k_2cM_L and the cylinder radius R in Figure 6 for several differently

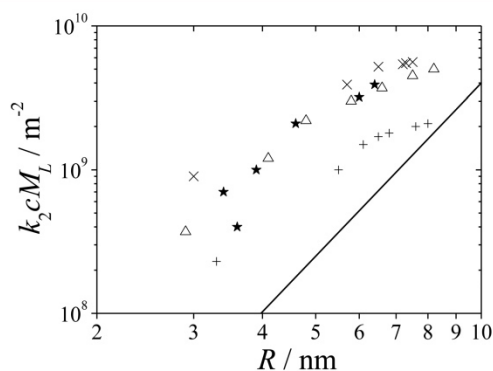


Figure 6. Correlations of the plateau values k_2cM_L and the cross section radii R for various samples. All samples contain RD and YD in a molar ratio of 1:1. Values of k_2cM_L were obtained by means of eq 17, whereas values of R were obtained from fitting cylinder model curves (eq SI-2) to the experimental data. The symbols denote the following concentrations: $[\text{Ba}^{2+}] = 1.6 \text{ mM}$, $c_{\text{RY}} = 0.33 \text{ g L}^{-1}$ (Δ); $[\text{Ba}^{2+}] = 3.2 \text{ mM}$, $c_{\text{RY}} = 0.33 \text{ g L}^{-1}$ (\times); $[\text{Ba}^{2+}] = 3.2 \text{ mM}$, $c_{\text{RY}} = 0.11 \text{ g L}^{-1}$ ($+$); $[\text{Sr}^{2+}] = 3.2 \text{ mM}$, $c_{\text{RY}} = 0.33 \text{ g L}^{-1}$ (\star). The continuous line illustrates a correlation of $k_2cM_L \sim R^4$.

concentrated samples. In all cases, R increases by a factor of 2–3 during the first 3 s after initiation, whereas k_2cM_L increases roughly 20-fold. Due to the large uncertainty of radii $< 5 \text{ nm}$, a correlation of $cM_L \sim R^4$ signifying a lateral fiber growth in this regime can neither be fully confirmed nor excluded. Yet, the data points at $R > 5 \text{ nm}$, where accuracy is much higher, denote a significant flattening of the correlation for all samples, which is not compatible with a lateral growth of single fibers anymore. A physically meaningful explanation for this finding is illustrated in Figure 7. When the longitudinal growth of single fibers by the addition of small building units is matured, the mass concentration of aggregates remains constant, which turns the contribution of c in the correlation between cM_L and R into a constant factor. The view of a complete consumption of building units in the regime of $R > 5 \text{ nm}$ is supported by the finding that the plateau values of the Ba^{2+} -based aggregates in Figure 6 correlate with the dyestuff concentration. However, mature fibers may now increasingly engage in partial lateral alignment leading to cross-linking of the dyestuff fibers. This partial lateral alignment would also cause an increase of R and of M_L averaged along the contour, and it is in line with TEM images presented in the preceding study.⁵ Branching and network formation in aggregating systems is an interesting phenomenon on its own and an aspect highly relevant for biological processes like for instance the formation of fibrin networks during blood clotting or the cross-linking of actin in the cytoskeleton.²⁵ In comparison with chemical polymerization, where branching is usually induced by incorporation of multifunctional monomers into the polymer chains, the mechanisms of branching in self-assembly processes are by far less well understood and much more diverse. To give but a

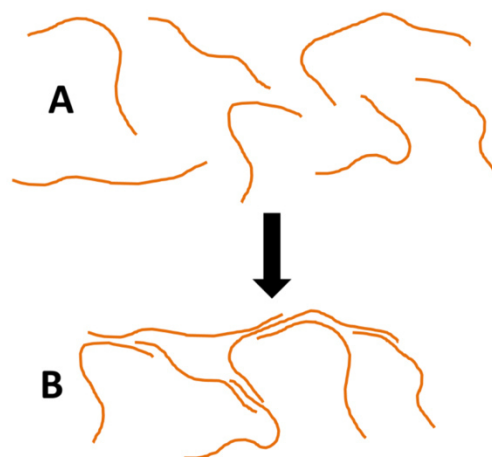


Figure 7. A fiber network (B) is formed from free, full-grown fibers (A). The network formation proceeds at constant mass concentration, but causes an increase of the averaged radius of locally rigid cylindrical segments as well as of their averaged mass per unit length.

few examples, the polymerization of fibrin²⁶ and the network formation of nonionic surfactants in water²⁷ and of dibenzylidene sorbitol in poly(propylene oxide) matrices²⁸ are based on different mechanisms.

In Figure 5B, Kratky plots of the first and the last scattering curve from Figure 5A are presented. According to eq 10, the area under a Kratky plot corresponds to the Porod invariant¹³ Q , which is proportional to the volume fraction of dyestuff aggregates in the respective sample. The high q limit used to calculate Q is located in a regime where the curves approach the q axis within experimental uncertainty. Considering all data points up to $q = 3 \text{ nm}^{-1}$ as denoted by the dotted line in Figure 5B results in an invariant that is independent of the time (inlet of Figure 5B). Time independence indicates that all species involved in structural reorganizations are captured by this invariant at any time. However, the shift of the Kratky plot toward lower q with time clearly indicates a continuous structural reorganization including the incorporation of smaller dyestuff particles into larger ones. This is in agreement with a longitudinal fiber growth by stepwise addition of small building units as identified in preceding work^{2–5} as well as with a network formation caused by partial lateral attachment of full-grown fibers as indicated by the present correlation of cM_L versus R . Yet, the present Kratky plots do not permit to define a q value by which building units could be clearly separated from larger, growing structures. Hence the plots suggest that the supposed oligomeric building units exhibit sizes comparable to or slightly larger than the cross sections of the growing structures. As illustrated in the Supporting Information (Figure S4), a possible impact of the building units on the fitted cylinder radius R is negligible.

The application of eq 17 to static light-scattering data of dyestuff aggregates that had grown in the presence of Ba^{2+} ions yielded a value of $M_L \approx 10^5 \text{ g mol}^{-1} \text{ nm}^{-1}$ at complete conversion. With the radius of the cross section of a mature dyestuff aggregate ($R \approx 5 \text{ nm}$) as a result from the SAXS data under present consideration, we can now estimate the average volume V_{RY} that a dyestuff dimer RD-YD would have to adopt in order to achieve this M_L value. The resulting value of $V_{\text{RY}} \approx 1 \text{ nm}^3$ represents a physically meaningful regime for the volume

of RD and YD and thereby emphasizes the coherence between the results from light scattering and SAXS.

Results from ASAXS. Two samples were investigated with ASAXS using three different photon energies. Since the recording of SAXS data at three different photon energies is time consuming, the samples had to be temporally stable. This prerequisite was achieved by generating dyestuff gels which extended over the bottom part of the scattering cell beneath a well-defined colorless supernatant (see Experimental Section). The results from ASAXS experiments shall be discussed in terms of two aspects. First, the SAXS of the dyestuff gels will be compared with the SAXS of dilute solutions. Afterward, the ratio of Sr^{2+} per RD and YD within the aggregates will be estimated.

A comparison of the scattering from the gels used for ASAXS experiments (Figure 8A) with the previously discussed time-resolved SAXS curves (Figure 5A) reveals the following features (see Figure S7 in the Supporting Information for a direct comparison). (i) The SAXS from a gel is about 2 orders of magnitude larger than the final SAXS from a dilute,

homogeneous sample used for time-resolved SAXS measurements, which can be clearly attributed to the large difference of the sample concentrations: the estimated dyestuff concentrations in the gels (see Table 3) are more than 30 times larger

Table 3. Results from ASAXS and X-ray Absorption Measurements^a

	Average Concentrations	
$[\text{Sr}^{2+}]/\text{mM}$	6.5	13.0
$c_{\text{dye-b}}/\text{g L}^{-1}$	0.66	0.66
	Results from XANES	
$[\text{Sr}^{2+}]_{\text{t}}/\text{mM}$	05.9 ± 0.5	12.6 ± 0.6
$[\text{Sr}^{2+}]_{\text{b}}/\text{mM}$	15.7 ± 0.8	19.9 ± 0.9
$c_{\text{dye-b}}/\text{g L}^{-1}$	11.3 ± 1.3	12.7 ± 1.3
$[\text{dye charges}]_{\text{b}}/\text{mM}$	36.2 ± 4.1	40.6 ± 4.2
	Results from ASAXS	
$[\text{Sr}^{2+}]_{\text{spec}}/\text{mM}$	13.7 ± 2.4	16.3 ± 3.2
	Ratio	
$[\text{Sr}^{2+}]_{\text{spec}}/[\text{dye charges}]_{\text{b}}$	0.38 ± 0.07	0.40 ± 0.09

^aIndices “t” and “b” denote values, respectively, at the top and at the bottom of the capillary. $[\text{Sr}^{2+}]_{\text{spec}}$ denotes the concentration of strontium ions that are specifically bound to dyestuff aggregates within the dyestuff gel at the bottom position. The route that was followed to obtain the values is outlined in detail in the Supporting Information.

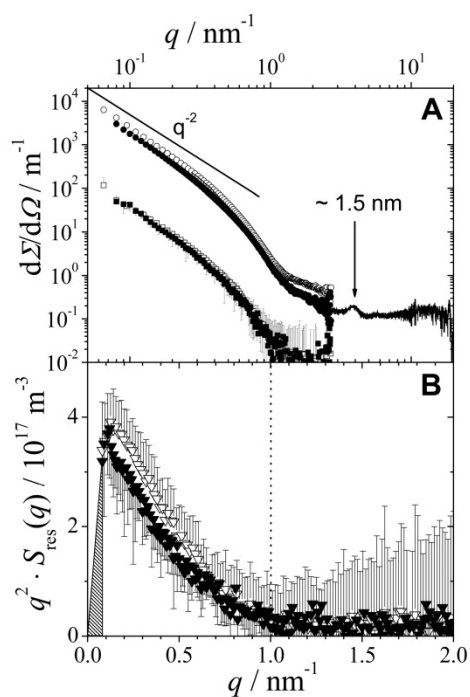


Figure 8. ASAXS measurements of two samples, which contain the same total dyestuff concentration of 0.66 g L^{-1} in a molar ratio of RD:YD = 1:1 but differ in their average concentration of Sr^{2+} ions. Open symbols denote the sample containing 13 mM Sr^{2+} , whereas filled symbols correspond to the sample containing 6.5 mM Sr^{2+} . (A) Total scattering curves recorded at the lowest photon energy $E_1 = 15\,500 \text{ eV}$ (\circ, \bullet) where the scattering of water has been subtracted in comparison with the pure resonant scattering (\square, \blacksquare) calculated by means of eq 12. The scattering of the sample with $[\text{Sr}^{2+}] = 6.5 \text{ mM}$ has additionally been recorded at higher angles, which is illustrated by the continuous line at $q > 3 \text{ nm}^{-1}$. (B) Kratky representations ($\nabla, \blacktriangledown$) of the two pure resonant scattering curves shown in (A). The areas under the curves correspond to the resonant invariants Q_{res} (eq 13). The shaded triangle illustrates the approximation of Q_{res} at low q , whereas the dotted line denotes the high q limit for the calculation of Q_{res} .

than the dyestuff concentration used for time-resolved SAXS. (ii) The scattering curves from gels and from dilute solutions behave similarly at $q > 0.5 \text{ nm}^{-1}$. This indicates that the aggregate structures in gels resemble the ones in dilute solutions on a length scale $< 10 \text{ nm}$, including any structural features on the level of fiber cross sections or below. Contrarily, at $q < 0.5 \text{ nm}^{-1}$ the distinct q^{-1} dependency of scattering curves from dilute solutions gives way to a q^{-2} dependency in the case of the gels. This decrease in decay from a q^{-1} dependence to a q^{-2} dependence suggests a considerable increase of the density of cross-links based on the partial alignment of matured dyestuff fibers, which is in line with the macroscopically observed gelation. (iii) The SAXS curve of the gel sample containing 6.5 mM Sr^{2+} , which was extended toward high q by using the shortest possible sample-to-detector distance, reveals a significant peak at $q \approx 4 \text{ nm}^{-1}$. This peak corresponds to a correlation length of approximately 1.5 nm between Sr^{2+} ions. Evidently, such a spatial correlation is a result of the aggregation process, thereby indicating a distinct degree of order within the aggregates.

The resonant scattering curves $S_{\text{res}}(q)$ of the two samples used for ASAXS were calculated by means of eq 12. They represent the scattering contributions which stem solely from strontium ions. As illustrated in Figure 8A, these contributions are about 2 orders of magnitude smaller than the total scattering. Remarkably, the total scattering and the resonant scattering contribution exhibit a similar q dependency, indicating that the strontium ions are evenly distributed along the dyestuff aggregates.

For each sample, the resonant invariant Q_{res} was calculated according to eq 13 as the area under the Kratky plot of the respective pure resonant contribution shown in Figure 8B. Thereby the low- q regime where no experimental data is available was approximated as a triangle, respectively. Such an approximation is justified since both Kratky plots pass a maximum at small q . The concentrations of strontium ions that are specifically bound to the dyestuff gel were estimated by

means of eq 14 for both samples. At the same time, the total concentrations of strontium ions at the top (colorless supernatant) and the bottom (gel) position of the sample capillaries were estimated by means of X-ray absorption spectra, respectively (for details, see the Supporting Information). The results are summarized in Table 3 and provide the following important features which hold for both samples, respectively. The Sr^{2+} concentrations measured in the colorless phase and in the gel phase, $[\text{Sr}^{2+}]_t$ and $[\text{Sr}^{2+}]_b$, adopt values below and above the average (weighed) Sr^{2+} concentrations denoted as $[\text{Sr}^{2+}]$, respectively. The finding of $[\text{Sr}^{2+}]_t < [\text{Sr}^{2+}] < [\text{Sr}^{2+}]_b$ verifies the significance of the X-ray absorption measurements for the determination of Sr^{2+} concentrations. Moreover, $[\text{Sr}^{2+}]_t$ is much closer to $[\text{Sr}^{2+}]$ than $[\text{Sr}^{2+}]_b$, which is in line with the macroscopic observation that the colorless phases occupy much larger volumes than the gel phases. The concentrations of specifically interacting strontium ions are slightly smaller but still very close to the absolute Sr^{2+} concentrations within the gel phases ($[\text{Sr}^{2+}]_{\text{spec}}/[\text{Sr}^{2+}]_b > 0.8$ for both samples). This indicates that the major part of strontium ions within the gel phase is involved in the dyestuff aggregation.

By knowing $[\text{Sr}^{2+}]_t$ and $[\text{Sr}^{2+}]_b$, the dyestuff concentration within the gel can be estimated (see the Supporting Information) and compared to $[\text{Sr}^{2+}]_{\text{spec}}$ resulting in a ratio of about 0.4 specifically bound strontium ions per anionic dyestuff charge. This proves that, within experimental uncertainty, anionic dyestuff charges can be considered to be entirely neutralized by the strontium ions.

SUMMARY

In several preceding studies,^{2–5} we thoroughly investigated the coaggregation of RD and YD in the presence of Mg^{2+} ions. The present work illustrates that an addition of Ca^{2+} , Sr^{2+} , or Ba^{2+} ions to an aqueous solution of stoichiometrically mixed RD and YD, similarly to the addition of Mg^{2+} ions, induces an aggregation to fiberlike particles. The interpretation of time-dependent molar mass data with the Lomakin model¹² indicated that the dyestuff aggregation is initiated by a short period of fast nucleation followed by an extended growth period during which long fiberlike dyestuff aggregates are formed by the stepwise addition of small building units. This holds independently of the type of alkaline earth cation used and is closely related to the pattern observed in the case of Mg^{2+} . However, the type and concentration of the alkaline earth cation have a strong impact on the rate of fiber growth. Both of these aspects reconfirm a strong involvement of the alkaline earth cations into the activation of chain ends and/or building units.

The proof of an aggregation induced by the use of heavy ions like Sr^{2+} and Ba^{2+} gave way to investigate the dyestuff aggregation by means of small-angle X-ray scattering. First, the SAXS of pure (salt free) mixed RD and YD solutions was measured as a reference. These curves are in line with a bimodal particle distribution as it has already been established by a preceding light-scattering study⁴ and furthermore enabled attribution of the smaller mode to rodlike dyestuff oligomers with lengths of less than 10 nm. The time-resolved SAXS of samples in which fiber formation was respectively induced by an addition of Sr^{2+} or Ba^{2+} was initially intended to reveal direct information on the nucleation period. This aim could not be achieved since even the earliest recorded curves already indicated the presence of fiber like structures with lengths of more than 200 nm, which again emphasizes an exceptionally

fast rate of nucleation. Instead, the SAXS experiments revealed an interesting mechanistic aspect of the later stages of the aggregation. Its correlation with the product of mass concentration and mass per unit length of the fibers indicates that the growth of the averaged fiber cross section results from a partial lateral alignment of mature fibers. At the same time, this correlation excludes a branching of still longitudinally growing fibers as another thinkable mechanism for network formation.

Finally, the ratio of Sr^{2+} ions per RD–YD unit within the dyestuff aggregates was estimated by additional ASAXS experiments. The results denote that anionic dyestuff charges are neutralized by alkaline earth cations in the course of the self-assembly process. Furthermore, a homogeneous distribution of Sr^{2+} ions within the dyestuff aggregates as well as a characteristic distance of approximately 1.5 nm between Sr^{2+} ions could be identified.

ASSOCIATED CONTENT

Supporting Information

Reproducibility of aggregation experiments; modeling of small-angle scattering data by means of the cylinder model; cylinder radii obtained from Guinier fits; parameter distortion based on an interpretation of the scattering of a mixture of small and large cylinders by means of the form factors of large cylinders; estimation of the dyestuff concentration within centrifuged dyestuff gels; calculation of Sr^{2+} concentrations from X-ray absorption spectra; direct comparison of the SAXS from samples used for SAXS and ASAXS experiments. This material is available free of charge via the Internet at <http://pubs.acs.org>.

AUTHOR INFORMATION

Corresponding Author

*E-mail: klaus.huber@upb.de. Phone: +49 5251 602125.

Notes

The authors declare no competing financial interest.

ACKNOWLEDGMENTS

The time-resolved SAXS experiments reported within the present article were performed on the ID02 beamline at the European Synchrotron Radiation Facility (ESRF), Grenoble, France. We are grateful to Theyencheri Narayanan, Peter Boesecke, and Michael Sztucki at ESRF for providing assistance in using beamline ID02. ASAXS measurements reported within the present article were carried out at the light source DORIS III at DESY, a member of the Helmholtz Association (HGF). We thank the staff at beamline B1 (former JUSIFA) for assistance in performing the experiments.

REFERENCES

- (1) Imae, T.; Gagel, L.; Tunich, C.; Platz, G.; Iwamoto, T.; Funayama, K. Formation of Supramolecular Fibril by Water-Soluble Azo Dye. *Langmuir* **1998**, *14*, 2197–2200.
- (2) Escudero Inglés, S.; Katzenstein, A.; Schlenker, W.; Huber, K. Time-Resolved Recording of Ionic Dyestuff Aggregation by Static Light Scattering. *Langmuir* **2000**, *16*, 3010–3018.
- (3) Katzenstein, A.; Huber, K. Model of Polydisperse Wormlike Stars and Its Application to Dyestuff Aggregates. *Langmuir* **2002**, *18*, 7049–7056.
- (4) Michels, R.; Sinemus, T.; Hofmann, J.; Brutschy, B.; Huber, K. Co-Aggregation of Two Anionic Azo Dyestuffs at a Well-Defined Stoichiometry. *J. Phys. Chem. B* **2013**, *117*, 8611–8619.

- (5) Michels, R.; Hertle, Y.; Hellweg, T.; Huber, K. Kinetic and Structural Features of a Dyestuff Co-Aggregation Studied by Time-Resolved Static Light Scattering. *J. Phys. Chem. B* **2013**, *117*, 15165–15175.
- (6) Becker, A.; Schmidt, M. Time-Resolved Static Light Scattering: New Possibilities in Polymer Characterization. *Macromol. Chem. Macromol. Symp.* **1991**, *50*, 249–260.
- (7) Panine, P.; Finet, S.; Weiss, T. M.; Narayanan, T. Probing Fast Kinetics in Complex Fluids by Combined Rapid Mixing and Small-Angle X-Ray Scattering. *Adv. Colloid Interface Sci.* **2006**, *127*, 9–18.
- (8) Zimm, B. The Scattering of Light and the Radial Distribution Function of High Polymer Solutions. *J. Chem. Phys.* **1948**, *16*, 1093–1099.
- (9) Zimm, B. Apparatus and Methods for Measurement and Interpretation of the Angular Variation of Light Scattering; Preliminary Results on Polystyrene Solutions. *J. Chem. Phys.* **1948**, *16*, 1099–1116.
- (10) Witte, T.; Haller, L. A.; Luttmann, E.; Krüger, J.; Fels, G.; Huber, K. Time Resolved Structure Analysis of Growing β -Amyloid Fibers. *J. Struct. Biol.* **2007**, *159*, 71–81.
- (11) Lages, S.; Michels, R.; Huber, K. Coil-Collapse and Coil-Aggregation due to the Interaction of Cu^{2+} and Ca^{2+} Ions with Anionic Polyacrylate Chains in Dilute Solution. *Macromolecules* **2010**, *43*, 3027–3035.
- (12) Lomakin, A.; Teplow, D. B.; Kirschner, D. A.; Benedek, G. B. Kinetic Theory of Fibrillogenesis of Amyloid Beta Protein. *Proc. Natl. Acad. Sci. U.S.A.* **1997**, *94*, 7942–7947.
- (13) Porod, G. Die Röntgenkleinwinkelstreuung von dichtgepackten kolloiden Systemen. *Kolloid Z.* **1951**, *124*, 83–114.
- (14) Guinier, A.; Fournet, G. *Small-Angle Scattering of X-Rays*; John Wiley and Sons: New York, 1955.
- (15) Goerigk, G. The Impact of the Turing Number on Quantitative ASAXS Measurements of Ternary Alloys. *JOM* **2013**, *65*, 44–53.
- (16) Goerigk, G. The Solution of the Eigenvector Problem in Synchrotron Radiation Based Anomalous Small-Angle X-Ray Scattering. *ALAMT* **2013**, *3*, 59–68.
- (17) Goerigk, G.; Huber, K.; Schweins, R. Probing the Extent of the Sr^{2+} Ion Condensation to Anionic Polyacrylate Coils: A Quantitative Anomalous Small-Angle X-Ray Scattering Study. *J. Chem. Phys.* **2007**, *127*, 154908.
- (18) Shannon, R. D. Revised Effective Ionic Radii and Systematic Studies of Interatomic Distances in Halides and Chalcogenides. *Acta Crystallogr.* **1976**, *A32*, 751–767.
- (19) Deublein, S.; Reiser, S.; Vrabec, J.; Hasse, H. A Set of Molecular Models for Alkaline-Earth Cations in Aqueous Solution. *J. Phys. Chem. B* **2012**, *116*, 5448–5457.
- (20) Tanford, C. Theory of Micelle Formation in Aqueous Solutions. *J. Phys. Chem.* **1974**, *78*, 2469–2479.
- (21) Kratky, O.; Porod, G. Röntgenuntersuchung gelöster Fadenmoleküle. *Recl. Trav. Chim.* **1949**, *68*, 1106–1123.
- (22) Pedersen, J. S.; Schurtenberger, P. Scattering Functions of Semiflexible Polymers with and without Excluded Volume Effects. *Macromolecules* **1996**, *29*, 7602–7612.
- (23) Hotzer, A. Interpretation of the Angular Distribution of the Light Scattered by a Polydisperse System of Rods. *J. Polym. Sci.* **1955**, *17*, 432–434.
- (24) Denking, P.; Burchard, W. Determination of Chain Stiffness and Polydispersity from Light Scattering. *J. Polym. Sci., Part B* **1991**, *29*, 589–600.
- (25) Bretscher, A. Microfilament Structure and Function in the Cortical Cytoskeleton. *Annu. Rev. Cell Biol.* **1991**, *7*, 337–374.
- (26) Bale, M. D.; Mosher, D. F. Effects of Thrombospondin on Fibrin Polymerization and Structure. *J. Biol. Chem.* **1986**, *261*, 862–868.
- (27) Bernheim-Groswasser, A.; Wachtel, E.; Talmon, Y. Micellar Growth, Network Formation, and Criticality in Aqueous Solutions of the Nonionic Surfactant C_{12}E_5 . *Langmuir* **2000**, *16*, 4131–4140.
- (28) Fahrlander, M.; Fuchs, K.; Friedrich, Chr. Rheological Properties of Dibenzylidene Sorbitol Networks in Poly(Propylene Oxide) Matrices. *J. Rheol.* **2000**, *44*, 1103–1119.

Coaggregation of Two Anionic Azo Dye-stuffs: A combined Static Light Scattering and X-Ray Scattering Study

Rolf Michels,[†] Günter Goerigk,[‡] Ulla Vainio,^{||} Jérémie Gummel,[§] and Klaus Huber^{*†}

[†]Universität Paderborn, Department für Physikalische Chemie, Warburger Straße 100, D-33098 Paderborn, Germany

[‡]Helmholtz-Zentrum Berlin, Institut Weiche Materie und Funktionale Materialien, Hahn-Meitner-Platz 1, D-14109 Berlin, Germany

^{||}Deutsches Elektronen-Synchrotron DESY, Notkestraße 85, D-22607 Hamburg, Germany

[§]Procter & Gamble Technical Centre, Whitley Road, Longbenton, Newcastle Upon Tyne, Tyne And Wear, NE12 9SR, United Kingdom

*to whom correspondence should be addressed

E-mail: klaus.huber@upb.de

Phone: +49 5251 602125

Supporting Information

SUPPORTING INFORMATION. Reproducibility of Aggregation Experiments; Modeling of Small-Angle Scattering Data by Means of the Cylinder Model; Cylinder Radii Obtained from Guinier Fits; Parameter Distortion Based on an Interpretation of the Scattering of a Mixture of Small and Large Cylinders by Means of the Form Factors of Large Cylinders; Estimation of the Dye-stuff Concentration within Centrifuged Dye-stuff Gels; Calculation of Sr^{2+} Concentrations from X-Ray Absorption Spectra; Direct Comparison of the SAXS from Samples Used for SAXS and ASAXS Experiments. This material is available free of charge via the Internet at <http://pubs.acs.org>.

Reproducibility of Aggregation Experiments

The reproducibility of dyestuff aggregation experiments is exemplified in Figures S1 and S2. Figure S1 demonstrates that an initiation by hand mixing and an initiation by using a stopped-flow device lead to growth processes that are not distinguishable from each other. In Figure S2, two features are demonstrated. First, different shots with the stopped-flow device lead to growth processes that are equal within the uncertainty of the SAXS data. Second, data sets that are recorded at equal times after initiation but at different sample-to-detector distances exhibit equal intensities within their overlapping q regime and thus can be merged without difficulty.

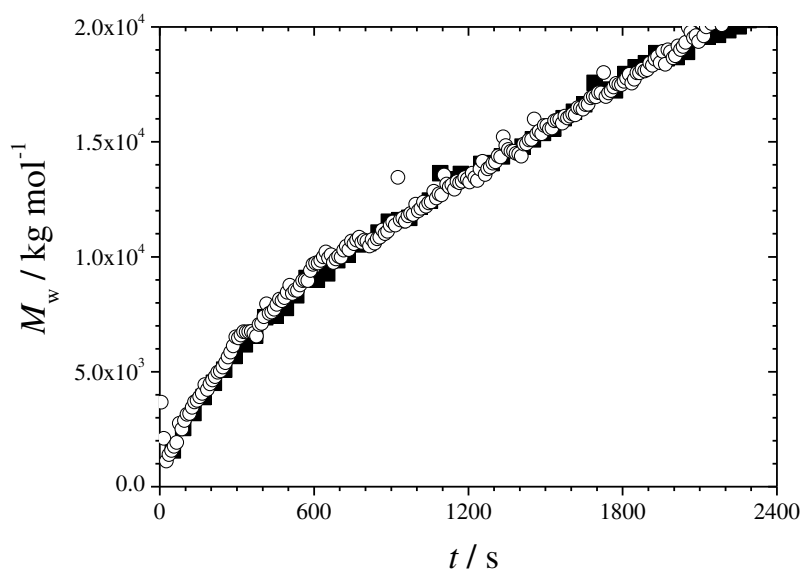


Figure S1. The evolution of the weight-averaged molar mass M_w is compared for two mixing cycles during which equal volumes of an aqueous magnesium chloride solution and an aqueous solution of RD and YD with a molar ratio of 1:1 were combined at time $t = 0$. Both mixing cycles resulted in a final dyestuff concentration of 0.066 g l^{-1} (0.042 mM) and a final Mg^{2+} concentration of 1.63 mM . Symbols (■) represent an experiment where the dyestuff aggregation has been initiated by hand mixing of the two components, whereas symbols (○) represent an experiment where the components were mixed by means of an SF-20 stopped-flow device.

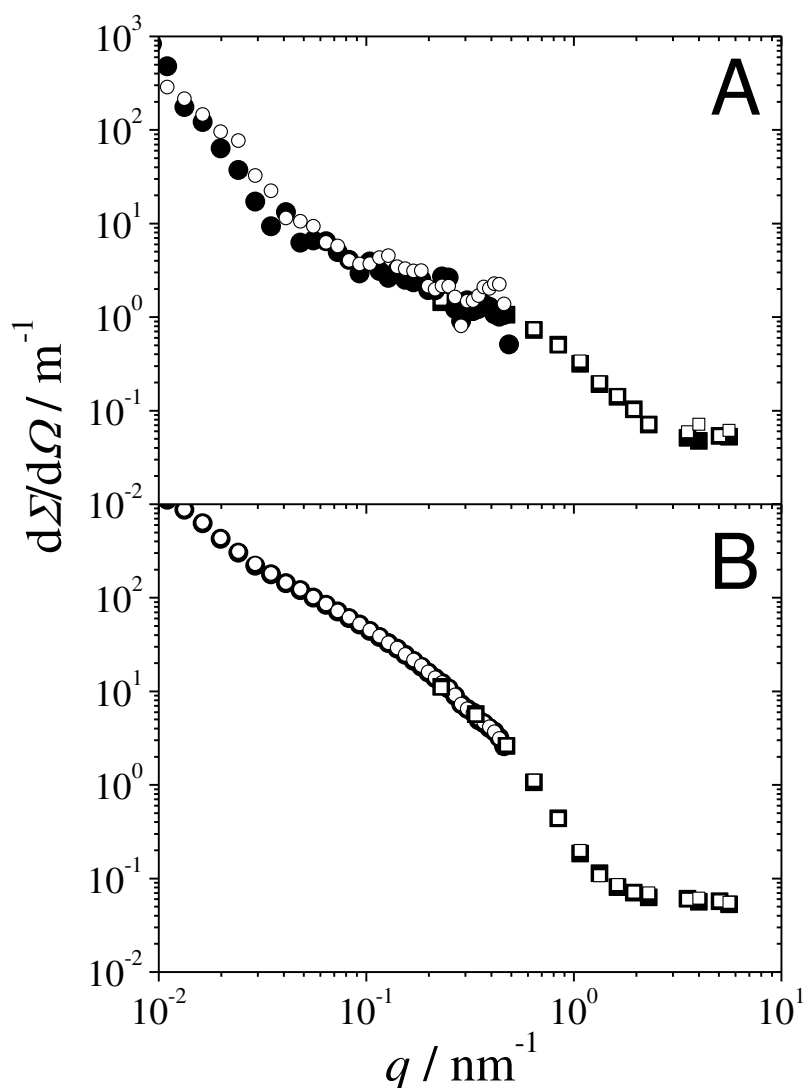


Figure S2. Scattering curves from shots with the SF-400 stopped flow device. All shots were performed with equal dyestuff and alkaline earth concentrations ($c_{\text{dye}} = 0.33 \text{ g l}^{-1}$, $[\text{Ba}^{2+}] = 1.6 \text{ mM}$) but at different detector distances of 1 m (symbols \square, \blacksquare) and of 10 m (symbols \circ, \bullet). Graph (A) shows scattering curves which were calculated by averaging three single curves recorded at $t = 25, 55$ and 85 ms , respectively, thus representing an averaged time after initiation of $t = 55 \text{ ms}$. Graph (B) shows scattering curves which were calculated by averaging 20 single curves recorded in between $t = 1,5 \text{ s}$ and $t = 2,1 \text{ s}$, respectively, thus representing an averaged time after initiation of $t = 1,8 \text{ s}$. The results illustrate (i) a good reproducibility of the shots achieved with the SF-400 stopped-flow instrument and (ii) justify the combination of time-resolved averaged scattering recorded at different detector distances.

Modeling of Small-Angle Scattering Data by Means of the Cylinder Model

The scattering from samples was interpreted by means of the cylinder model. The form factor of a homogeneous cylinder with length L and cross section radius R is given by¹:

$$P_{\text{cyl}}(q, L, R) = \frac{d\Sigma/d\Omega(q)_{\text{cyl}}}{d\Sigma/d\Omega(q=0)_{\text{cyl}}} = \int_0^{\pi/2} \left[\frac{2J_1(qR \sin(x))}{qR \sin(x)} \frac{\sin(qL \cos(x)/2)}{qL \cos(x)/2} \right]^2 \sin(x) dx \quad (\text{SI-1})$$

In the present work, we added a polydispersity to the cylinder cross-section in terms of a Gaussian distribution of the radius R' around its mean value R with absolute standard deviation σ and relative standard deviation σ/R . Moreover, a q independent background scattering was included into the model. Accordingly, model scattering intensities of cylinders with polydisperse cross-sections were calculated as

$$I_{\text{poly}}(q, L, R, \sigma) = \frac{I_0}{\sqrt{2\pi\sigma^2}} \int_{R'} \exp\left(-\frac{(R'-R)^2}{2\sigma^2}\right) P_{\text{cyl}}(q, L, R') dR' + bg \quad , \quad (\text{SI-2})$$

where I_0 represents the scattering intensity at zero momentum transfer and bg is the background scattering.

Cylinder Radii Obtained from Guinier Fits

The scattering intensity of cylindrical structures with length L and radius R is proportional to q^{-1} within the regime $qL > 1$ and $qR < 1$. This can be utilized to determine R by means of a Guinier¹ like approximation:

$$q \cdot \frac{d\Sigma}{d\Omega}(q) \Big|_{qR < 1} \approx A \cdot \exp\left(-\frac{q^2 R^2}{6}\right) \quad . \quad (\text{SI-3})$$

Besides modeling the experimental data with cylinder form factors (eq SI-2), eq SI-3 represents an alternative for the determination of R . As indicated in Figure S3-B, the values resulting for R from both of these alternative methods do not deviate significantly.

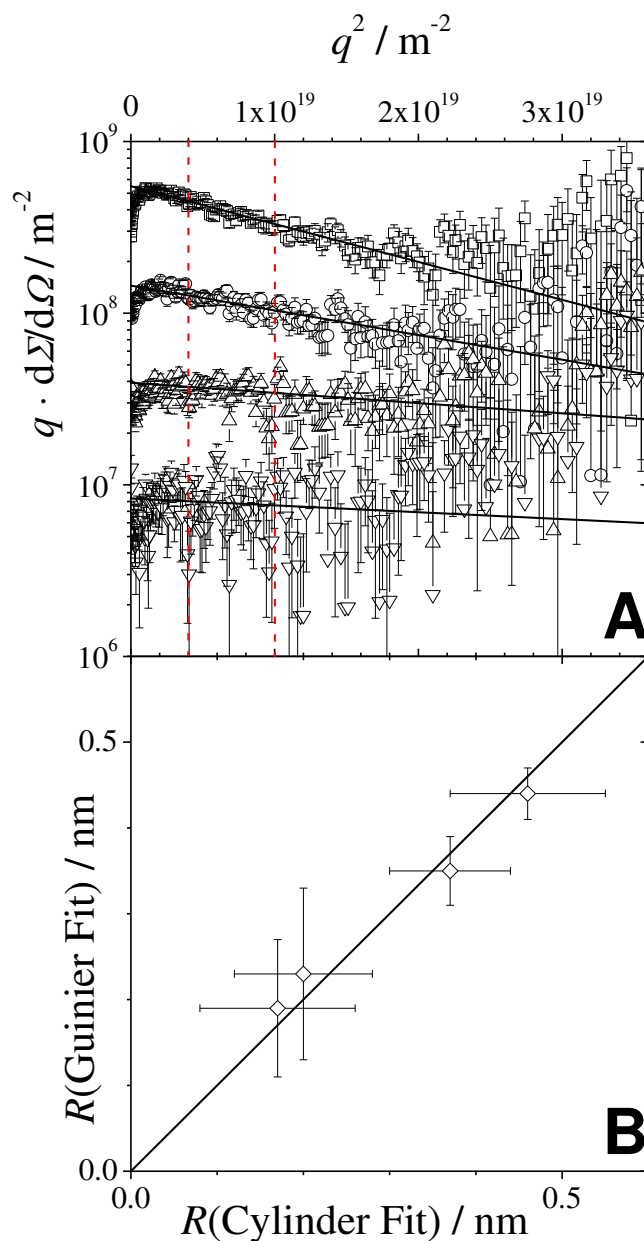


Figure S3. (A) Plots of the product of the scattering vector q with the SAXS of aqueous solutions containing 0.66 g l^{-1} (\square), 0.33 g l^{-1} (\circ), 0.17 g l^{-1} (\triangle) and 0.08 g l^{-1} (∇) mixed RD and YD in stoichiometric ratio (cf. Figure 3A in the manuscript). The continuous lines represent Guinier like fits according to eq SI-3. For these fits, only the q regime in between the red dashed lines was considered. For the sake of clarity, the curves are separated from each other by a factor of 2, respectively. (B) Comparison of the R values resulting from cylinder fits (eq SI-2, cf. Table 2 in the manuscript) with the R values resulting from Guinier like fits (eq SI-3).

Parameter Distortion Based on an Interpretation of the Scattering of a Mixture of Small and Large Cylinders by Means of the Form Factors of the Large Cylinders

The scattering of matured dyestuff fibres is modeled by means of form factors of cylinders with a length of $L = 200$ nm and variable scale (I_0) and radius (R). This interpretation does not consider possible smaller species with a size in the regime of 10 nm (e.g. unconsumed building units) that might coexist with the large aggregates. Whereas the presence of such species hardly affects the low q regime of the total scattering, it may influence significantly the scattering intensity in the q regime of the cylinder cross section and thus distort the values of the fitting parameter R . In order to scrutinize such an influence, we calculated theoretical scattering curves of a bimodal system consisting of large cylinders with lengths of $L_1 = 200$ nm and small cylinders with length $L_2 = 10$ nm and radius $R_2 = 0.5$ nm. Initially the large cylinders have a radius of $R_2 = 4$ nm and the ratio of total volume occupied by small cylinders to the total volume occupied by large ones is $V_2/V_1 = 4:1$ (Figure S4, lower left). Then the large cylinders grow laterally by incorporation of the small ones until the volume ratio has reduced to $V_2/V_1 = 1:4$ (Figure S4, upper right). In the course of the incorporation of small cylinders into large ones, the total volume of the latter has thus increased by a factor of 4, corresponding to an increase of the radius of the latter from $R_2 = 4$ to $R_2 = 8$ nm (Note that L_2 remains unaffected). Theoretical scattering curves I_{theor} of several intermediate states in the range of $4:1 \geq V_2/V_1 \geq 1:4$ were calculated using the cylinder form factor¹ P_{cyl} as given by eq SI-1:

$$I_{\text{theor}} = V_1 R_1^2 L_1 P_{\text{cyl}}(R_1, L_1) + V_2 R_2^2 L_2 P_{\text{cyl}}(R_2, L_2) \quad (\text{SI-4})$$

For all calculations, a polydispersity of cylinder cross-sections of $\sigma/R = 0.33$ has been included in terms of eq SI-2. Subsequently, the theoretical scattering curves have been fitted by means of eq SI-2, i.e. by excluding the small cylinders from the fitting function. During fitting, $L_2 = 200$ nm and $\sigma/R_2 = 0.33$ were kept constant and R_2 and I_0 were adjusted. For each fitted curve, a quantity proportional to the product of mass concentration and mass per unit length of the cylinders has been established (see eq SI-2) and plotted versus the corresponding fitted cylinder radius. The resulting correlation is compared with the exact correlation in Figure S4.

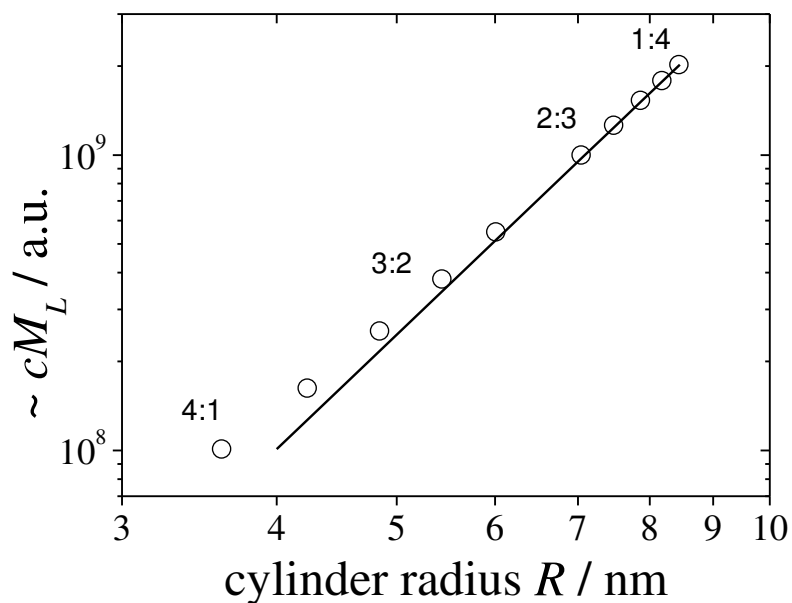


Figure S4. The theoretical correlation of the product of mass concentration c and mass per unit length M_L of a cylinder with its Radius R is represented by the continuous line ($cM_L \sim R^4$). The symbols (\circ) illustrate values of cM_L and R obtained by the fit procedure described above. The graph illustrates that the deviations of the fitted values from the correct ones represented by the continuous line are negligible.

Estimation of the Dyestuff Concentration within Centrifuged Dyestuff Gels

Figure S5 exemplifies a sample used for ASAXS and x-ray absorption measurements. In order to estimate the metal-to-dye stoichiometry of the formed aggregates situated in the gel phase at the bottom of the capillary, both the Sr^{2+} concentration within the gel, $[\text{Sr}^{2+}]_b$, and the concentration of Sr^{2+} ions that bind specifically to the dye within the gel, $[\text{Sr}^{2+}]_{\text{spec}}$, have to be determined. It is important to note that the latter may be significantly smaller than $[\text{Sr}^{2+}]_b$, since a large fraction of the gel phase might consist of aqueous Sr^{2+} solution, i.e. the gel might contain many Sr^{2+} ions that do not contribute to $[\text{Sr}^{2+}]_{\text{spec}}$. Whereas $[\text{Sr}^{2+}]_b$ is accessible by absorption measurements, $[\text{Sr}^{2+}]_{\text{spec}} \leq [\text{Sr}^{2+}]_b$ can only be determined by measuring ASAXS at the bottom position of the capillary (see ref. 2 and manuscript). Once $[\text{Sr}^{2+}]_{\text{spec}}$ is determined, only the dyestuff concentration at the bottom position, $c_{\text{dye-b}}$, is needed in order to establish the desired metal-to-dye stoichiometry of the formed aggregates. $c_{\text{dye-b}}$ can be estimated if the following two prerequisites are fulfilled: (i) the entire dyestuff has to be located at the bottom domain and (ii) the Sr^{2+} concentrations within the two domains of the capillary have to be

homogeneous in z -direction. Condition (i) is adequately fulfilled since the top domain is colorless. Besides, the obvious stability of the gel-like phase is in support of its homogeneity: After a short period of centrifugation, positions, shapes and colors of the bottom domains became invariant to further mechanical stress.

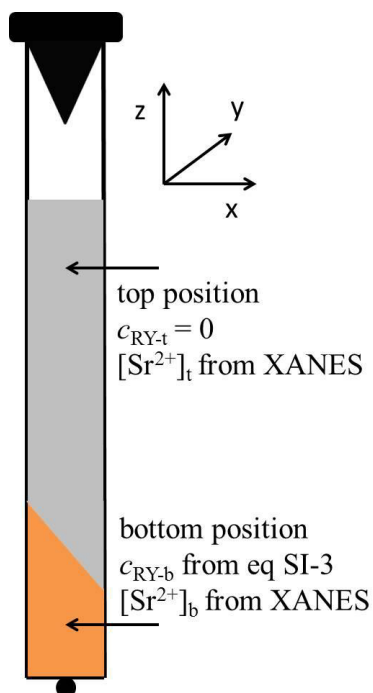


Figure S5. Schematic of a quartz capillary containing RD and YD in a 1:1 molar ratio as well as an excess of SrCl_2 . The excess of Sr^{2+} ions causes an immediate aggregation process by which the entire ensemble of RD and YD molecules is consumed. The formed aggregates can be separated from the remaining solution by centrifugation such that they form a gel-like domain located at the bottom of the capillary. The remaining solution thereby becomes colorless, indicating that the dyestuff concentration within the supernatant is close to zero. Provided that the Sr^{2+} concentrations within the gel, $[\text{Sr}^{2+}]_b$, and within the supernatant, $[\text{Sr}^{2+}]_t$, do not change with the z -coordinate, respectively, they can be determined by measuring x-ray absorption spectra at the top and the bottom position of the capillary.

We denote the total dyestuff and total Sr^{2+} concentrations within the sample as c_{dye} and $[\text{Sr}^{2+}]$, respectively, and use the denotations given in Figure S5 for the respective concentrations at top (t) and bottom (b) position. Successively we can write

$$c_{\text{dye}} = c_{\text{dye-b}} \frac{V - V_t}{V}, \quad \text{therefore} \quad c_{\text{dye-b}} = c_{\text{dye}} \frac{V}{V - V_t}, \quad (\text{SI-5})$$

where V is the total sample volume. The volume of the top domain, V_t , can be expressed considering

$$[\text{Sr}^{2+}]V = [\text{Sr}^{2+}]_t V_t + [\text{Sr}^{2+}]_b (V - V_t), \quad \text{therefore} \quad V_t = V \frac{[\text{Sr}^{2+}]_b - [\text{Sr}^{2+}]_t}{[\text{Sr}^{2+}]_t - [\text{Sr}^{2+}]_b}. \quad (\text{SI-1})$$

Introducing eq SI-1 into eq SI-5 cancels the total sample volume V and yields the following expression for the desired dyestuff concentration within the bottom domain.

$$c_{\text{dye-b}} = c_{\text{dye}} \frac{[\text{Sr}^{2+}]_b - [\text{Sr}^{2+}]_t}{[\text{Sr}^{2+}]_b - [\text{Sr}^{2+}]_t} \quad (\text{SI-2})$$

Calculation of Sr^{2+} Concentrations from X-Ray Absorption Spectra

The strontium-K-edge at ~ 16105 eV was used to quantify the Sr^{2+} concentrations $[\text{Sr}^{2+}]_t$ and $[\text{Sr}^{2+}]_b$ at the top and the bottom positions of the ASAXS samples, respectively. The mass density ρ of the absorbing species can be written as the derivative of the absorption coefficient μ with respect to the specific absorption cross-section σ .

$$\rho = \frac{d\mu}{d\sigma} \approx \frac{\Delta\mu}{\Delta\sigma} = \frac{\Delta(\mu \cdot d)}{d \cdot \Delta\sigma} \quad (\text{SI-4})$$

In eq SI-4, d is the sample thickness. An example of an x-ray absorption spectrum is given in Figure S6. X-ray absorption spectroscopy yields the product μd as a function of the photon energy E . The product $\mu d = \ln(I_0/I)$ is calculated from the intensities of the primary beam (I_0) and of the beam after transmitting the sample (I). As illustrated in Figure S6, the difference $\Delta(\mu d)$ can be determined by fitting a spline to the pre-edge data and to the post-edge data, respectively. We chose a function of the empirical form a/E^3 for the pre-edge spline, where a is a constant. The post-edge data was then fitted with the same spline plus $\Delta(\mu d)$, where $\Delta(\mu d)$ was chosen such that the areas A_1 and A_2 caused by the near-edge fine structure became equal. The edge difference in specific absorption cross-section, $\Delta\sigma$, was estimated by choosing a pre-edge data pair (σ_1, E_1) and a post-edge data pair (σ_2, E_2) from tabulated³ values.

$$\Delta\sigma \approx \frac{\sigma_2 E_2^3 - \sigma_1 E_1^3}{E_{\text{edge}}^3} \quad (\text{SI-5})$$

With $\Delta(\mu d)$ from the experimental data and $\Delta\sigma$ from eq SI-5, the mass density ρ corresponding to the mass concentration of Sr^{2+} is accessible via eq SI-4. The molar concentrations of Sr^{2+} is then calculated as $[\text{Sr}^{2+}] = \rho/M_{\text{Sr}}$, where M_{Sr} is the molar mass of strontium.

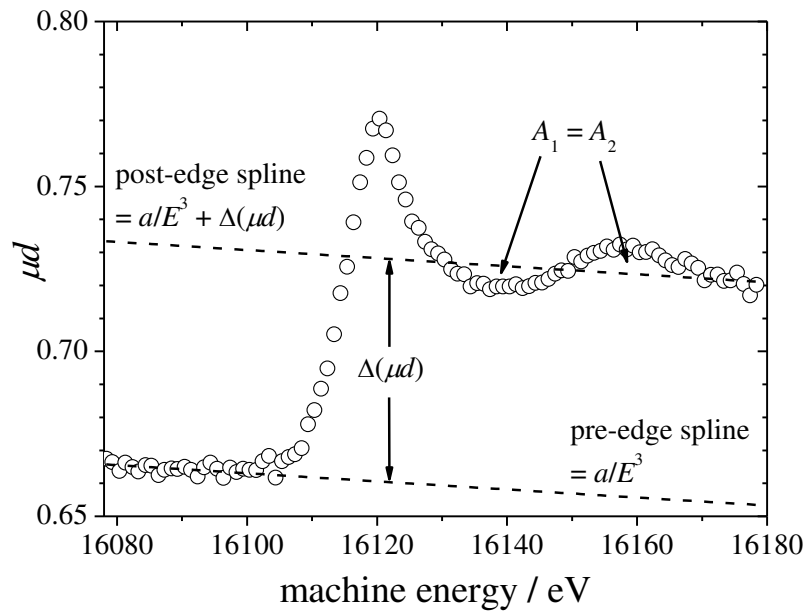


Figure S6. Illustration of an x-ray absorption spectrum used to determine the jump in absorption at the strontium-K-edge ($E_{\text{edge}} = 16105$ eV). The machine energy displayed by the abscissa deviates by about 8 eV from the real photon energy due to uncertainties of the monochromator control.

Direct Comparison of the SAXS from Samples Used for SAXS and ASAXS Experiments

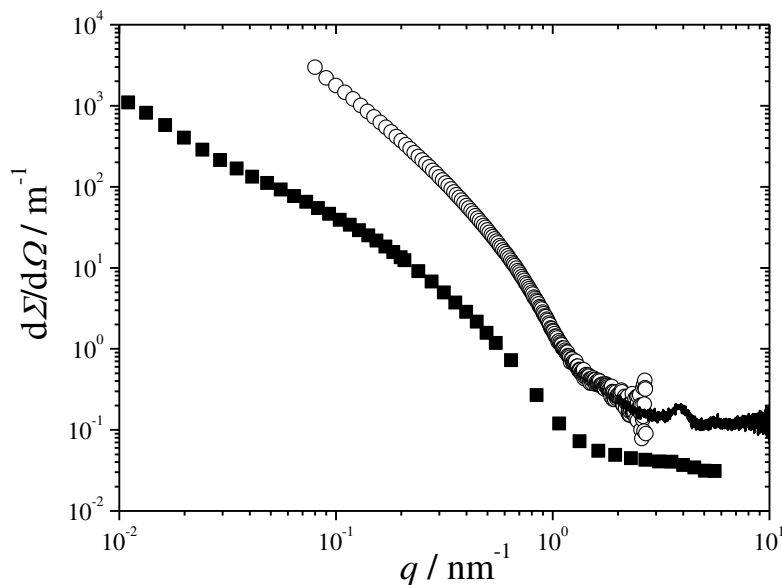


Figure S7. Comparison of the SAXS from a dyestuff gel (○ and continuous line at high q) containing approximately 11.3 g l^{-1} dyestuff (see Table 3 in the manuscript) with the scattering from a sample containing 0.33 g l^{-1} dyestuff (■). Both samples contain an excess of Sr^{2+} ions with respect to the anionic dyestuff charges and represent a temporally stable state of matured dyestuff aggregates.

References.

1. Guinier, A.; Fournet, G. *Small-Angle Scattering of X-Rays*. John Wiley and Sons: New York, 1955.
2. Stuhrmann, H. B. Resonance Scattering in Macromolecular Structure Research. *Adv. Polym. Sci.* **1985**, *67*, 123-163.
3. McMaster, W. H.; Kerr Del Grande, N.; Mallett, J. H.; Hubbell, J. H. *Compilation of X-Ray Cross Sections*. *Lawrence Livermore National Laboratory Report* **1969** UCRL-50174 Section II Revision I.